



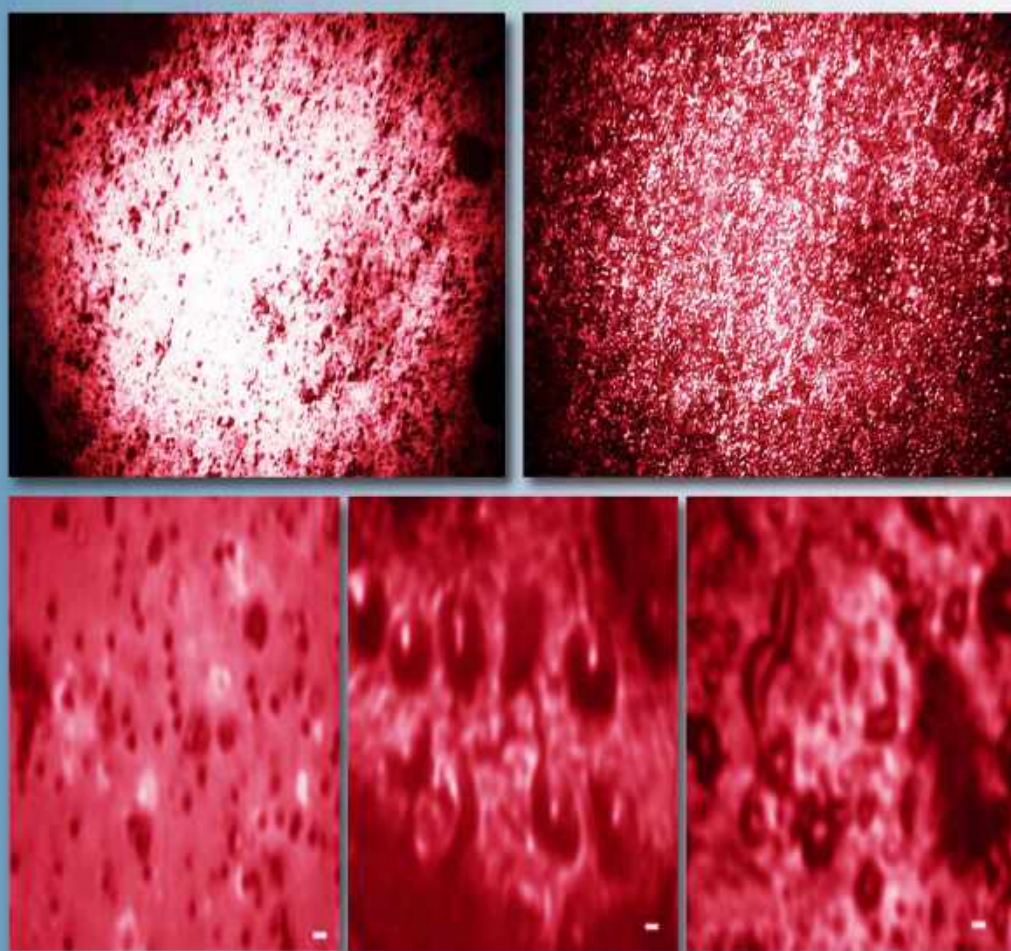
ISSN 1028-8546

Volume XXVI Number 2
Section: En July, 2020

Azerbaijan Journal of Physics

Fizika

www.physics.gov.az
jophphysics.wixsite.com/ajpphysics



Institute of Physics
Azerbaijan National Academy of Sciences
Department of Physical, Mathematical and Technical Sciences

Published from 1995
Ministry of Press and Information
of Azerbaijan Republic,
Registration number 514, 20.02.1995

ISSN 1028-8546
vol. XXVI, Number 02, 2020
Series: En

Azerbaijan Journal of Physics

FIZIKA

*Institute of Physics
Azerbaijan National Academy of Sciences
Department of Physical, Mathematical and Technical Sciences*

HONORARY EDITORS

Arif PASHAYEV

EDITORS-IN-CHIEF

Nazim MAMEDOV

Chingiz QAJAR

SENIOR EDITOR

Talat MEHDIYEV

INTERNATIONAL REVIEW BOARD

Ivan Scherbakov, Russia
Kerim Allahverdiyev, Azerbaijan
Mehmet Öndr Yetiş, Turkey
Gennadii Jablonskii, Belarus
Rafael Imamov, Russia
Vladimir Man'ko, Russia
Eldar Salayev, Azerbaijan
Dieter Hochheimer, USA
Victor L'vov, Israel

Vyacheslav Tuzlukov, South Korea
Majid Ebrahim-Zadeh, Spain
Anatoly Boreysho, Russia
Mikhail Khalin, Russia
Hasan Bidadi, Tebriz, Iran
Natiq Atakishiyev, Mexico
Tayar Djafarov, Azerbaijan
Arif Hashimov, Azerbaijan
Javad Abidinov, Azerbaijan

Salima Mehdiyeva, Azerbaijan
Talat Mehdiyev, Azerbaijan
Ayaz Bayramov, Azerbaijan
Tofiq Mammadov, Azerbaijan
Shakir Nagiyev, Azerbaijan
Rauf Guseynov, Azerbaijan
Almuk Abbasov, Azerbaijan
Yusif Asadov, Azerbaijan

TECHNICAL EDITORIAL BOARD

Senior secretary: Elmira Akhundova; Nazli Huseynova, Gulnura Jafarova
Nigar Akhundova, Elshana Aleskerova, Rena Nayimbayeva

PUBLISHING OFFICE

131, H. Javid ave., AZ-1143, Baku
ANAS, Institute of Physics

Tel.: (99412) 539-51-63, 539-32-23
Fax: (99412) 537-22-92
E-mail: jophphysics@gmail.com
Internet: www.physics.gov.az
<https://jophphysics.wixsite.com/ajpphysics>

Published at "Omega-5"
41, Aga Nematulla str., Baku

Sent for printing on: _____. 202_
Printing approved on: _____. 202_
Physical binding: _____
Number of copies: _____ 200
Order: _____

It is authorized for printing:

RASHBA SPIN-ORBIT INTERACTION IN SEMICONDUCTOR NANOSTRUCTURES (REVIEW)

B.G. IBRAGIMOV

*Institute of Physics, Azerbaijan National Academy of Sciences,
Azerbaijan State Oil and Industry University.*

Corresponding author: E-mail : Behbud.ibrahimov.93@mail.ru

In this work we review of the theoretical and experimental issue related to the Rashba spin-orbit interaction [1] in semiconductor nanostructures. The Rashba spin-orbit interaction has been a promising candidate for controlling the spin of electrons in the field of semiconductor spintronics. In this work I focus study of the electrons spin and holes in isolated semiconductor quantum dots and rings in the presence of magnetic fields. Spin-dependent thermodynamic properties with strong spin-orbit coupling inside their band structure in systems are investigated in this work. Additionally, specific heat and magnetization in two- dimensional, one-dimensional ring and quantum dot nanostructures with spin- orbit interaction are discussed.

Keywords: spin-orbit interaction, Rashba effect, two-dimensional electron gas, one-dimensional ring, quantum wire, quantum dot, semiconductor nanostructures.

PACS: 35Q41

INTRODUCTION

The use of electron spin in electronic devices has been of great interest to scientists during the last three decades. The spin-orbit interaction is also called spin-orbit coupling or spin-orbit effect. It means that any interaction of a particle's spin with its motion. Spin degree of freedom is made by spin-orbit coupling which is respond to its orbital environment. Moving of the electron in an external electrical field leads to creating spin-orbit interaction and experiences an effective magnetic field in its own reference frame, that in turn couples to its spin through the Zeeman effect [2]. The magnitude of the spin-orbit interaction increases with the atomic number which is a relativistic effect. The spin-orbit interaction is found with asymmetry in the underlying structure in crystals in semiconductor systems [3]. In bulk it seems in crystals without an inversion center (e.g. zinc blende structures) and is called the Dresselhaus spin-orbit interaction [4]. However, Rashba term is aroused from the structural asymmetry of the confining potential in heterostructures [5]. A set of practical information on the cyclotron resonance and also the combined resonance of two-dimensional electron gas at the GaAs-AlxGa1-xAs heterojunctions' interface [6,7], shown that the spin degeneracy was lifted in the inversion layer. For describing this experimental information in term of spin-orbit interaction is developed by the theory [1,5]. In semiconductor nanostructures, studies of transport phenomena and spin-dependent confinement have been progressing importantly since spintronics became a focus of recent interest. The first offer of Das and Datta assign that the basic elements of spintronic devices [8]. Several possible structures with the basic elements were analyzed. Different kinds of electron spin detection methods have been investigated. Lately the coherent spin transport has been showed in heterostructures and homogeneous semiconductors [9]. The most necessary property of III-V semiconductors to be used in all

semiconductor spintronic devices is the spin-orbit interaction [4,5]. In III-V and II-VI semiconductors the spin-orbit interaction has been used successfully to interpret experimental results in different quantum wire and well structures. Additionally, it lifts the conduction state spin-degeneracy [5,11]. Exploiting the spin-orbit interaction in the conventional III-V nonmagnetic semiconductors to design basic and high-speed spintronic devices is reviewed in paper [12]. To achieve this [12], concentrate on spin-dependent electronic characteristics of semiconductor nanostructures.

RASHBA EFFECT IN TWO-DIMENSIONAL ELECTRON SYSTEM

Spin-orbit interaction has a vital role in spin relaxation, optical phenomena and transport, which are actively studied for entirely new applications in semiconductor spintronics. Study of the effects of spin-orbit interaction in two-dimensional electronic systems exposed to a perpendicular magnetic field and were initially associated with Landau volume levels: the spin-orbit interaction renormalization of energy dispersions, the interplay among various spin-orbit interaction mechanisms, effects of magnetic transport and electron-electron interaction. In general, the Hamiltonian described the spin-orbit interaction $H_{so} = (\alpha/\hbar)\nabla U \cdot (\sigma \times p)$, in here p is the momentum operator, α is the spin-orbit coupling parameter and having a dimension of length squared, which is proportional to the interface electric field and is sample dependent, σ is the Pauli matrices vector. The value of α determines the contribution of the Rashba spin-orbit coupling to the total electron Hamiltonian. When an external electric field is present, the relativistic correction introduces a relation between the electron spin and its own momentum. The coupling of the electron spin and its orbital motion lifted the spin degeneracy of the two dimensional

electron gas energy bands at $k \neq 0$ in the absence of a magnetic field. This coupling arises due to inversion asymmetry of the potential which confines the two dimensional electron gas system. This is described by Hamiltonian which is given many books and papers by:

$$H_{so} = \frac{\alpha}{\hbar} (\vec{\alpha} \times \vec{p})_z = i\alpha \left(\sigma_y \frac{\partial}{\partial x} - \sigma_x \frac{\partial}{\partial y} \right) \quad (1)$$

Where the z axis is selected perpendicular to the two dimensional electron gas system lying in the x-y plane.

In the presence of the Rashba spin-orbit term the Hamiltonian of the two-dimensional electron gas systems in the plane (x,y) is given :

$$H = \frac{\vec{p}^2}{2m} + \frac{\alpha}{\hbar} (\vec{\sigma} \times \vec{p})_z \quad (2)$$

The eigenvalues of this Hamiltonian is

$$E \pm (\vec{k}) = \frac{\hbar^2 k^2}{2m} \pm \alpha k = \frac{\hbar^2}{2m} (k_x \pm k_{so})^2 - \delta_{so} \quad (3)$$

Here $k = \sqrt{k_x^2 + k_y^2}$ is the electron momentum modulus, $k_{so} = \frac{\alpha m}{\hbar^2}$ is a recast form of the spin orbit

coupling constant and $\delta_{so} = \left(\frac{\alpha m}{\hbar} \right)^2$ which is neglected due to spin orbit coupling α is small. The eigenvectors of the Hamiltonian (1) relative to the spectrum (2) are plane wave's function of the momentum \vec{k}

$$\psi_+(x, y) = e^{i(k_x + k_y)} \frac{1}{\sqrt{2}} \begin{pmatrix} 0 \\ 1 \end{pmatrix} e^{-i\theta} \quad (4)$$

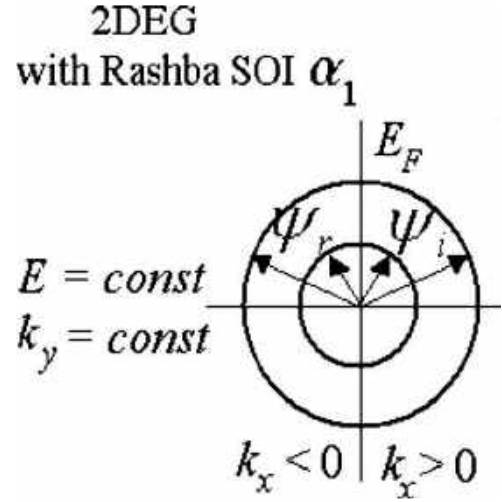
$$\psi_-(x, y) = e^{i(k_x - k_y)} \frac{1}{\sqrt{2}} \begin{pmatrix} 1 \\ -i \end{pmatrix} e^{-i\theta} \quad (5)$$

Scattering geometry of two-dimensional electron gas with Rashba spin-orbit interaction on the spin-orbit lateral superlattice shown in Fig. 1 [13]

Fig.1. Two-dimensional electron gas scattering geometry with Rashba spin-orbit interaction on the spin-orbit lateral superlattice. The reflected ψ_r and incoming ψ_i spinors are the eigenstates of Rashba Hamiltonian with spin-orbit coupling constant α_1 and wave vectors belonging to the same Fermi contour [13].

In many two-dimensional electronic systems the main mechanism of spin relaxation is the Dyakonov – Perel spin relaxation mechanism [14, 15]. In this mechanism electron spins sense an effective

momentum dependent magnetic field randomized by electron-scattering events, which leads to relaxation of electron spin polarization. In the last decade, a number of theoretical and experimental studies of the features of Dyakonov – Perel spin relaxation were published [16–19]. This has been shown in Ref. [20] that the spin relaxation time for two-dimensional electrons depends not only on the material parameters, for example, the spin-orbit interaction strength, electron mean free path, etc., but also on the initial spin polarization profile. The spin-orbit coupling defines the electrons spin-relaxation time in semiconductor heterostructures and in ordinary semiconductors [21]. So it has a significant role in the physics of diluted magnetic semiconductors [22].



ONE-DIMENSIONAL RING WITH SPIN-ORBIT INTERACTION

Nanostructures with ring geometry are of great interest, because they provide unique opportunities for studying quantum interference effects, for example, the persistent current and the Aharonov–Bohm effect.

The theoretically studying of the persistent current of electrons without free spin in the one dimensional ring was shown in Ref [23]. Founding shapes and periods of the current oscillations created great interest. The current oscillations' shapes and periods were found. Periodic dependence on a magnetic flux of the persistent current is one of the important properties of it. That effect occurs for the isolated ring [24] and also the ring connected to an electron reservoir [23, 25]. The theoretically studying of the magnetic moment of a 2D electron gas with the Rashba spin–orbit interaction in a magnetic field was investigated in Ref [26]. The persistent current, the electronic thermal capacity in the dimensional ring have been investigated in [30, 31], [32] respectively. Oscillations of the magneto transport [27–29], and the magnetic properties [33] in the dimensional ring have been studied. An obvious analytic expression is got by taking into account the spin-orbit interaction in the Rashba model [34] for the persistent current and magnetic moment of the electron gas in one dimensional ring.

Over the ten years, great attention has been dedicated toward control and engineering of freedom spin degree at mesoscopic scale, usually referred to as spintronics [35].

Diluted magnetic semiconductors is a prime class of materials for spintronics. These are solutions of the A2B6 or A3B5 with a high density of magnetic impurities (usually, Mn). For combining semiconductor electronics with magnetism DMS is one of the best candidates. The strong s-d exchange interaction between the local magnetic ions and the carriers leads to Diluted magnetic semiconductors offers us with an interesting possibility for tailoring the spin splitting and the spin polarization [36].

The spin-orbit interaction effects on the one-dimensional quantum ring properties has attracted much attention [37]. In Ref [38] have studied the Rashba SO interaction, the effect of the magnetic field the finite temperature and also the s-d exchange interaction on the conductance of a DMS hollow cylindrical wire.

The specific heat and magnetization of a diluted magnetic semiconductor (DMS) quantum ring in the presence of magnetic field have been calculated by us in the paper [39] and also we take into consideration the effect of Rashba spin-orbital interaction, the exchange interaction and the Zeeman term on the specific heat. Additionally, in diluted magnetic semiconductor quantum ring, we calculated the electrons energy spectrum. Furthermore, at finite temperature of a DMS (Diluted magnetic semiconductor) quantum ring, the specific heat dependency on the magnetic field and Mn concentration have been calculated by us. In Fig. 2 show us the average magnetization of diluted magnetic semiconductors quantum ring as a magnetic function and Rashba spin-orbit coupling constant $\alpha = 160$ meV. nm at fixed Mn concentration $x = 0.05$ and $T = 10$ K.

The magnetization changes abruptly with a small increase in H and the peak is observed after which the magnetization starts to decrease.

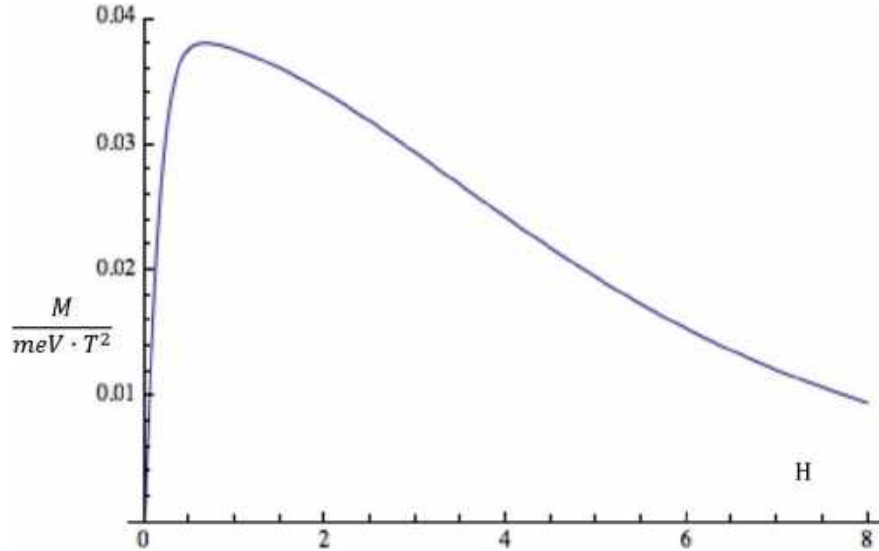


Fig. 2. The average magnetization of diluted magnetic semiconductors quantum ring as a function of magnetic with Rashba spin-orbit coupling constant $\alpha = 160$ meV.nm at fixed Mn concentration $x=0.05$ and $T=10$ K [39].

The magnetization of electrons in a diluted magnetic semiconductor quantum ring have been investigated in the paper [40] by us. The Rashba spin-orbit interaction, the exchange interaction and the Zeeman term effect are taken into account by us and also we have calculated wave function and energy spectrum of the electrons in DMS quantum ring. Likewise, as a function of the magnetic field at finite temperature of a diluted magnetic semiconductor quantum ring for strong degenerate electron gas, the magnetic moment has been calculated.

We have theoretically studied the magnetic properties and electronic spectra of a Diluted magnetic semiconductors quantum ring in externally applied static magnetic field in the paper [41, 42]. It has been shown that if Mn concentration rise, the compensation points reduce Also, it was obtained that with increasing manganese content in the DMS quantum ring a transition to the paramagnetic from the

antiferromagnetic properties one occurs for finding DMS ring electrons magnetization it is necessary to obtain in the ring, the expression of the electron gas's free energy. That equation can be determined from the classical partition function Z . We express the given non-degenerate energy spectrum by a sum over all possible states of the system

$$Z = \sum_{l,\sigma} e^{-\beta E_{l,\sigma}} \quad (6)$$

In here, $\beta = \frac{1}{k_B T}$ and k_B -is the Boltzmann constant and T is the thermodynamic equilibrium temperature.

$$F = -k_B T \ln Z \quad (7)$$

We use the expression of the free energy of the ring for calculation the magnetization of the electron gas:

$$M = -\frac{\partial F}{\partial H} \quad (8)$$

As it is seen from Fig. 1, with changing of the AB flux at fixed temperature the magnetization for free electron model system ($x=0$) varies from negative to positive values, such a behavior is typical for antiferromagnetic systems.

The exchange interaction between the localized angular moments changes with increasing in the $\text{Cd}_{1-x}\text{Mn}_x\text{Te}$ solid solutions Mn concentration and this leads to change in the magnetization of the DMS quantum ring. The calculations showed that, a transition from the antiferromagnetic properties to the

paramagnetic one is observed in a DMS quantum ring as the manganese content increases.

With changing the AB flux at fixed temperature, the magnetization $x=0.0004$ varies to negative values from positive for Mn concentration in the non-interacting DMS quantum rings, which is typical for paramagnetic systems. When $=l$ and where l is integer or half integer, as it can be seen the magnitude of magnetization is equal to zero.

These points are called “Aharonov-Bohm compensation points” at that time the magnetization disappears at fixed temperature and magnetic flux varies.

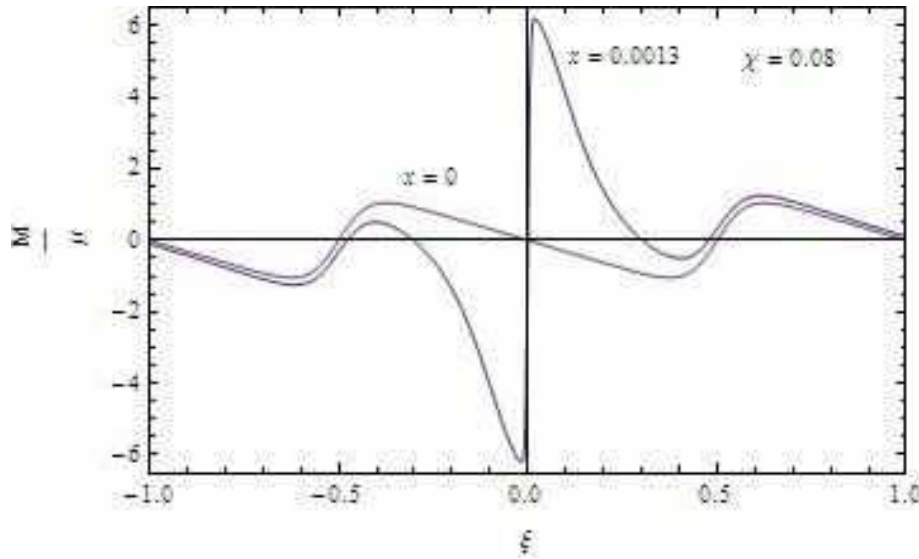


Fig.3. Dependence of the magnetization in terms of μ_B on the magnetic flux for the cases where Mn concentrations $x=0$, $g=0$, and $x=0.0013$, $g=-1.67$ for $x = 0.08$.

QUANTUM DOTS IN THE PRESENCE OF THE SPIN-ORBIT INTERACTION.

The spin of an electron confined in a semiconductor quantum dot is a promising candidate for a scalable quantum bit [43, 44]. The electron spin states in quantum dots are expected to be very stable, because the zero dimensionality of the electron states in quantum dots leads to a significant suppression of the most effective 2D spin-flip mechanisms [45].

During the past few decades, spin physics has attracted substantial attention in semiconductors. Experimental and theoretical studies have made it possible to fabricate Nano-structured semiconductor devices [46, 47] with quantum confinement in all spatial directions. The size of these structures are typically consist of several nanometers and are usually known as objects of zero size or, more technically called as quantum dots [48]. With the advent of modern manufacturing technologies, such as molecular beam epitaxy, selective ion implantation, nanolithography and etching and it has become possible to design such semiconductor quantum heterostructures in which the electrical properties of a quantum dot are very sensitive to the spin of electrons. In this context where devices are controlled by spin-

polarization is “Spintronics” [49, 50]. This leads to offer of many devices like spin filter, spin transistors etc. Investigation of spin-dependent phenomena in low dimensional systems has attracted a rage over the years. Spin-dependent phenomena offer opportunities to advance many optoelectronic devices in which these devices can be controlled by intrinsic spin-orbit interaction. The presence of a heterojunction leads to inversion asymmetry of the confinement potential in semiconductor nanostructures, such as GaAs, InAs and $\text{In}_{1-x}\text{Ga}_x\text{As}$ quantum dots, quantum wells and quantum wires.

Electron-phonon interaction plays an important role in defining the transport and other properties of quantum dots. Electron-phonon interaction leads to various physical phenomena, such as superconductivity, polaronic effect, magneto phonon anomalies etc. Thus it is our main target to learn the polaronic effects in the energy states of an electron and other quantum structures. It was theoretically studied in Ref [51] that the RSOI effect on an electron polaronic energy spectrum in a 2D parabolic quantum dot of a polar semiconductor. There is extended investigate to the bound polaron difficulty where the electron is bound to a Coulomb impurity. Thanks to modern advanced technologies, it has become possible

to study the energy levels of electrons of various types of quantum dots. In [38–42, 52–54] has extensively studied the orbital and spin magnetization of those systems over the last years. The point of interest is that the magnetization provides information on the multi particle dynamics of the dots in an external magnetic field. Additionally, an extensive study of magnetic properties of nanosystems [56–59] is required by recent development of spintronics. The spin states in the quantum dots are promising candidates for realizations of qubit in the quantum computing [60]. The design of the magnetic properties of semiconductor quantum dots and energy shells is controlled by the electron spin [48–50]. For III–V semiconductor nanostructures the interaction among orbital angular and spin momenta [5] has an important role in the energy spectrum formation (spin–orbit interaction). When the potential through which the carriers travel is inversion asymmetric, the spin–orbit

interaction eliminates the spin degeneracy of the energy levels even without external magnetic fields. The effect of the spin–orbit interaction on the electron magnetization of small semiconductor quantum dots is theoretically studied in Ref [61]. Moreover, In Ref. [61] a study of the effect of the spin–orbit interaction on the magnetic susceptibility of small semiconductor quantum dots. These characteristics show quite interesting behavior at low temperature. There are many investigations on the thermodynamic properties of quantum dots, because of their huge potential for future technological applications [51–54]. In the presence of the spin Zeeman effect the specific heat and entropy of GaAs quantum dot and Gaussian confinement have been studied Boyacioglu and Chatterjee [62]. At low temperature they observed a Schottky-like anomaly in heat capacity while that anomaly approaches a saturation of 2kB with rising temperature.

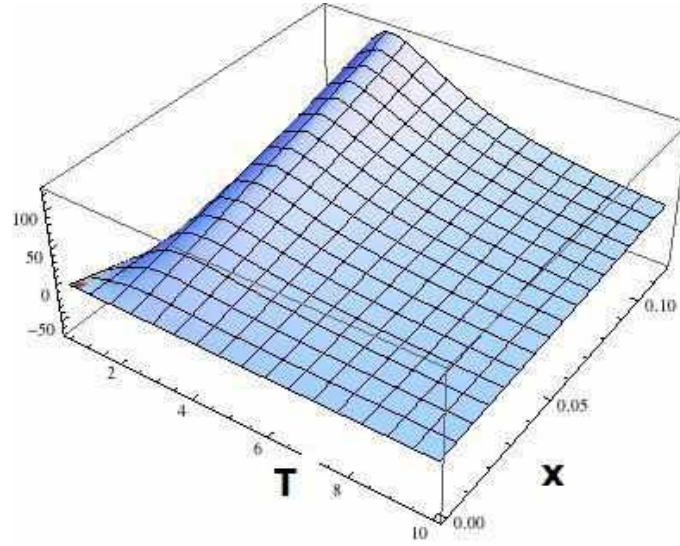


Fig. 4. The dependence of $\frac{C_v}{k_B}$ as function of temperature and Mn concentration at fixed $H = 5Tl$. [68].

Boyacioglu et al [63] investigated that diamagnetic and paramagnetic effects in a Gaussian quantum dot can create the total magnetization and susceptibility. The magnetic properties of a quantum ring and dot using a three-dimensional model are calculated by Climente et al. [64].

In the presence of external electric and magnetic field the thermal and magnetic properties of a cylindrical quantum dot with asymmetric confinement has been studied in the paper [65]. In [66] have been investigated the thermodynamic properties of an InSb quantum dot in the presence of Rashba spin-orbit interaction and a static magnetic field. Fundamental part of materials for spintronics forms diluted magnetic semiconductors (DMS). They are A^2B^6 or A^3B^5 solutions with high density of magnetic impurities (usually, Mn). The Zeeman effects and exchange terms are taken into account on the heat capacity of diluted magnetic semiconductors quantum

dots and the electron is assumed to be moving in an asymmetrical potential in the paper [68].

In Fig.3 we demonstrate as function of temperature and Mn concentration at fixed $H = 5Tl$ the specific heat of the DMS quantum dot in the presence of exchange interaction and Zeeman term. According to this figure as the temperature is risen the specific heat unexpectedly increases and then reduces giving a peak-like structure.

I thank prof. A.M. BABANLI and prof. G. B. IBRAGIMOV for useful discussions.

Declaration of Competing Interest

The author declares that he does not known competing financial interests or personal relationships that could have appeared to influence the work reported in this paper.

- [1] *E. Rashba*. Fiz. Tverd. Tela (Leningrad) 2, 1224 (1960), [Sov.Phys.Solid State 2, 1109 (1960)].
- [2] *W. Greiner*. Relativistic quantum mechanics (Springer, 1987).
- [3] *R. Winkler*. Spin-orbit Coupling Effects in Two-Dimensional Electron and Hole Systems (Springer Berlin).
- [4] *G. Dresselhaus*. Spin-Orbit Coupling Effects in Zinc Blende Structures Phys. Rev. 100, 580 1955.
- [5] *Y.A. Bychkov and E. I. Rashba*. Journal of Physics C:Solid State Physics 17, 6039, 1984.
- [6] *D. Stein, K.V. Klitzing, and G. Weimann*. Electron Spin Resonance on GaAs–Al_xGa_{1–x}As Heterostructures Phys. Rev. Lett. 51, 130, 1983.
- [7] *H.L. Stormer, Z. Schlesinger, A. Chang, D.C. Tsui, A.C. Gossard, and W. Wiegmann*. Energy Structure and Quantized Hall Effect of Two-Dimensional Holes Phys. Rev. Lett. 51, 126, 1983.
- [8] *S. Datta and B. Das*. Electronic analog of the electro-optic modulator Appl. Phys. Lett. 56, 665, 1990.
- [9] *J.M. Kikkawa, I.P. Smorchkova, N. Samarth, and D.D. Awschalom*. Room-Temperature Spin Memory in Two-Dimensional Electron Gases Science 277, 1284–1287, 1997.
- [10] *E.A. de Andrada e Silva, G.C. La Rocca, and F. Bassani*. Spin-orbit splitting of electronic states in semiconductor asymmetric quantum wells Phys. Rev. B 55, 16293, 1997.
- [11] *O. Voskoboynikov and C.P. Lee*. Spin–Orbit Interaction and All-Semiconductor Spintronics Journal of Superconductivity volume 16, pages 361–363, 2003.
- [12] *D.V. Khomitsky*. Scattering on the lateral one-dimensional superlattice with spin-orbit coupling Phys. Rev. B 76, 033404, 2007.
- [13] *M.I. Dyakonov and V.I. Perel*. [Spin relaxation of conduction electrons in noncentrosymmetric semiconductors](#), Soviet Physics Solid State, 13 (12), 3023–3026, 1972.
- [14] *M.I. Dyakonov and V.Y. Kachorovskii*. “Spin Relaxation of Two Dimensional Electrons in Noncentrosymmetric Semiconductors,” Soviet Physics: Semiconductors, Sov. Phys. Semicond. 20, 110 _1986.
- [15] *J.D. Koralek, C.P. Weber, J. Orenstein, B.A. Bernevig, S.-C. Zhang, S. Mack, and D.D. Awschalom*. Emergence of the persistent spin helix in semiconductor quantum wells. Nature _London_ 458, 610, 2009.
- [16] *P. Kleinert and V. V. Bryksin*. Electric-field-induced long-lived spin excitations in two-dimensional spin-orbit coupled systems, Phys. Rev. B 79, 045317, 2009.
- [17] *M. Duckheim, D.L. Maslov, and D. Loss*. Dynamic spin-Hall effect and driven spin helix for linear spin-orbit interactions, Phys. Rev. B 80, 235327, 2009.
- [18] *I.V. Tokatly and E.Ya. Sherman*. Ann. Phys. 325, 1104, 2010.
- [19] *Y.V. Pershin*. Phys. Rev. B 71, 155317 2005. [Long-Lived Spin Coherence States in Semiconductor Heterostructures](#)
- [20] *J.M. Kikkawa & D.D. Awschalom*. Lateral drag of spin coherence in gallium arsenide. Nature, 1999, 397, 139.
- [21] *S. Sanvito, G. Theurich & Hill NA*. (2002), Density functional calculations for III–V diluted ferromagnetic semi-conductors: a review. J Supercond, 15, 85.
- [22] *M. Peshkin and A. Tonomura*. The Aharonov–Bohm Effect, in Lecture Notes in Physics, Vol. 340 (Springer-Verlag, Berlin, 1989).
- [23] *H. Fai Cheung, Y. Gefen, E.K. Riedel, W.-H. Shih*. Persistent currents in small one-dimensional metal rings, Phys. Rev. B 37, 1988 6050.
- [24] *D. Loss, P. Goldbart*. Period and amplitude halving in mesoscopic rings with spin, Phys. Rev. B 43 (1991) 13762.
- [25] *M.V. Moskalets*. Oscillations of the thermodynamic properties of a one-dimensional mesoscopic ring caused by Zeeman splitting, JETP Lett. 70, 1999, 602.
- [26] *V.A. Margulis, V.A. Mironov*. Magnetic moment of a 2D electron gas with spin-orbit interaction, JETP 108 ,2009, 656.
- [27] *A.G. Aronov, Y.B. Lyanda-Geller*. Spin-orbit Berry phase in conducting rings, Phys. Rev. Lett. 70, 1993, 343.
- [28] *X.F. Wang, P. Vasilopoulos*. Spin-dependent magnetotransport through a mesoscopic ring in the presence of spin-orbit interaction, Phys. Rev. B 72, 2005, 165336.
- [29] *B. Molnar, F.M. Peeters, P. Vasilopoulos*. Spin-dependent magnetotransport through a ring due to spin-orbit interaction, Phys. Rev. B 69 (2004) 155335.
- [30] *J. Splettstoesser, M. Governale, U. Zulicke*. Persistent current in ballistic mesoscopic rings with Rashba spin-orbit coupling, Phys. Rev. B 68, 2003, 165341.
- [31] *J.S. Sheng, K. Chang*. Spin states and persistent currents in mesoscopic rings: Spin-orbit interactions, Phys. Rev. B 74, 2006, 235315.
- [32] *X.-E. Yang, Y.-C. Zhou*. Magnetism and structural distortions in the La_{0.7}Sr_{0.3}MnO₃ metallic ferromagnet, Phys. Rev. B 53, 1996, 10167.
- [33] *H.-Y. Chen, P. Pietilainen, T. Chakraborty*. Electronic optic and magnetic properties of quantum ring in Novel systems, Phys. Rev. B 78, 2008, 073407.
- [34] *V.A. Margulis, V.A. Mironov*. Magnetic moment of an one-dimensional ring with spin–orbit interaction Physica E 43, 2011, 905–908.
- [35] *S.A. Wolf, et al.*, Spintronics: a spin-based electronics vision for the future, Science 294, 2001, 1488.
- [36] *P.A. Wolff*. Semiconductors and semimetals, in: J.K. Furdyna, J. Kossut (Eds.), Diluted Magnetic Semiconductors, Academic, New York, 1988.

- [37] A.V. Chaplik, L.I. Magarill. Effect of the spin-orbit interaction on persistent currents in quantum rings, *Superlattice. Microst.* 18,1995, 4.
- [38] B.H. Mehdiyev, A.M. Babayev, S. Cakmak, E. Artunc. Rashba spin-orbit coupling effect on a diluted magnetic semiconductor cylinder surface and ballistic transport, *Superlattice, Microst* 46 2009, 4.
- [39] A.M. Babanlı, B.G. Ibragimov. Specific heat in diluted magnetic semiconductor quantum ring Superlattices and Microstructures 111, 2017, 574-578.
- [40] A.M. Babanlı, B.G. Ibragimov. *AJP Fizika* 2019, vol. XXV, Number 01, page.35-38.
- [41] A.M. Babanlı, B.G. Ibragimov. Magnetic moment of the lattice of non-interacting diluted magnetic semiconductor ring. *Modern Trends in Physics International Conference* 01-03 may 2019 Baku.
- [42] A.M. Babanlı, B.G. Ibragimov. "Aharonov-bohm paramagnetism" and compensation points in noninteracting diluted magnetic semiconductor quantum ring. *Journal of Magnetism and Magnetic Materials* 495,2020, 165882.
- [43] D. Loss and D. P. DiVincenzo. Quantum computation with quantum dots, *Phys. Rev. A* 57, 120,1998.
- [44] L.M. K. Vandersypen *et al*, in *Quantum Computing and Quantum Bits in Mesoscopic Systems* (Kluwer Academic, New York, 2003); quant-ph/0207059.
- [45] A.V. Khaetskii and Y.V. Nazarov. Spin relaxation in semiconductor quantum dots, *Phys. Rev. B* 61, 12 639, 2000.
- [46] Can-Ming Hu, Junsaka Nitta, Tatsushi Akazaki, Jiro Osaka, P. Pfeffer, and W. Zawadzki. Polaronic and bound polaronic effects in the energy states of an electron in a two-dimensional parabolic quantum dot in the presence of Rashba spin-orbit interaction, *Phys. Rev. B* 60, 7736, 1999.
- [47] E.A. de Andrada e Silva, G.C. La Rocca, and F. Bassani. Spin-orbit splitting of electronic states in semiconductor asymmetric quantum wells, *Phys. Rev. B* 55, 16 293, 1997.
- [48] N.F. Johnson. *J. Phys.: Condens. Matter* 7 965. Quantum dots: few-body, low-dimensional systems 1995.
- [49] S. Datta and B. Das. *Appl. Phys. Lett.* 56, 665 1990. Electronic analog of the electro-optic modulator, <https://doi.org/10.1063/1.102730>
- [50] B.E. Kane. A silicon-based nuclear spin quantum computer, *Nature London* 393, 133, 1998.
- [51] Kuntal Bhattacharyya and Ashok Chatterjee *Polaronic and Bound Polaronic. Effects in The Energy States of An Electron in A Two-Dimensional Parabolic Quantum Dot in The Presence of Rashba Spin-Orbit interaction AIP Conference Proceedings* 2142, 090008, 2019; <https://doi.org/10.1063/1.5122452>.
- [52] D. Bimberg. Quantum dots: Paradigm changes in semiconductor physics, *Semiconductors* 33, 951 1999.
- [53] O. Steffens, M. Suhrke, and U. Rössler. *Physica B* 256–258, 147, 1998.
- [54] S. Tarucha *et al.*, Spin effects in semiconductor quantum dot structures, *Physica E (Amsterdam)* 3, 112, 1998.
- [55] H. Tamura. Magneto-photoluminescence in high magnetic fields from InGaAs/GaAs quantum dots formed in tetrahedral-shaped recesses, *Physica B* 249–251, 210, 1998.
- [56] G.A. Prinz. Magnetoelectronics, *Science* 282, 1660, 1998.
- [57] B.E. Kane. A silicon-based nuclear spin quantum computer, *Nature (London)* 393, 133, 1998.
- [58] D.D. Awschalomand, J.M. Kikkawa. *Phys. Today* 52, 33, 1999. Electron Spin and Optical Coherence in Semiconductors.
- [59] S. Das Sarma, J. Fabian, X. Hu, and I. Žutić. *Solid State Commun.* 119, 207, 2001. Spin-Polarized Bipolar Transport and its applications
- [60] D. Lossand D.P. DiVincenzo. *Phys. Rev. A* 57, 120 (1998). Quantum computation with quantum dots.
- [61] O. Voskoboinikova. Magnetic properties of parabolic quantum dots in the presence of the spin–orbit interaction.
- [62] B. Boyacioglu and A. Chatterjee. *J. Appl. Phys.* 112, 083514 (2012). Heat capacity and entropy of a GaAs quantum dot with Gaussian confinement doi:10.1063/ 1.4759350.
- [63] B. Boyacioglu and A. Chatterjee. *Phys. E*, 44, 1826, 2012 . Dia- and paramagnetism and total susceptibility of GaAs quantum dots with Gaussian confinement doi:10.1016/j.physe. 2012.05.001.
- [64] J.I. Climente, J. Planelles, and J.L. Movilla. *Phys. Rev. B*, 70, 081301, 2004. Magnetization of nanoscopic quantum rings and dots, doi:10.1103/PhysRevB.70.081301.
- [65] Sukirti Gumber, Manoj Kumar, Monica Gamblur, Man Mohan, Pradip Kumar Jha, *Can. J. Phys.* 93, 2015, 1e5.
- [66] Sukirti Gumber, Manoj Kumar, Pradip Kumar Jha, Man Mohan. *Chin. Phys. B* vol. 25 (5) 2016, 056502.
- [67] S. Gumber. *Metal., Canadian Jour. of Phys.*, Vol93 No.11,2015, 1264-1268.
- [68] A.M. Babanlı, B.G. Ibragimov. Heat capacity of electrons in diluted magnetic semiconductor quantum dot. The 6 th International conference on Control and Optimization with Industrial Applications July 11-13 2018. Baku, vol 2, page 89-91.

Received: 12.05.2020

DIELECTRIC, CONDUCTIVITY, AND ELECTRO-OPTIC PROPERTIES OF LIQUID CRYSTAL 5CB DOPED BY SINGLE-WALLED CARBON NANOTUBES

T.D. IBRAGIMOV, A.R. IMAMALIYEV, G.F. GANIZADE

Institute of Physics of NAS Azerbaijan

131, H. Javid ave., Baku, Azerbaijan, AZ-1143

e-mail: tdibragimov@mail.ru

The effect of single-walled carbon nanotubes (SWCNTs) on the dielectric, conductive, and electro-optic properties of nematic liquid crystal 4-cyano-4'-pentylbiphenyl (5CB) has been studied. It was shown that the additive of SWCNTs with concentration of 0.5% leads to strong interaction between SWCNTs and molecules, which increases the order parameter of 5CB. As a result, the clearing point is raised, the longitudinal component of the dielectric permittivity increases while the transverse component decreases. The incipient percolation effect promotes to the dominance of hopping electron conductivity over ionic conductivity, leading to an increase in specific conductivity. In this case, the elastic splay constant of 5CB is enhanced and, accordingly, the threshold voltage of the S-effect increases. A decrease in the Van-der-Waals interaction between molecules decreases viscosity. As a result, the flip-flop motion of molecules become easier and the switching times are also reduced.

Keywords: liquid crystal, single-walled carbon nanotubes, dielectric relaxation, electric conductivity, threshold voltage.

PACS: 64.70.mj;64.70.pv;77.84.Nh;82.70.Dd.

1. INTRODUCTION

Single-walled carbon nanotubes (SWCNTs) are rod-shaped and have a diameter comparable to the transverse size of elongated liquid crystal (LC) molecules. In addition, there is strong interaction of nanotubes with LC molecules, as a result of which they are aligned along the preferred direction (director) of LC molecules [1]. In that respect, liquid crystal with such nanoparticles can significantly change its physical properties.

The aim of this work is to study the effect of SWCNTs on the dielectric, conductivity, and electro-optic properties of nematic liquid crystal 4-cyano-4'-pentylbiphenyl (5CB).

2. EXPERIMENTAL

We used nematic liquid crystal 4-cyano-4'-pentylbiphenyl (firm Merck) with positive dielectric anisotropy as a matrix. The temperature range of the nematic phase of this LC is usually located between 21.3°C and 35.2°C.

The single-walled carbon nanotubes (US, Research Nanomaterials, Inc.) were added into the liquid crystal with concentration of 0.5 wt. %. Then obtained mixture was shaken in a vortex mixer for 1 hour at temperature 50°C, followed by sonication with dispergator Ultrasonic Cleaner NATO CD-4800 (China) for 4 hours.

The cell had a sandwich structure and consisted of two plane-parallel glass plates whose inner surfaces were coated with thin transparent and conductive indium-tin-oxide (ITO) layer. Planar orientation of molecules was attained by coating the inner substrate surfaces with rubbed polyimide layers. For obtaining of homeotropic orientation of LC molecules, we used the surfactant (polysiloxane). The cell thickness was fixed with calibrated 20 μm polymer spacers for measurements. Both the colloid and the pure LC were injected into the empty cell by capillary action at the

isotropic state. To increase the dispersion, the cells with the colloid were placed at electric field of 40 V to achieve turbulence and were kept for 2 days. In this case, no aggregation of particles was observed. The stuffed cell was kept in the special heater with temperature regulator GL-100 (China). The copper-constantan thermocouple was used for temperature control. An accuracy of temperature determination was 0.1°C.

Dielectric and conductivity measurements were carried out by the Precision LCR Meter 1920 (IET Labs. Inc., USA) in the frequency range of 20 Hz – 1 MHz and at temperatures between 23°C – 43°C. In this case, applied voltage was 0.5 V for both LC molecular orientations.

A set-up for measurements of electro-optic parameters was assembled on the base of the Carl Zeiss polarization microscope. The electric impulses of the special form applied to the cell from the functional generator (model G6-28, Russia). A light, passing through the cell, fell on the photo diode and was registered by digital storage oscilloscope (model 6022BE, Hantek).

Switching times were defined from an electro-optic response by application of unipolar rectangular impulses while threshold voltage was defined using unipolar triangular impulses in quasi-static regime. Besides, a value of the threshold voltage was supervised under the polarization microscope.

3. RESULTS AND DISCUSSION

According to [2], nanoparticles do not disturb the director field of a LC, if the penetration length ξ is much smaller than their diameter D . The penetration length is defined as $\xi = K/W$, where K is some average of the Frank elastic constants, W is an anchoring energy of the nematic molecule at the particle surface. The values of the anchoring energy are within $10^{-4} - 10^{-6} \text{ J/m}^2$, elastic constants have the value about $6 \cdot 10^{-12} \text{ N}$, and D of single-walled nanotubes is equal to 1 nm. Elementary calculations show that the penetration length has an

order between $10^{-8} - 10^{-6}$. It is much more than the SWCNT diameter. Hence, the obtained colloids can be considered as a homogeneous media and they should behave as pure LCs but with the modified parameters.

Observation under polarization microscope has shown that the clearing temperature of the pure LC is located near 35.2°C while the nematic-isotropic transition of the colloid takes place at 37.1°C .

Rod-like particles of single-walled carbon nanotubes in nematic LC cause the effective orientational coupling with LC molecules [3]. The charges transfer from LC molecules to the particles and are distributed asymmetrically on the SWCNTs inducing a permanent dipole moment on them [4]. As a result, SWCNTs are oriented parallel to the LC director enhancing the order parameter S [5]. In this case, the isotropic-nematic transition temperature increases [6].

Fig. 1 and fig. 2 show the frequency dependence of real ϵ' and imaginary ϵ'' parts of dielectric permittivity of both the pure LC and the colloid for homeotropic and planar configurations, correspondingly, at temperature of 24°C .

The frequency dependence of ϵ' can be divided into three ranges. At low frequencies, an increase in dielectric permittivity occurs, which is associated with electronic exchange between electrodes and ions [7]. In this case, the nanotubes increase the double electric layer enhancing the field screening effect. In the middle frequency region, the dielectric permittivity remains almost unchanged and is connected with the bulk properties of the sample. And finally, relaxation of the liquid crystal and the colloid starts in the high-frequency range. As can be seen, the additive of carbon nanotubes increases the longitudinal component of real part ϵ' of dielectric permittivity while it decreases the transverse component in the middle frequency range. In particular, the longitudinal component increases from 19.55 to 20.56 and the transverse component decreases from 6.51 to 5.93 at the frequency of 2 kHz. As a result, the dielectric anisotropy increases from 13.04 to 14.63 at temperature 24°C . A presence of SWCNTs also decreases the value ϵ'' except for low frequencies at homeotropic configuration.

Temperature dependences of the real part of the dielectric permittivity of the colloid and the pure LC for both configurations at the frequency of 2 kHz are presented in fig. 3.

As can be seen, the longitudinal component of dielectric permittivity of the colloid is more and the transverse component is less than the corresponding value of the pure LC at all temperature up to the clearing point. The longitudinal and transverse components of the dielectric permittivity of the pure LC coincide above 35.2°C . It indicates that the isotropic-nematic transition occurs at the indicated temperature in the pure LC. While the components of the dielectric permittivity of the colloid are equalized at temperature of 37.1°C . Therefore, phase transition in the colloid rises to indicated temperature. This fact is consistent with observations under the polarization microscope.

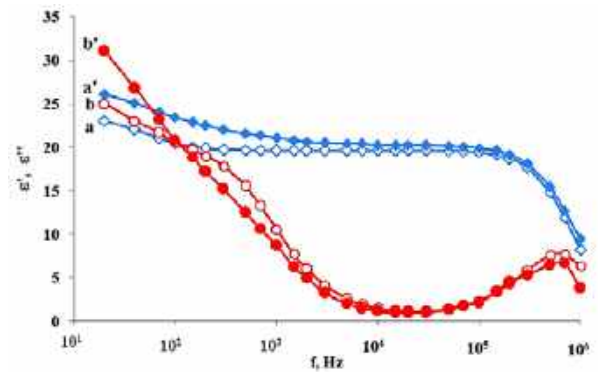


Fig. 1. Frequency dependence of real ϵ' and imaginary ϵ'' parts of dielectric permittivity at homeotropic configuration (temperature 24°C): (a) ϵ' of the pure LC, (a') ϵ' of the colloid, (b) ϵ'' of the pure LC, (b') ϵ'' of the colloid.

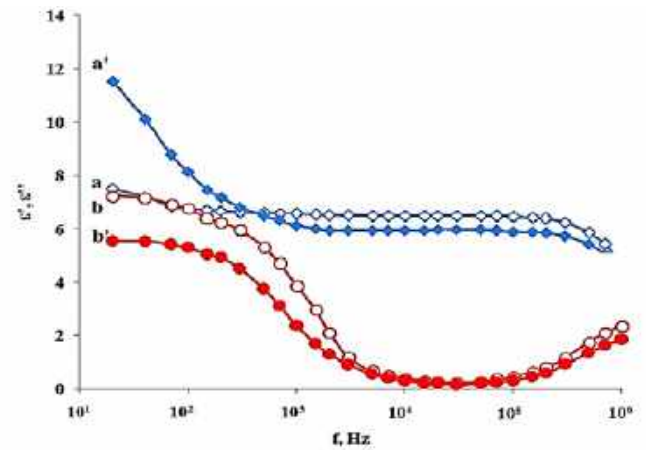


Fig. 2. Frequency dependence of real ϵ' and imaginary ϵ'' parts of dielectric permittivity at planar configuration (temperature 24°C): (a) ϵ' of the pure LC, (a') ϵ' of the colloid, (b) ϵ'' of the pure LC, (b') ϵ'' of the colloid.

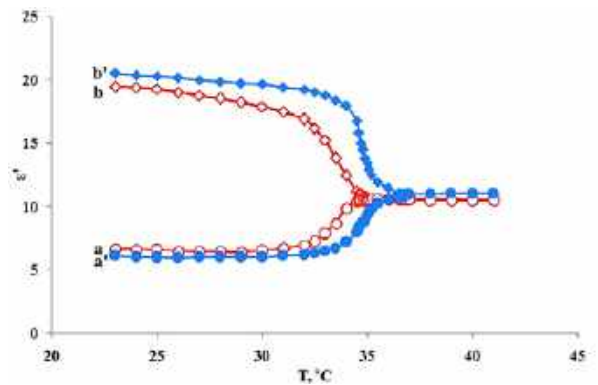


Fig. 3. Temperature dependence of components of dielectric permittivity at the frequency of 2 kHz: (a) the transverse component of the pure LC, (a') the transverse component of the colloid, (b) the longitudinal component of the pure LC, (b') the longitudinal component of the colloid.

The observable changes dielectric permittivity can be explained by the Maier-Meier theory for nematic LC according to which expressions for components of dielectric permittivity are defined as follows [8]:

$$\varepsilon'_{||} = 1 + \frac{NHF}{\varepsilon_0} \left\{ \gamma_{av} + \frac{2}{3} S \Delta\gamma + F \frac{p_e^2}{3k_B T} \left[1 - \frac{1}{2} (1 - 3 \cos^2 \beta) S \right] \right\}$$

$$\varepsilon'_{\perp} = 1 + \frac{NHF}{\varepsilon_0} \left\{ \gamma_{av} - \frac{1}{3} S \Delta\gamma + F \frac{p_e^2}{3k_B T} \left[1 + (1 - 3 \cos^2 \beta) S \right] \right\}$$

Dielectric anisotropy is the difference of these quantities:

$$\Delta\varepsilon' = \frac{NHF}{\varepsilon_0} \left[\Delta\gamma - F \frac{p_e^2}{2k_B T} (1 - 3 \cos^2 \beta) S \right]$$

where F is reaction field factor, H is the cavity form factor, $\gamma_{av} = (\gamma_{||} + 2\gamma_{\perp})/3$ is the average value of polarizability of LC molecules, $\Delta\gamma = \gamma_{||} - \gamma_{\perp}$ is the anisotropy of polarizability, N is the number of LC molecules per unit volume, S is the order parameter, β is an angle between the point molecular dipole p_e and the axis of maximum molecular polarizability, ε_0 is dielectric permittivity of vacuum, k_B is Boltzmann constant, T is Kelvin temperature. These expressions include quantity of molecules N per volume unit and the order parameter S . Since the concentration of the colloid is very small, the number of embedded particles per unit volume is also small. That is, the number of LC molecules per unit volume N decreases insignificantly. As shown above, the additive of nanotubes increases the order parameter S . The second term in the curly brackets of the expressions for components of dielectric permittivity containing the order parameter has different sign. It has the order parameter with a positive coefficient of $2/3$ for the longitudinal component, accordingly, this component increases at the additive of nanotubes while the transverse component decreases because of negative coefficient of $1/3$ of the same term. These inferences agree with our experimental data.

As can be also seen from figure 3, a maximum of dielectric absorption shifts to the high-frequency region from 640 kHz to 680 kHz. Fig. 4 shows the temperature dependence of the frequency of the dielectric absorption peak for the pure LC and the colloid.

As can be seen, the frequency of the dielectric absorption peak of the colloid is less than for the pure LC at all temperatures. The frequency of the dielectric absorption peak of the pure LC varies from 590 kHz (23°C) to 770 kHz (34°C) while it increases from 645 kHz (23°C) to 780 kHz (34°C) for the colloid.

The relaxation frequencies f_R follow the Arrhenius behavior by equation:

$$f_R = A e^{-\frac{W}{k_B N_A T}}$$

As may be inferred from this figure, the longitudinal component is more than the transverse one in the pure LC and the colloid at low and middle

where W is the activation energy of the flip-flop motion of the molecules about their short axes., A is some parameter, N_A is the Avogadro number. The slopes of the plots of $\log f_R$ versus the inverse of the temperature correspond to the activation energies along the director for the pure and the colloid, which equal to 27 kJ/mol and 23 kJ/mol, correspondingly. The activation energy decreases due to the presence of nanotubes. It indicates to that SWCNTs facilitates the flip-flop motion of the LC molecules.

As is well known, the relaxation time τ of LC molecules is characterized by flip-flop motion of molecules about their short axes. It is determined as follows:

$$\tau = \frac{1}{2\pi f}$$

where f is the frequency of the applied electric field. The addition of SWCNTs reduces the relaxation time from $2.7 \cdot 10^{-7}$ to $2.1 \cdot 10^{-7}$ s at 23° C and from $2.5 \cdot 10^{-7}$ s to $2.0 \cdot 10^{-7}$ s at 34° C. Obviously, the decrease of the relaxation time for the colloid connects to the decrease in viscosity. Temperature also affects on the relaxation time: an increase in temperature reduces viscosity. As a result, the flip-flop motion of LC molecules becomes easier.

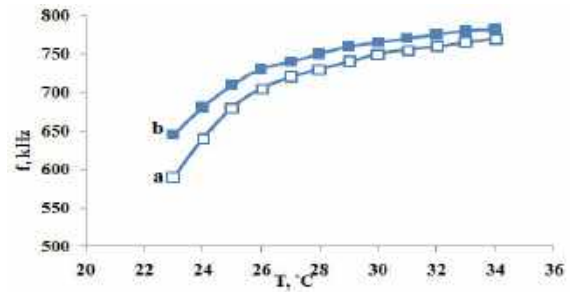


Fig. 4. Temperature dependence of the frequency of a local maximum of ε'' : (a) the pure 5CB, (b) the colloid.

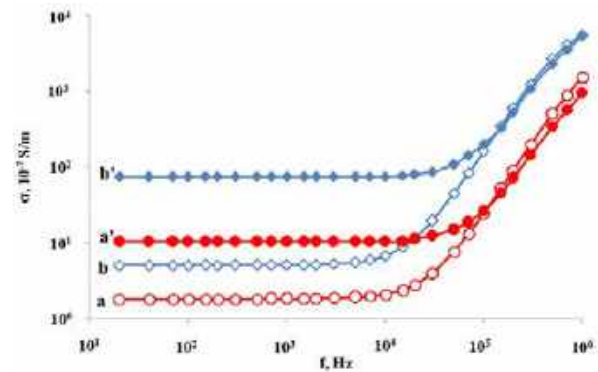


Fig. 5. Frequency dependence of specific conductance at temperature 24°C: (a) $\sigma_{||}$ of the pure 5CB, (a') $\sigma_{||}$ of the colloid, (b) σ_{\perp} of the pure 5CB, (b') σ_{\perp} of the colloid.

frequencies. This is due to the fact that it is easier for charges to move along the long axes of LC molecules (director). In this case, SWCNTs increase the

conductivity of both components. In such a case, the longitudinal component increases more than the transverse component. In particular, at the frequency of 2 kHz, the longitudinal component of conductivity increases from $5.2 \cdot 10^{-7}$ S/m to $7.4 \cdot 10^{-6}$ S/m while the transverse component increases from $1.9 \cdot 10^{-7}$ S/m to $1.1 \cdot 10^{-6}$ S/m. Starting from 15 kHz, the conductivity increases sharply. At high frequencies, conductivity of the colloid is less than for the pure LC.

The increase in conductivity is connected with the percolation phenomenon and high intrinsic electrical conductivity of carbon nanotubes. Continuous network of SWCNTs is formed in the colloid at a certain concentration called the percolation one. In this case, there is a transition from the ionic conductivity to the dominating charge hopping conductivity.

The conductivity of the LC at high frequencies is determined by the dielectric losses because molecular dipoles follow the electric field with some lag. There is the inhibition of the rotation of these dipoles in an alternating field. It is known that the corresponding conductivity can be represented by the Debye formula:

$$\sigma = 2\pi f \varepsilon_0 \varepsilon'' = \varepsilon_0 [\varepsilon(0) - \varepsilon(\infty)] (2\pi f)^2 \tau_D$$

where τ_D is the relaxation time for molecular dipoles which is determined as [8]:

$$\tau_D = \frac{\gamma}{2k_B T},$$

where γ is the rotational viscosity. The decrease in LC conductivity at high frequencies can be explained by a decrease in rotational viscosity at additive of SWCNTs into the LC.

The temperature dependences of specific conductance for the pure LC and the colloids are presented in fig. 6.

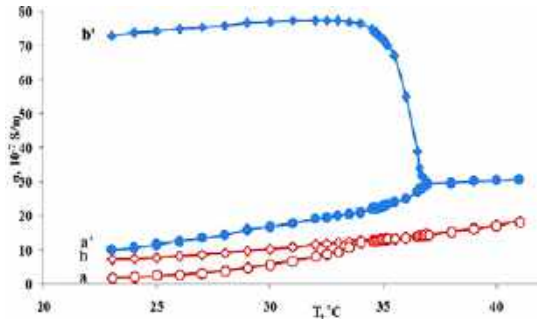


Fig. 6. Temperature dependences of specific conductance at the frequency 2 kHz: (a) $\sigma_{||}$ of the pure 5 CB, (a') $\sigma_{||}$ of the colloid, (b) σ_{\perp} of the pure 5CB, (b') σ_{\perp} of the colloid.

With increasing temperature, conductivity increases and the corresponding dependence obeys the Arrhenius law:

$$\sigma = \sigma_0 e^{-\frac{E}{k_B N_A T}},$$

where σ_0 is the pre-exponential factor, E is the activation energy of electrical conductivity. The value of E consists of the activation energy of the motion of the carriers and the energy necessary for the nucleation of new charges. It is an energy barrier which an ion must overcome to move inside a liquid crystalline medium. The larger the E , the harder the ions move within the LC layer and, accordingly, the lower the conductivity.

From the last expression, it is possible to find the activation energy of $E_{p||}$ of the pure LC and $E_{c||}$ of the colloid along the director, $E_{p\perp}$ of the pure LC and $E_{c\perp}$ of the colloid across the director, as well as the activation energy of $E_{p, is}$ of the pure LC and $E_{c, is}$ of the colloid in the isotropic phase. The method is the same as for the the activation energy of flip-flop motion of molecules. The calculated values of the activation energy are given in Table 1.

Table 1
Activation energy (in kJ/mol) of the pure LC and the colloid in the isotropic phase as well as nematic phase along and across director.

	$E_{ }$			E_{\perp}	E_{is}
Pure LC	39.6			85.4	56.3
Colloid	23.2			78.5	49.1

As one can see from this Table, the presence of SWCNTs decreases the activation energy of charges in nematic phase for both directions. That is, charges move inside the colloid with lesser exertion than in the pure LC.

The measurement of the threshold voltage of the Fredericksz effect by the electro-optical method showed that the addition of nanotubes increases it from 1.2 to 1.6 V.

According to [8], the threshold voltage U_F of the Fredericksz effect is determined by the following equation:

$$U_F = \pi \sqrt{\frac{K_{11}}{\varepsilon_0 \Delta \varepsilon}},$$

where K_{11} is splay elastic constant; ε_0 is the permittivity of vacuum; $\Delta \varepsilon$ is the dielectric anisotropy. This expression is true for colloids with a low concentration of particles and their small sizes. Using the numerical values of the threshold voltages and dielectric anisotropy, one can obtain the values of the elastic constants of the pure LC and the colloid. Calculations show that they are equal to $1.685 \cdot 10^{-11}$ N and $3.362 \cdot 10^{-11}$ N, respectively. That is, the additive of SWCNTs into LC increases its elastic constant.

The dependence of the rise time of the Fredericksz effect on the applied voltage for both the pure LC and the colloid is presented in fig. 7.

Apparently, the dependence of the rise time t_{on} on the voltage for both the pure LC and the colloid qualitatively corresponds to the expression [8]:

$$t_{on} = \frac{\gamma_1 d^2}{\varepsilon_0 \Delta \varepsilon (U^2 - U_F^2)},$$

where γ_1 is the rotational viscosity, d is the cell thickness, and U is the applied voltage, U_F is the threshold voltage of Fredericksz effect. Moreover, the rise time for the colloid is less than for pure LC at all voltage.

Fig. 8 shows the dependences of the decay time of the pure LC and the colloid on the applied voltage. As can be seen, the decay time of the colloid is less than the pure LC at all voltages. In addition, the decay time starts to increase slightly after the voltage of 6 V.

According to [8], the decay time is determined as follows:

$$t_{off} = \frac{\gamma_1 d^2}{\pi^2 K_{11}}$$

If we assume that this expression is true for a colloid then we can estimate the change in viscosity with the additive of SWCNTs. In particular, using the numerical values of the decay times and elastic constants at the applied voltage of 4 V, one can find the ratio of viscosities which is equal to $\gamma_{lc} = 0.25 \gamma_{lp}$, where γ_{lc} and γ_{lp} are the viscosities of the colloid and the pure LC, correspondingly. As can be seen, the viscosity decreases with the additive of SWCNTs into the liquid crystal. An increase in the decay time with voltage increasing may be associated with the occurrence of specific turbulence (fig. 9) in the colloid. In this case, the coupling between LC molecules and SWCNTs is violated. As a result, SWCNTs inhibit the relaxation of molecules to their initial state.

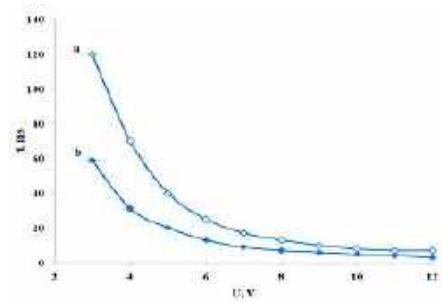


Fig. 7. Voltage dependence of the rise time of the Fredericksz effect: (a) the pure 5CB, (b) the colloid.

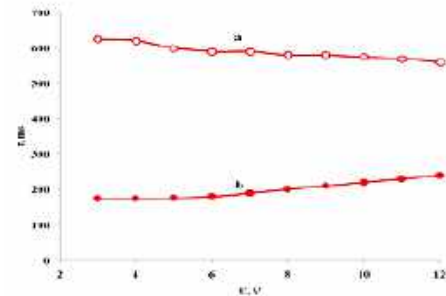


Fig. 8. Voltage dependence of the decay time of the Fredericksz effect: (a) the pure 5CB, (b) the colloid.

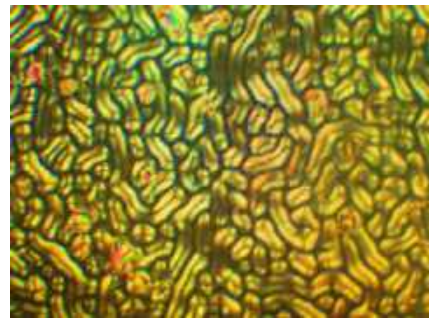


Fig. 9. The image under polarization microscope at the application of voltage of 6 V to the cell with the colloid.

- [1] N. R. Jber, A.A. Rashad, M. S. Shihab. Effects of carbon nanotubes on the physical properties of a nematic liquid crystal N-(4-methoxybenzylidene)-4-butylaniline. Journal of Molecular Structure, v. 1043, pp. 28–36, 2013.
- [2] S. V. Burylov, Yu. L. Raikher. Orientation of a solid particle embedded in a monodomain nematic liquid crystal. Phys. Rev. E, v. 50, pp.358-367, 1994.
- [3] D. Singh, U. Bahadur, S.M. Brushan, R. Dabrowski, R. Dhar. Improvement of orientational order and display parameters of liquid crystalline material dispersed with single-wall carbon nanotubes. Material Letters, v. 216, pp. 5-7, 2018.
- [4] K.A. Park, S.M. Lee, S.H.Lee, Y.H. Lee. Anchoring a liquid crystal molecule on a single-walled carbon nanotube. J. Phys. Chem. C, v.111, pp. 1620-1624, 2007.
- [5] I. Dierking, G. Scalia, P. Morales. Liquid crystal-carbon nanotube dispersions. Journal of Applied Physics, v. 97, pp. 044309-1-5, 2005.
- [6] M.V. Gorkunov, M.A. Osipov. Mean-field theory of a nematic liquid crystal doped with anisotropic nanoparticles. Soft Matter. v. 7, pp.4348–4356, 2011.
- [7] A.V. Koval'chuk. Low-frequency dielectric relaxation at the tunnel charge transfer across the liquid/electrode interface. Functional Materials. v. 8, No. 4, pp. 690-693, 2001.
- [8] L. Blinov. Structure and properties of liquid crystal, New York: Springer, p. 439, 2011.

Received: 03.06.2020

THE INVESTIGATION OF EQUILIBRIUM AND DYNAMIC CHARACTERISTICS OF DIELECTRIC POLARIZATION OF CHLOROBENZENE –n – BUTYL ALCOHOL SOLUTION

S.T. AZIZOV, G.M. ASKEROV

AZ 1143, H.Javid, ave.,131, ANAS Institute of Physics, Baku, Azerbaijan

e-mail: samir.azizov@mail.ru

The investigation data of equilibrium and dynamic characteristics of dielectric polarizations, the measurement results of dielectric constant ϵ' and absorption index ϵ'' of chlorobenzene - n – butyl alcohol system, are given in the article. The measurements are carried out on the frequencies 0,008; 0,04; 0,20; 0,50; 1,5; 5,0; 7,5 MHz at temperature from 20 up to -150° C; 25; 50; 500; 1000; 3000; 7500; 14000 MHz at temperature from 20 up to -40°C at alcohol content in mole percent $x = 0,000; 0,270; 0,526; 0,769; 1,000$.

Keywords: dielectric spectroscopy, dielectric constant, dielectric properties, chlorobenzene, n – butyl alcohol.

PACS: 61.20. – p; 77.22. – d; 77.22.Gm;

INTRODUCTION

The equilibrium and dynamic characteristics of dielectric polarization of chlorobenzene - n – butyl alcohol system are investigated in the work. The structure of studied solutions higher liquidus line is characterized by strong micro-heterogeneity which is formed in the presence of open hydrogen-bounded chains from alcohol and chlorobenzene molecules. The molecular movement in liquid solutions in interval liquidus-solidus differs by high clusterization. The devitrification phenomenon with following spontaneous crystallization is revealed at temperatures below the solidus line.

EXPERIMENTAL PART

The dielectric constants ϵ' and solution absorption coefficient ϵ'' of chlorobenzene - n – butyl alcohol system are measured on frequencies 0,008; 0,04; 0,20; 0,50; 1,5; 5,0; 7,5 MHz in temperature interval from 20 up to -150° C and also on frequencies 25; 50; 500; 1000;3000;7500;14000 MHz in temperature interval from 20 up to -40°C at content of butyl alcohol in mole percent $x = 0,000; 0,270; 0,526; 0,769; 1,000$. The equilibrium dielectric constants ϵ_0 are defined at twelve concentrations in temperature interval 20 ÷ -150°C. The low-frequency measurements are carried out at big absorption by

the method of inductively bounded contours [1]. The short-circuited line method is used in decimeter range, the variable thickness method [2] is used in centimeter range. The error of ϵ_0 , ϵ' and ϵ'' values is averagely $\pm 1\%$. The contribution of conduction dielectric loss in total absorption is taken under consideration at low frequencies.

The cooling is carried by liquid nitrogen. The measurements are carried out at continuous heating with velocity less 0,1 grad/min. The temperature is maintained by thermostat on super-high frequencies. The sample temperature is measures by thermocouple. Thermocouple error is less $\pm 0,3^\circ$.

RESULT DISCUSSION

The preliminary data and interaction character between system components can be obtained from state diagram. The temperature variation of ϵ_0 is obeyed to linear dependence in liquid state where components are mixed unlimitedly:

$$\epsilon_0 = A + \frac{B}{T} \quad (1)$$

The values of A and B constants for some concentrations x are given in table 1:

Table 1

x	0	0,109	0,270	0,426	0,526	0,625	0,769	1,00
A	1,58	1,32	-1,20	-11,2	-14,3	-15,2	-17,5	-18,6
$10^{-3} \cdot B^\circ C$	1,22	1,38	2,35	5,65	7,00	7,82	9,20	10,8

At addition of chlorobenzene to alcohol the derivative $\frac{\partial \epsilon_0}{\partial (1/T)}$ firstly decreases relatively slowly and it strongly decreases below values $x \sim 0,4$. Especially in this concentration region there are the most inclinations ϵ_0 from additivity. The discussion of inclination reasons from additivity can be considered in terms of equilibrium orientational polarization. According to Kirkwood - Frohlich we have:

$$P = \frac{(\epsilon_0 - \epsilon_\infty)(2\epsilon_0 + \epsilon_\infty)}{\epsilon_0(\epsilon_\infty + 2)^2} \quad V = \frac{4\pi N \mu_0^2}{9kT} g \quad (2)$$

where ϵ_∞ is dielectric constant caused by electronic and atomic contributions in polarization, μ_0 is dipole moment of isolated molecules, V is molar volume, N is Avogadro number, g is correlation parameter taking under consideration the short-range forces. For aliphatic alcohols the model of hydrogen-bounded molecular chains of alternative length with limited

rotation round the bounds of molecular chains [3,4], allows us to describe the observable temperature variation of g parameter. The small g parameter values at high temperatures are caused by decrease of length of molecular chains under influence thermal motion and big g parameter values at low temperatures are caused by increasing rotation slow at which the orientational correlation of neighbor dipoles becomes more effective one.

Within the framework of this model the dilution of n – butyl alcohol in chlorobenzene should be accompanied by redistribution of chains by lengths in favor of shortest lengths and monomers. This leads to the appearance of negative inclinations of ε_0 from additivity because of decrease of hydrogen bond number in volume unit. The character of temperature variation of inclinations is agreed with hypotheses on the bond between thermal motion energy and chain depolymerization process.

The short chains transit into more stable close multimers, often dimers which have the practically zero dipole moment and don't contribute into polarization in chemically inert solvents. That's why the clear minimum [5] appears at small parts of alcohol on $P(x)$ dependence curve. If we take under consideration in first approximation that polarization of P_1

chlorobenzene doesn't depend on composition, then P_2 alcohol polarization is determined by the expression:

$$P_2 = \frac{P_{12} - (1-x)P_1}{x} \quad (3)$$

where 12 index is related to solution.

Such interaction is connected with proton-accepter properties of benzene ring. Indeed, according to data of NMR method [6] the open dimers dominate in diluted benzene solutions.

The treatment results in the terms of two independent relaxation processes, each of which has the one relaxation time τ , are calculated by the formula:

$$\varepsilon^* = \varepsilon' - i\varepsilon'' = \frac{C_1}{(1+i\omega\tau_1)} + \frac{C_2}{(1+i\omega\tau_2)} \quad (4)$$

where $C_1 + C_2 = 1$, $C_1 = \frac{\varepsilon_0 - \varepsilon_{\infty,1}}{\varepsilon_0 - \varepsilon_{\infty,2}}$; $\varepsilon_{\infty,1}$ is high-frequency limit of low-frequency absorbing region, $\varepsilon_{\infty,2}$ is high-frequency limit of high-frequency absorbing region (table 2). The relaxation parameters of pure component of main dispersions are also given in table 2. The inclinations of dielectric coefficient values calculated by (4) and data of table 2 from experimental ones don't exceed $\pm 2\%$ for ε' and $\pm (5-7)\%$ for ε'' .

Table 2

x	$t, ^\circ\text{C}$	ε_0	$\varepsilon_{\infty,1}$	$\varepsilon_{\infty,2}$	$10^{12} \cdot \tau_1, \text{sec}$	$10^{12} \cdot \tau_2, \text{sec}$
0,000	20	–	5,72	2,58	–	12,5
	0	–	6,08	2,62	–	16,3
	– 20	–	6,44	2,68	–	22,0
	– 40	–	6,80	2,74	–	30,2
0,270	20	6,80	5,50	2,60	164	12,0
	0	7,52	5,70	2,65	330	15,0
	– 20	8,15	5,92	2,70	790	21,0
	– 40	8,95	6,18	2,77	2100	29,4
0,526	20	9,50	5,20	2,56	360	12,5
	0	11,5	5,30	2,62	750	15,0
	– 20	13,4	5,44	2,72	2160	21,0
	– 40	15,7	5,62	2,75	6340	30,0
0,769	20	13,8	4,50	2,55	515	12,5
	0	16,4	4,60	2,60	1200	15,6
	– 20	19,0	4,68	2,65	3160	21,0
	– 40	22,1	4,78	2,70	9600	30,0
1,000	20	18,1	3,38	–	630	–
	0	21,2	3,44	–	1400	–
	– 20	24,3	3,53	–	3700	–
	– 40	27,9	3,59	–	11000	–

From consideration of table 2 it is followed that:

1. The relaxation times of the first region are close to corresponding values for the main absorbing region of n – butyl alcohol. The significant diversions appear only at $x \leq 0,5$.

2. The relaxation times and activation energies of the second region don't practically differ from the same ones for the main absorbing region of pure chlorobenzene at all studied concentrations.

3. The extrapolation $\varepsilon_{\infty,1}$ gives values ε_0 of chlorobenzene at $x \rightarrow 0$ and at $x \rightarrow 1$ it gives the values of

high-frequency limit of the main dispersion of n – butyl alcohol.

Thus, the given system in liquid phase is heterogeneous one at molecular level and it consists of clusters. Taking under consideration the investigation results at equilibrium, we can't consider these clusters not depending on each other. The direction in which the relaxation times change in solution will be defined by interaction nature between molecules of the one and the same cluster, and both of them.

The main dispersion region in n – butyl alcohol is interpreted on the base of cluster decay processes [7]

consisting of elongated chains because of breaking of hydrogen bonds under the influence of thermal motion with the following orientation of released molecules. Moreover, the relaxation time is determined by duration of cluster existence. The chain lengths don't practically differ on ones existing in pure state at big concentrations of *n* – butyl alcohol. The insignificance of τ_1 change proves this fact. Along with monomer molecules of *n* – butyl alcohol, the chlorbenzene molecules weakening the hydrogen bond are situated between chains. This leads to more rapid τ_1 decrease.

The strong decrease concentration of free hydroxyls in the system is the evidence of another proton-acceptor behavior of the solvent that is expressed in the apparent absence of additive absorption contribution observed in *n* – butyl alcohol at micro-waves [8]. One can suppose that complexes of *n* – butyl alcohol – chlorbenzene will take part in low-frequency absorption. Such possibility is confirmed by the almost threefold decrease of critical frequency corresponding to monomer relaxation of *n* – butyl alcohol at transition from pure liquid into diluted benzene solution [9].

The absorption below liquidus line is presented by one region which is mainly related to *n* – butyl alcohol. The relaxation is characterized by asymmetric ($x = 0,270$ and $0,526$) and ($x = 0,769$) symmetric distributions and is described by equations [2, 10]:

$$\varepsilon^* - \varepsilon_\infty = \frac{\varepsilon_0 - \varepsilon_\infty}{(1 + i\omega\tau)^\beta}, \quad 0 < \beta < 1, \quad (5)$$

$$\varepsilon^* - \varepsilon_\infty = \frac{\varepsilon_0 - \varepsilon_\infty}{[1 + (i\omega\tau)^{1-\alpha}]}, \quad 0 < \alpha < 1, \quad (6)$$

where β and α are distribution parameters.

The change character of relaxation parameters at transition through the liquidus line has many common details with the behavior of bromobenzene – benzene system where the jump of relaxation time τ and increase of U activation energy value are observed. Considerably, that in both systems the relative increase of relaxing component part in liquid solutions with temperature decrease doesn't correspond to bigger time increase. The high dormancy of relaxation process is caused by the presence of one of the components in solid state. The dispersion asymmetry is the consequence of clusterization processes [11].

In terms of this model the asymmetric distribution should observe in that case if the diffusion time is equal to or bigger than dielectric rotation time. According to this system, this means that the duration of existence of hydrogen-bounded chains is big one and molecules relax without chain dissociation.

CONCLUSION

The samples enriched by the alcohol are easily cooled and frozen in the glass form at transition to the temperature regions below solidus. The samples rapidly cooled up to liquid nitrogen temperature (~ 1 grad/min), the heating leads to the devitrification and reconstruction of supercooled state. The spontaneous crystallization takes place at temperatures $\sim -120^\circ\text{C}$ that is proved by ε' jump decrease up to value which is less than ε' of glass and ε' jump increase in melting point.

-
- [1] Y.Y. Akhadov. Dielectric parameters of pure liquids, Moscow, (1999), 854.
 - [2] Ch. Kadjar, Sh.K. Agamuradova, S.T. Azizov. The investigation of dielectric properties of strongly absorptive liquids and their solutions, AJP Fizika, vol. XIV, №2, Baku, (2008), 56 – 59.
 - [3] S. Sudo, N. Shinyashiki, Y. Kitsuki, S.Yagihara, Dielectric Relaxation Time and Relaxation Time Distribution of Alcohol – Water Mixtures, J. Phys. Chem.106, 3, (2002), 458 – 464.
 - [4] S.T. Azizov, O.A. Aliev, R.G. Abaszade. "Equilibrium and dynamic properties of dielectric polarization of chlorobenzene-n-butyl alcohol system", Abstrct books of Young scientists conference on semiconductor physics "Lashkarov's reading" Kyiv, Ukraine, April 3-5, 2019, p. 68.
 - [5] W. Dannhauser, L.W. Bahe. J. Chem. Phys., 40. 3058, 1964.
 - [6] S.T. Azizov. Dielectric properties of some amides and their solutions in dioxane, ANAS Transactions, Physics-Math, Astronomy, №2, vol. XXV, Baku, (2014), pp. 74–80.
 - [7] S.T. Azizov, O.A. Aliev, R.G. Abaszade. "Low – frequency dielectric properties of acetone", International Journal of Latest Research in Science and Technology, 5, (2016), 58-62.
 - [8] L.M. Imanov, K.E. Zulfigarzade, Z.A. Bafadarov, L.A. Kuliyeu. Journal of Physical chemistry, vol. 40, (1966) 1271.
 - [9] L.M. Imanov, F.G. Mirzoyev, K.E. Zulfigarzade. Journal of Physical chemistry, vol.39, (1965), 2836.
 - [10] R. Liebaert, Y. Leroy. Magnettic and Electric resonance and relaxation, Amsterdam, (1963), 316.
 - [11] J.L. Daschbach, B.M. Peden, R.S. Smith, B.D. Kay. Adsorption, desorption, and clustering of H₂O on Pt (111), J. Chem. Phys.120, 3, (2004) 1516 – 1523.

Received: 12.05.2020

DIELECTRIC RELAXATIONS OF CHLORBENZENE-BENZENE AND CHLORBENZENE-N-HEXANE SOLUTIONS

S.T. AZIZOV

*Institute of Physics of ANAS, AZ 1143, H.Javid ave., 131, Baku,
Azerbaijan e-mail: samir_azizov@mail.ru*

The measurement results of dielectric constant ϵ' and absorption coefficient ϵ'' obtained for concentrated solutions chlorobenzene-benzene, chlorobenzene-n-hexane at wave lengths $\lambda = 12,80$ and $\lambda = 3,26$ cm at temperature 20°C are given in the article. The static dielectric constant is obtained at frequency 1MHz. The obtained experimental values ϵ', ϵ'' and ϵ_0 of investigated systems in (ϵ', ϵ'') plane locate on the semi-circle the center of which is on ϵ' axis. In this case the high-frequency limit value of ϵ_∞ dielectric coefficient exceeds the corresponding n^2 refraction index square. The macroscopic and molecular relaxation times are calculated on the base of experimental data.

Keywords: dielectric spectroscopy, dielectric relaxation, dielectric properties of chlorobenzene-benzene, chlorobenzene-n-hexane solutions.

PACS: 61.20. – p; 77.22. – d; 77.22.Gm;

INTRODUCTION

The increased values of dielectric relaxation times in comparison with their values in diluted solutions are usually observed in pure dipole liquids. If in the first case the relaxation process is the cooperative one, then the relaxation time characterizes the separate molecule in diluted solutions. In this connection the investigation of dielectric relaxation dependence on polar molecule concentration is of great interest.

On the example of carried out double system investigations one can confirm that the concentration dependence of τ relaxation time ratio to η viscosity can be used for the evaluation of clusterization degree of polar molecules [1]. As a result, one can define the special relaxation mechanism in the case of concentration solutions of some cyclohexane derivatives in nonpolar solvents [2].

In some works, [3 – 5] the explanation of dielectric properties of some systems in micro-wave range on the base of perception on concentration fluctuation, is given.

In present work the investigation results of dielectric relaxation of chlorobenzene-benzene, chlorobenzene-n-hexane in microwave range are presented. The data of dielectric relaxation is expanded on the region of investigated concentration solutions.

The dielectric constant ϵ' and absorption coefficient ϵ'' of double systems chlorobenzene-benzene, chlorobenzene-n-hexane in total concentration interval are measured at wave lengths $\lambda = 12,80$ and $\lambda = 3,26$ cm at temperature 20°C . Besides, the static dielectric constant of these systems in total concentration interval at frequency 1MHz and temperature 20°C is measured.

EXPERIMENT TECHNIQUE

The data at $\lambda = 12,80$ cm are obtained by the method described in [6]. In the comparison with the known method Roberts-Hippel [7] consisting in measurement of input impedance of short-circuit transmission line filled by investigated dielectric, in the given method the transformation of this impedance on

measuring line input is carried out in such way that the optimal measurement conditions in the case of strongly absorbing substances are formed. The deviations from average values are 1% for ϵ' and 3% for ϵ'' .

The method [8] which leads to measurement of standing-wave factor dependence on height of liquid column short-circuit waveguide is applied at wavelength $\lambda = 3,26$ cm. The deviations from average values don't exceed 1% for ϵ' and 2% for ϵ'' .

The measurements at frequency 1MHz are carried out on Q-meter. The deviations from average values are less than 1%.

RESULTS AND THEIR DISCUSSION

The measurement results of ϵ' dielectric constant, ϵ'' absorption coefficient and static dielectric constant ϵ_0 for the studied systems are given in tables 1,2. Further, there are values of τ_M macroscopic and τ_μ molecular relaxation times. The polar component concentration in mole percent is designated by x.

τ_M calculation is carried out on the following formulas:

$$\tau_M = \frac{1}{\omega} \frac{\epsilon''}{\epsilon' - \epsilon_\infty} \quad (1)$$

$$\tau_M = \frac{1}{\omega} \frac{\epsilon_0 - \epsilon'}{\epsilon''} \quad (2)$$

where ω is circular frequency of applied field.

τ_M values, obtained by above mentioned two formulas, well agree in 3 – 5% limits and only in several cases at very small difference $\epsilon_0 - \epsilon'$ the values defined by (2) more deviate from average values. That's why one can suppose that the values of high-frequency dielectric constant ϵ_∞ given in tables 1,2 are real ones. Note that ϵ_∞ value in all cases for the pure polar component exceeds the corresponding n^2 refraction index square. The difference $\epsilon_\infty - n^2$ monotonously decreases as far as dilution of solution. These results well agree with data of [9] in which the analogous phenomena in solutions of halogenated benzene are observed. The supposition on presence of additional absorbing region of resonance character at

DIELECTRIC RELAXATIONS OF CHLORBENZENE-BENZENE AND CHLORBENZENE-N-HEXANE SOLUTIONS

more high frequencies is made on the base of these data. Such proposition is enough proved only in the case of overlapping of bigger frequency interval and first of all

of the submillimeter range. The low-temperature measurements can be the additional information source.

Table 1

chlorbenzene-benzene								
X	ϵ_0	ϵ_∞	$\lambda=12,80$ cm		$\lambda=3,26$ cm		$\tau_M \cdot 10^{11}$ sec	$\tau_\mu \cdot 10^{11}$ sec
			ϵ'	ϵ''	ϵ'	ϵ''		
0,000	2,28	2,28	2,28	—	2,28	—	0,87	0,87
0,179	3,07	2,34	3,06	0,10	2,90	0,31	0,95	0,88
0,368	3,84	2,40	3,81	0,22	3,45	0,64	1,05	0,92
0,567	4,60	2,46	4,54	0,35	3,97	0,98	1,14	0,96
0,778	5,20	2,52	5,12	0,45	4,34	1,25	1,19	0,99
1,000	5,70	2,58	5,60	0,54	4,63	1,47	1,25	1,02

Table 2

chlorbenzene-n-hexane								
X	ϵ_0	ϵ_∞	$\lambda=12,80$ cm		$\lambda=3,26$ cm		$\tau_M \cdot 10^{11}$ sec	$\tau_\mu \cdot 10^{11}$ sec
			ϵ'	ϵ''	ϵ'	ϵ''		
0,000	1,89	1,89	1,89	—	1,89	—	0,60	0,60
0,243	2,63	2,03	2,62	0,06	2,57	0,21	0,68	0,63
0,461	3,40	2,16	3,38	0,14	3,20	0,46	0,77	0,68
0,658	4,15	2,31	4,12	0,24	3,76	0,77	0,88	0,75
0,837	4,92	2,44	4,86	0,38	4,24	1,11	1,07	0,89
1,000	5,70	2,58	5,60	0,54	4,63	1,47	1,25	1,02

Table 3

system	γ on formula (3)	γ on formula (4)	γ on formula (5)
chlorbenzene-benzene	1,17	1,17	1,17
chlorbenzene-n-hexane	0,83	1,67	1,23

The molecule orientation is lightened at solution dilution. The transition from τ_M to τ_μ leads to the insignificant quantitative changes. It is known that the difference between τ_M and τ_μ is in the fact that so-called “inner field” existing in pure dipole liquids significantly decreasing as far as dilution in nonpolar solvents, is taken under consideration at τ_M definition. $\tau_\mu = \tau_M$ can be accepted at infinite dilution.

That's why one can use τ_M values in pure liquid and extrapolated ones to infinite dilution for finding of γ multiplier taking under consideration the inner field in pure polar liquid. We use the relation from [10]:

$$\gamma = \frac{\tau_M}{\tau_\mu} = \frac{\tau_{M1} \eta_2}{\tau_{M2} \eta_1} \quad (3)$$

where η is liquid viscosity, index1 corresponds to pure liquid, index 2 corresponds to infinite dilution in nonpolar solvent.

By other side, the theoretical expression for γ value has the following form:

$$\gamma = \frac{\epsilon_0 + 2}{\epsilon_\infty + 2} \quad (4)$$

$$\gamma = \frac{3\epsilon_0}{2\epsilon_0 + \epsilon_\infty} \quad (5)$$

The results of corresponding calculations are given in table 3.

From the table, it is followed that Debye expression for γ significantly deviates from experimental data. The comparably best agreement takes place at the use of formula (5) by which τ_μ values given in table 1,2.

The divergences in n-hexane case are probably connected with the direct proportionality between relaxation time and viscosity. Indeed, if the viscosity of n-hexane is 2,5 times less than chlorbenzene one, then τ_μ changes only in 1,7 times. By other side, the benzene viscosity is less in 1,24 times than chlorbenzene one, whereas τ_μ decreases in 1,16 times. If we consider that extrapolation is associated with some error, then we should recognize the presence of proportionality between τ and η values in benzene solution. According to solution in n-hexane, then the molecule mobility is less than one can expect proceeding of viscosity changes. This is proved by the fact that double viscosity decrease is accompanied by 30% τ_μ decrease for chlorbenzene at transition from benzene to n-hexane. It is significant that the deviations from proportionalities between τ and η values are weak ones at significant concentrations of polar molecules.

CONCLUSION

At wave lengths $\lambda = 12,80$ and $\lambda = 3,26$ cm and temperature 20°C the dielectric constant ϵ' and absorption coefficient ϵ'' of double system chlorbenzene-benzene, chlorbenzene-n-hexane are measured.

The values of macroscopic and molecular relaxation times are calculated on the base of experimental data. The possibility of existence of additional absorption region at more high frequencies is noted. The dependence of relaxation process on viscosity and also on sizes and forms of solvent molecules is investigated.

-
- [1] *Ch.O.Kajar, S.T.Azizov, Sh.K. Agamuradova.* "The investigation of dielectric properties of strongly absorbing liquids and their solutions" , *AJP Fizika*, 2008, XIV, En № 2, p.56 – 59.
- [2] *V.A. Durov, O.G. Tereshin.* Modeling of supramolecular ordering and physic – chemical properties in cyclohexane ethanol mixtures. *J. Phys. Chem. B.*, 2006, 110, p. 8441-8450.
- [3] *R.M. Villamanan, M.C .Martin, C.R. Chamorro, J. Segovia.* "Vapor-liquid equilibrium of binary and ternary mixtures containing isopropyl ether, 2 – butanol, and benzene at T =313.15 K", *J. Chem. Eng.*, 51, 2006, 148 – 152.
- [4] *M.C. Grande, J.A. Julia, M. Garcia.* On the density and viscosity of (water + dimethylsulphoxide) binary mixtures. *J. Chem. Therm.*, 2007, 39, p.1049 – 1056.
- [5] *S. Sudo, N. Shinyashiki, Y. Kitsuki, S. Yagihara,* "Dielectric relaxation time and relaxation time distribution of alcohol – water mixtures" *J. Phys. Chem.*, 2002, p. 458 – 464.
- [6] *S.T. Azizov, O.A. Aliev, R.G. Abaszade.* "Low – frequency dielectric properties of acetone", *International Journal of Latest Research in Science and Technology*, 5, 2016, p. 58-62.
- [7] *A.R. Hippel.* Dielectric and their application, M., 1959, p.335.
- [8] *Y.Y. Akhadov,* Dielectric parameters of pure liquids, Moscow, 1999, p. 854.
- [9] *S.T. Azizov, K.E. Zulfugarzade, O.A. Aliyev,* "Dielectric relaxation of halogenated benzene in microwave range", *APJ Fizika XXIII*, En № 4, 2017, p. 22 – 26.
- [10] *R.C. Miller, C.P. Smyth.* "Microwave absorption and molecular structure in liquids. The effect of internal field upon molecular relaxation times in liquids" *J. Amer. Chem. Soc.*, 79, 1957, p. 3310.

Received: 08.06.2020

CHARACTERIZATION OF OPTICAL PARAMETERS AND EVALUATION OF THE QUANTUM YIELD OF THE LED PHOSPHOR LAYER

T.Y. ORUJOV^{1,2}

¹*Institute of Physics, Azerbaijan National Academy of Sciences, Baku, Azerbaijan*

²*Research and Development Center for High Technologies, Ministry of Transport, Communications and High Technologies*

This paper studies absolute photoluminescence as well as the quantum yield of phosphors (YAG: Ce) used in the manufacture of LEDs. The interactions between light and phosphor samples with and without silicone dispersion were investigated, since the optical properties of luminescent materials have a great influence on the efficiency of LEDs. From the calculations of the reflected, absorbed and transmitted radiation in the phosphor, the quantum yield of the phosphor was evaluated.

Keywords: LED, phosphor, luminescence spectrum, quantum yield

PACS: 42.25.Bs, 78.55.-m, 78.66.Sq

INTRODUCTION

Phosphor conversion is the most common method for achieving white light using single LED chips. Among the mainstream and most commonly used phosphors is the yellow YAG: Ce phosphor (known to have high quantum efficiency), which is usually pumped by a blue (450 nm) light energy source. This simple and effective method produces a white LED with a color rendering index of 70-80. It is known that only a limited number of phosphors can be used as conversion materials due to the many requirements for the realization of the spectrum conversion process. These phosphors should have wide enough excitation and emission spectra and energy conversion to provide the required CRI and quantum efficiency. Phosphors must also provide a high fluorescence quantum yield and high thermal stability. They are expected to have a small particle size and a uniform spherical morphology to reduce scattering, improve quantum efficiency, and be easily mixed in matrices of silicones, epoxies, and other resins.

The precise characterization of phosphors used in LEDs for solid state lighting is important for understanding the extraction efficiency and light conversion in LED devices [1]. An accurate assessment of the photoluminescence (PL) efficiency of phosphors is a difficult task, mainly due to the difficulty of understanding the behavior of reflected and transmitted light (scattered and transmitted), as well as the need for accurate estimation of light losses in the optical range. When the light wave hits the silicone/phosphor layer, several things can occur. Light can reflect against the surface, be selectively absorbed by the phosphor, scattered by the phosphor particles (differently depending on the particle size), converted to different wavelengths, or transmit through the layer. That is why an accurate understanding and explanation of the processes describing the interaction of the particles of light with the phosphor is necessary [2,3]. The quantum yield of a luminescent material is defined as the ratio of the number of emitted photons and the number of photons absorbed by the irradiated sample; it characterizes the radiative transition in combination

with the luminescence lifetime, the luminescence spectrum and the stability of the phosphor.

Quantum yield is a criterion for the selection of luminescent materials used in solid state lighting devices. Knowledge of the quantum efficiency provides important feedback in the development of new synthesis methods for the various luminescent materials in research. Despite the importance of an accurate assessment of the quantum yield of luminescent materials, there are very few studies in the literature devoted to the study of its absolute values [4,5]. In these references, the photoluminescence quantum yield value for the yellow phosphor YAG: Ce is often quoted as being greater than 90%.

The behavior of incident radiation interacting with samples of different absorption and diffusion properties cannot be thoroughly studied, since the reflected and transmitted light are not differentiated in the integrating sphere. Measuring the reflected and transmitted light separately will give more information about the interaction of light with the phosphor: the amount of reflected and transmitted converted light, the difference in the ratio of yellow and blue components between reflected and transmitted light. These effects are due to the physical properties of the phosphors (absorption, particle size and concentration). Thus, analyzing the properties of both reflected and transmitted light gives a deeper look at these phenomena, which is important for optimizing LEDs.

EXPERIMENTAL PART

To study the characteristics of the phosphor, an integrating sphere with a diameter of 30 cm was used. The setup is shown schematically on fig. 1. The sample was placed at the input slit on the wall of the sphere, so that one of the sides of the sample was facing the outside of the sphere. To register the photons reflected from the sample (blue and yellow), the source of exciting emission must illuminate the sample from the inside of the sphere, the reflection from which is measured by a spectrophotometer, optically connected to the sphere. For this purpose, an optical cable is inserted into the sphere, which has an optically non-

absorbing coating, the exciting radiation of which is concentrated on the sample. To register the photons transmitted through the sample, the sample should be illuminated from outside of the sphere, with the light scattered and emitted by the phosphor being measured with a spectrophotometer. The integrating sphere and the applied measuring equipment used in the experiment were from Everfine (PMS-80 Spectrophotocalorimeter).

To determine the absolute values of the reflected and transmitted radiation for commercial phosphors, firstly, the power of the initial blue radiation was measured in the integrating sphere. The spectrophotometer measures the spectral flux distribution (W/nm), which allows the direct calculation of power values for individual wavelengths as well as reflected and transmitted components of total optical power. YAG:Ce phosphor with a peak emission wavelength of 550 nm dispersed in silicone epoxy at a concentration of 0.5 g/cm³ was used as a sample, and also the same phosphor compressed into a tablet without the epoxy. The density was maintained equal in both samples, so as to keep the same amount of phosphor across its thickness. The concentration of phosphor in the silicone was 10% because the density

of the phosphor particles in a 10% sample ($\sim 9 \times 10^4$ particles/mm³) is of the same order of magnitude as the density of the phosphor commonly found in LED packages.

To evaluate the influence of the clear encapsulating material on the transmittance of the luminescent layer, the transmission properties of the silicone epoxy were measured on a linear optical bench. By placing the sample between the light source and the detector, the light emitted by the control LED was transmitted through the silicone layer and compared to a measurement of the emission from just the light source. Resulting data was obtained by subtracting these two data sets.

RESULTS

Figure 2 shows the emission spectra of the excitation source and the phosphor. An important requirement for the measurement of the quantum yield of the phosphor is that the excitation spectra of the pump source and the phosphor do not intersect. It can be seen that the emission spectra do not overlap, which makes it possible to calculate the energy distribution of the two spectra.

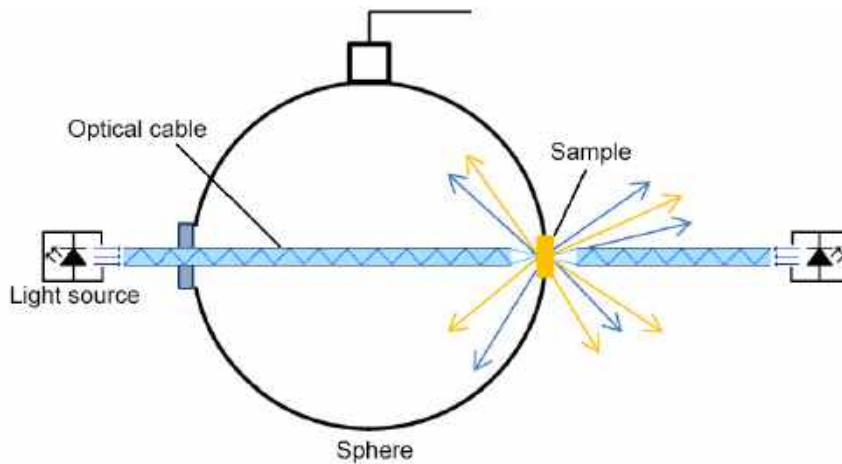


Fig. 1. Schematic representation of an integrating sphere for measuring the properties of a phosphor.

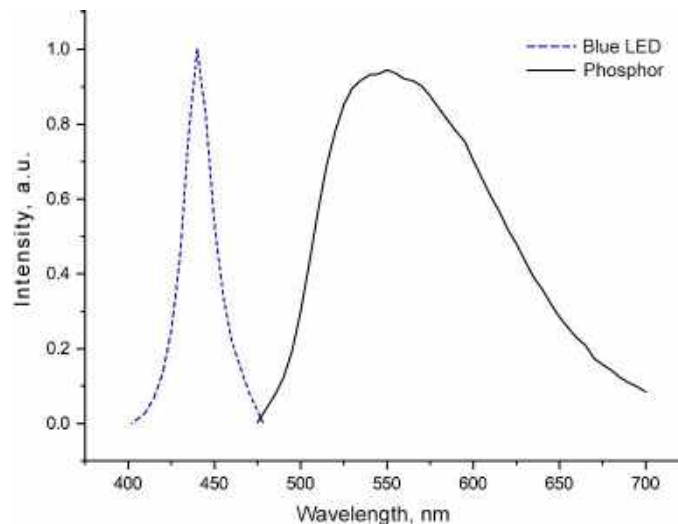


Fig. 2. Spectral distribution of the LED and phosphor.

YAG:Ce phosphor properties

Table 1

Emission	Initial, W	Reflected, W	Transmitted, W	Loss, %
Free phosphor				
Yellow	10	2.8	4.2	11
Blue		0.6	1.3	
Dispersed phosphor				
Yellow	10	2.7	4.1	13
Blue		0.6	1.3	

The measurement results shown in Table 1 showed that 34% of the initial light energy is lost just as a result of reflection at the phosphor particles. Another 11% of the optical power is wasted on the non-radiative absorption of blue photons by the phosphor. These losses are due to the Stokes shift and the quantum efficiency of the phosphor. As a result, the power of the initial irradiation not involved in the output emission is equal to:

$$F_{e_{loss}} = F_{e_{total}} - (F_{e_{ref}} + F_{e_{tr}}) \quad (1)$$

By converting the luminous power values into photon count values, the quantum yield of the phosphor can be calculated using the following expression [6]:

$$\eta_l = \frac{N_e}{N_b} = \frac{N_e}{N_b^{total} - (N_b^{ref} + N_b^{tr})} \quad (2)$$

where N_e is the number of photons emitted by the phosphor, N_b is the number of photons emitted by the blue LED, N_b^{ref} and N_b^{trans} are the reflected and transmitted blue photons, respectively.

The quantum yield in case of the phosphor dispersed in silicone epoxy was $93.2\% \pm 0.5\%$, while the quantum yield of the free phosphor was $91.2\% \pm 0.5\%$. Errors in quantum efficiency values were estimated by calculating the standard deviation from experimentally measured averaged quantum efficiency values from 10 different measurements.

Emission transmission in the silicon epoxy was within the 99% range for visible wavelengths, although there will always be a small shift of this value in the 380 nm to 780 nm range. Multiple reflections within the silicone layer result in only small transmission losses, which are wavelength dependent. This effect explains the shift in color coordinates to a slightly more

reddish wavelength when the phosphor is mixed with transparent polymers or silicones.

Considering all the above, it can be stated that the traditional method of dispersing phosphor particles in silicones is not ideal for efficient photon extraction. To fully extract the reflected photons, it would be necessary to redirect them back using a 100% reflector placed on the die substrate surface. However, this approach does not solve the problem of yellow reflected photons, which will not excite the phosphor even if redirected backward. In phosphor converted white LEDs, low efficiency to a certain extent is an inherent property of the phosphor, which can only be improved by increasing the quantum efficiency. However, the isotropic nature of the emission of the phosphor converted light leads to the fact that approximately half of the converted light must undergo multiple reflections between the phosphor layer and the LED chip on the substrate, which will also lead to a certain decrease in efficiency.

CONCLUSION

Thus, using the transmission method in the integrating sphere, the optical parameters of the YAG:Ce phosphor were measured, as a result, the factors influencing the optical characteristics of white LEDs associated with the phosphor were revealed. Accurate measurements of the absorption of the incident blue light, together with the absolute values of reflected and transmitted light, are valuable optical constants of the tested phosphor samples. The quantum yield values obtained in this paper are in good agreement with the values reported by other authors in literature. It was concluded that the method of mixing the phosphor with silicone epoxy results in an increase in the intensity of the outgoing light, which is associated with the refractive parameters of the light in the layer.

- [1] R. Cees. Luminescence: From Theory to Applications, WILEY-VCH Verlag GmbH & Co. KGaA, Weinheim. (2008) 276 p.
- [2] H. Shi, C. Zhu, J. Huang, J. Chen, W. Wang, Y. Cao, X. Yuan. Luminescence properties of YAG:Ce, Gd phosphors synthesized under vacuum condition and their white LED

- performances, Optical Materials Express. Vol. 4, No. 4 (2014) pp. 649-655.
- [3] L. Arunachalam & Ranganathan, S. Kumar, V. Sivakumar, T. Preema M.T. Jose. Synthesis, photoluminescence and thermal quenching of YAG:Ce phosphor for white light emitting diodes,

- Indian Journal of Pure and Applied Physics. Vol. 49, No. 5 (2011) pp. 303-307.
- [4] *Lei, Chen & Chun-Che, Lin & Chiao-Wen, Yeh & Liu, Ru-Shi.* Light Converting Inorganic Phosphors for White Light-Emitting Diodes, Materials. Vol. 3, No. 3 (2010) pp. 2172–2195.
- [5] *A. Keppens, Y. Zong, Y. Ohno, G. Deconinck, P. Hanselaer,* Determining Phosphors' Effective Quantum Efficiency For Remote Phosphor Type Of Led Modules, CIE Expert Symposium on Spectral and Imaging Methods for Photometry and Radiometry (2010).
- [6] *S. Philippe, A.B. Parmentier, D. Poelman.* Journal of Electrochemical Society, Vol. 158, No. 6, (2011) pp. R37-R54.

Received: 10.09.2020

REFINEMENT OF THE CRYSTAL STRUCTURE OF MnBi_2Te_4 I.R. AMIRASLANOV, P.A. ASKEROVA, Z.S. ALIYEV, Y.R. ALIYEVA,
A.B. RAHIMLI*Institute of Physics, of Azerbaijan NAS**131, H. Javid ave., Baku, AZ 1143,**E-mail: iamiraslan@gmail.com*

Interest in magnetic topological insulators is growing every day. Among topological insulators, MnBi_2Te_4 is considered more promising. Due to its antiferromagnetic properties, it can be used in spintronic and quantum electronics. The authors of this work were the first to grow a single-phase ingot of MnBi_2Te_4 , refined the crystal structure, and examined the mutual solubility in the cationic sites of Mn and Bi. It is shown that such solubility is optional and depends on technological procedures. In addition to the seven-layer package characteristic of MnBi_2Te_4 , a new site was also found to be partially present.

Key words: Topological insulator, phase transition, structure.**PACS:** 548.4

1. INTRODUKTION

The integration of ferromagnetism in layered chalcogenide semiconductors with the properties of topological insulators (*TI*) and thermoelectric materials (*TE*) has attracted much attention in recent years. *TI* are insulators in bulk, but have metallic conductivity on the surface due to the presence of clearly defined topological surface states [1]. The charge carriers have spin polarization and are completely protected from defect scattering due to time reversal symmetry (*SOW*), which leads to almost non-dissipative currents. The aforementioned quantum effects occur in magnetic topological insulators (*MTI*), when a magnetic ion destroys and opens the energy gap in the surface state [2]. In the context of *TI*, the compounds MnBi_2Se_4 and MnBi_2Te_4 have recently been the cause of great research activity. The ferromagnetic seven-layer films of these compounds were grown by various authors either by molecular beam epitaxy alone or on the surface of a tetradymite-like *TI* [3], also by intercalation between five-layer *TI* packets [4-6], which are promising platforms for realizing quantized anomalous Hall effects [7,8], magnetoelectric effects [9-11] and the state of the axion insulator [12, 13]. MnBi_2Te_4 was described as the first antiferromagnetic *TI* [14,15], the observation of which can lead to such exotic phenomena as axion electrodynamics [16] and hinged Majorana modes [17]. Due to the growing *MTI* boom, detailed studies of ternary compounds in *MTM-A^V-Chalcogenide* systems (*MTM*=magnetic transition metal $3d3-6$; $A^V=\text{Sb, Bi}$; Chalcogenide= Se, Te) are of significant interest in the context of chemical and structural modeling of new *MTI* and *TE*. The great interest in these systems is due to the hope of obtaining a number of homologous compounds with controlled compositions and properties. It is known that several layered ternary phases are formed in the Mn-Bi-Te system [18]. The crystal structure of Bi_2Te_3 , solved in the middle of the last century, is also layered and is characterized by the structural type of tetradymite [19, 20]. The five-story packages (or slabs) of this structure are composed of five atomic layers: Te-Bi-Te-Bi-Te . The alternation of these packets along the *c* axis form Bi_2Te_3 (-5-5-5-) crystals. The addition of Mn atoms to

the composition promotes the formation of seven-story layers of the type $\text{Te-Bi-Te-Mn-Te-Bi-Te}$. Accordingly, the crystal structure of MnBi_2Te_4 is formed by alternating similar layers along to the *c* axis (-7-7-7-). The crystal structure of MnBi_2Te_4 was solved by Korean scientists based on X-ray powder data [21]. However, obtaining high-quality crystals of this compound in monophasic form is not an easy task. Usually the x-ray analysis of the ingots obtained by melting the elements taken in the ratios corresponding to MnBi_2Te_4 showed that the final product consists of a mixture of several phases. Studies have shown that these phases correspond to compounds of the mixed layer type, which are formed from five and seven layer slabs in different ratios. Therefore, it was necessary to study the phase formation in the Mn-Bi-Te system. For this purpose, in our previous work [18], we carried out syntheses in various stoichiometric ratios in the range $\text{Bi}_2\text{Te}_3\text{-MnBi}_2\text{Te}_4$ and refined the crystal structures of the homologous phases MnBi_2Te_4 , MnBi_4Te_7 and $\text{MnBi}_6\text{Te}_{10}$ by the Rietveld method. In all cases, the morphological characteristics of the obtained crystals indicate their belonging to the layered structures of the Van der Waals type. Numerous articles published in recent years on Mn-containing *TIs* show that not many still manage to isolate single-phase pieces of at least a few millimeters in size [22, 23]. Also, the quality of crystals grown by the Bridgman method did not correspond to obtaining high quality single-crystal diffraction data. As noted above, the magnetic properties of MnBi_2Te_4 are currently widely studied both experimentally and theoretically. Correlation between these results requires more accurate structural data. One of these parameters is the interchange of metal atoms Mn and Bi, which is necessary for an accurate assessment of magnetic properties, for example, phase transitions of the paramagnetic-antiferromagnetic type. However, in the aforementioned work [21], the degree of mutual solubility in cationic positions was not determined, but it was considered that they were occupied by one type of atoms. In fact, for various reasons, they can partially deal with other atoms involved in synthesis. Such reasons may be the proximity of atomic or ionic radii, the presence of free positions in the structure, better

satisfaction of local valence balances (*LVB*), etc. There are similar reasons in the structure of the tetradymite type. For example, in the Bi_2Te_3 structure, Bi atoms are noticeably shifted from the center of the octahedrons.

Apparently, the main reason for this shifting is an improvement in *LVB* values. In the idealized structure of Bi_2Te_3 , the *LBV* value for tellurium atoms in the central layer is 3 electrons, and for the outer layers of blocks, 1.5e. The shifting of Bi atoms towards Te atoms in the outer layers reduces this large difference in real structures. In seven-layer packets, the presence of more divalent Mn^{+2} atoms provide additional opportunities for improving TWT. In this case, the substitution of some of the Bi⁺³ atoms by the Mn^{+2} atoms lead to a similar result.

In recently published papers [18, 24], this issue was discussed. The authors show that such a cationic substitution does exist. They experimentally established that the central cationic layer of the seven-story package of MnBi_2Te_4 is populated with 85% Mn + 15% Bi atoms, and in the other cationic layer 10% of Bi atoms are replaced by Mn atoms. Nevertheless, it is still impossible to say that the noted values of mutual solubility are optimal for 7-storey blocks, or does it depend on the technological conditions of synthesis? Therefore, it is impossible to consider the issue of solubility in cationic positions solved, and obtaining new data on the basis of various samples is necessary.

2. THE EXPERIMENTAL PART

2.1. Material preparation

First, the binary compounds MnTe and Bi_2Te_3 were synthesized from bismuth, manganese, and tellurium elements (all 99.999 wt%) purchased from Alfa Aesar. The synthesis was carried out in sealed quartz ampoules by melting elements taken in stoichiometric ratios at 1180 and 630°C, respectively. Avoid to the reaction of manganese with silicon dioxide during melting, the inner wall of the ampoule was previously coated with graphite by thermal decomposition of acetone in a medium with a low oxygen content. And MnBi_2Te_4 was synthesized from previously prepared MnTe and Bi_2Te_3 by direct melting at 980°C for 8 hours. After that, polycrystalline alloy samples were pulverized, pressed into tablets, and annealed at 575°C for 750 hours. As a result, a single-phase polycrystalline MnBi_2Te_4 was obtained.

2.2. Refinement of the crystal structure of MnBi_2Te_4

The crystal structure was refined by the Rietveld method based on X-ray powder diffraction data obtained on a “D2 Phaser” diffractometer, and all calculations were performed using the Topas 4.2 software (Bruker, Germany). The results obtained are shown in tables 1-3 and in fig. 1-3.

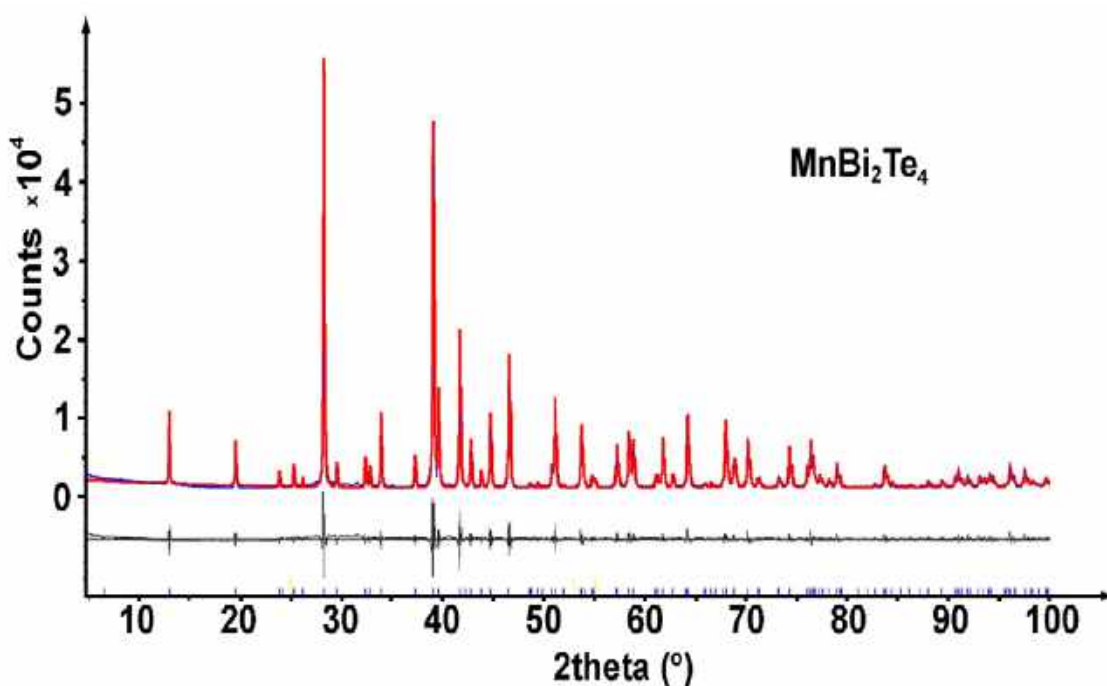


Fig. 1. Experimental, calculated by Rietveld (almost identical upper profiles of blue and red) and difference diffraction profiles (below) of MnBi_2Te_4 crystals.

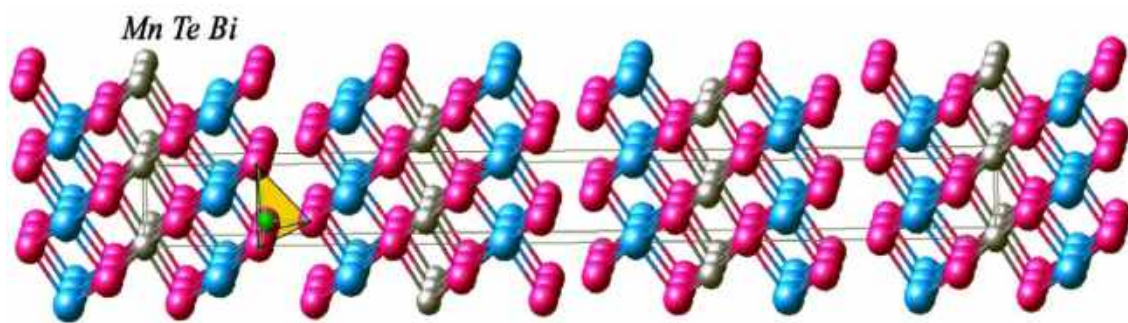


Fig. 2. Crystal structures of MnBi_2Te_4 : projection of the structure onto the (100) plane. Interlayer tetrahedral position highlighted in yellow

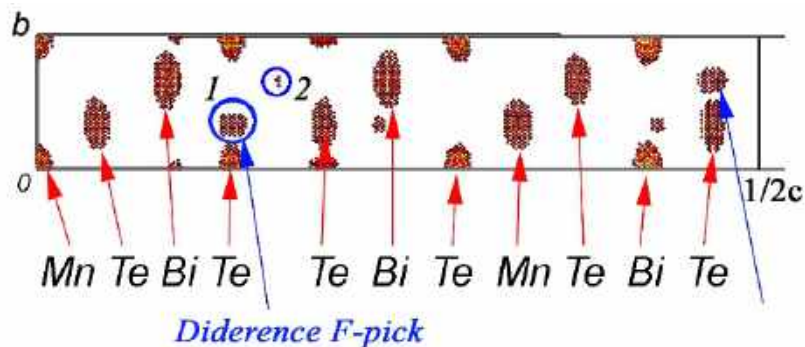


Fig 3. The position of difference fourier picks in F-map

Table 1.
Crystallographic data of the crystal structure of MnBi_2Te_4

Characteristic	Value
M (g/mol)	983.298
Z	3
Syngonia	Trigonal
Prost. Group (No.)	R-3m (166)
Radiation	Cu-K α_1 ($\lambda = 1.540596 \text{ \AA}$)
2 θ interval ($^\circ$)	$5 \leq 2\theta \leq 100$
R-Bragg (%)	1.542
Cell Parameters:	
a (\AA)	4.3304(1)
c (\AA)	40.956(2)
Cell Volume (\AA^3)	664.87(2)
X-ray density (g / cm 3)	7.32(5)

Table 2.
Refined coordinates of atomic positions and inter-atomic distances of MnBi_2Te_4 crystals.

Site	Np	X	Y	Z	Atom	Occ	Beq
Mn	3	0	0	0	Mn $^{+2}$	1.02(3)	0.5
Bi	6	0	0	0.4230(2)	Bi $^{+3}$	0.98(2)	0.5
Te (1)	6	0	0	0.1344(2)	Te	1	0.5
Te (2)	6	0	0	0.2924(3)	Te	1	0.5
Interatomic distances:					(\AA)		
Mn – Te (2)					3.010(8)		
Bi – Te (1)					3.101(9)		
Bi – Te (2)					3.199(10)		

Table 3.

Refined coordinates of atomic positions and inter-atomic distances of MnBi_2Te_4 crystals, taking into account the occupation of the inter-slab's tetrahedral positions.

Site	Np	X	Y	Z	Atom	Occ	B _{eq}
Mn	3	0	0	0	Mn ⁺²	0.878(46)	1
Bi	6	0	0	0.4228(3)	Bi ⁺³	0.942(32)	1
Te(1)	6	0	0	0.1348(3)	Te	1	1
Te(2)	6	0	0	0.2923(4)	Te	1	1
Mn*	6	0	0	0.804(10)	Mn ⁺³	0.058(32)	1
Bi*	3	0	0	0	Bi ⁺³	0.122(46)	1
Interatomic distances:					(Å)		
Mn – Te(2)					3.012(8) x 6		
Bi – Te(1)					3.115(9) x 3		
– Te(2)					3.192(12) x 3		
Mn* – Te(1)					2.490		
– Te(2)					2.502 x 3		

The obtained diffraction pattern is uniquely indexed with the parameters of the rhombohedral cell of MnBi_2Te_4 . On the other hand, the presence or absence of other homologous compounds (MnBi_4Te_7 , $\text{MnBi}_6\text{Te}_{10}$, ...) in the sample is very easily determined by the $00l$ type reflections using powder diffraction pattern. The fact is that a small value of the parameters a and b , as well as a multiply large value of c , always leads to the appearance of non-superimposed and sufficiently strong peaks of the $00l$ type in the initial region of the diffraction pattern (Cu , $k\alpha$; $5^\circ \leq 2\theta \leq 100^\circ$), which make it possible to unambiguously determine the phase sample composition. In the noted system, in addition to ternary homologous phases, binary compounds MnTe and MnTe_2 can also form. However, a detailed examination of the diffraction image did not confirm the presence of these phases. Thus, the sample under study consists exclusively of MnBi_2Te_4 crystals and the results of structure refinement presented in table 2. It can be seen from this table that, within the error, no substitution at cation positions ($\text{Mn} \leftrightarrow \text{Bi}$) is observed.

3. RESULTS AND DISCUSSIONS

The atomic coordinates given in table 2 were used to calculate the difference Fourier synthesis. On the

obtained Fourier map two peaks with a certain electron density were clearly seen. Both peaks are located in the inter-layer van der Waals space. The intensity of the first peak is several times stronger than the background level, while the second one is noticeably weak and should be ignored. In fig.3, these positions are indicated by numbers 1 and 2. Interestingly, peak-1 is tetrahedral surrounded by tellurium atoms. Previously, such a partial filling of the van der Waals space between blocks was established in a tetradymite-like structure $\gamma\text{-In}_2\text{S}_3$, stabilized by the addition of As or Sb [25]. Consequently, the formation of such tetrahedrons in the MnBi_2Te_4 structure looks quite possible. Therefore, we are inclined to believe that, in fact, a previously unobserved new cation position is formed in MnBi_2Te_4 crystals. The refinement of the structure with the addition of Mn atoms to this position corresponded to their approximately six percent occupation. These results are shown in table 3.

Apparently, the occupancy factors of cationic positions depend on the technological process and, to a certain extent, can be used to control the properties of these materials. Thus, new syntheses and further research on this issue are still needed.

- [1] M. Z. Hasan, C.L. Kane. Rev. Mod. Phys. 2010, v. 82, p. 3045.
- [2] R. Yu, W. Zhang, H. J. Zhang, S.C. Zhang, X. Dai, Z. Fang. Science. 2010, v. 329, p.61.
- [3] T. Hirahara, S. V. Eremin, T. Shirasawa etc. Nano Lett. 2017, v. 17, p. 3493.
- [4] J.A. Hagmann, X. Li, S. Chowdhury, S.N. Dong, S. Rouvimov, S.J. Pookpanratana, K.M. Yu, T.A. Orlova, T.B. Bolin, C.U. Segre et al. New J. Phys. 2017, v. 19, p. 085002.
- [5] E.D. Rienks, et al. Large magnetic gap at the Dirac point in a Mn-induced Bi_2Te_3 heterostructure, arxiv1810.06238
- [6] Y.S. Hou, R.Q. Wu. Axion insulator state in a ferromagnet topological insulator antiferromagnet heterostructure, archive: 1809.09265
- [7] R. Yu, W. Zhang, H.J. Zhang, S.C. Zhang, X. Dai, Z. Fang. Science. 2010, v. 329, p. 61.
- [8] C.Z. Chang, J. Zhang, X. Feng, J. Shen, Z. Zhang, M. Guo, K. Li, Y. Ou, P. Wei et al. Science. 2013, v. 340, p. 167.
- [9] X.L. Qi, T.L. Hughes, S.C. Zhang. Phys. Rev. B. 2008, v. 78, p.195424.
- [10] A.M. Essin, J.E. Moore, D. Vanderbilt. Phys. Rev. Lett. 2009, v.102, p.146805.
- [11] W.K. Tse, A.H. MacDonald. Phys. Rev. Lett. 2010, v.105, p. 057401.
- [12] M. Mogi, M. Kawamura, A. Tsukazaki, R. Yoshimi, K.S. Takahashi, M. Kawasaki, Y. Tokura. Sci. Adv. 2017, v. 3, p. 1669.

- [13] *M.H. Chan, N. Samarth, C.Z. Chang.* Phys. Rev. Lett. 2018, v.120, p. 056801.
- [14] *Y. Gong.* Experimental realization of an intrinsic magnetic topological insulator, arxiv:1809.07926.
- [15] *M.M. Otrokov, I.P. Rusinov, M. Blanco-Rey, M. Hoffmann, A. Yu. Vyazovskaya, S.V. Ereemeev, A. Ernst, P.M. Echenique, A. Arnau, E.V. Chulkov.* Unique thickness-dependent properties of the van der Waals interlayer antiferromagnet MnBi_2Te_4 films, archive:1810.05289.
- [16] *R. Li, J. Wang, X.L. Qi, S.C. Zhang.* Nat. Phys. 2010, v. 6, p. 284.
- [17] *Y. Peng, Y. Xu.* Proximity-induced Majorana hinge modes in antiferromagnetic topological insulators, archive:1809.09112].
- [18] *Z.S. Aliev, I.R. Amiraslanov, D.I. Nasonova, A.V. Shevelkov, N.A. Abdullayev, Z.A. Jahangirli, E.N. Orujlu, M.M. Otrokov, N.T. Mamedov, M.B. Babanli, E.V. Chulkov.* Journal of Alloys and Compounds 2019, v.789, p. 443.
- [19] *Y.S. Hor, P. Roushan, H. Beidenkopf, J. Seo, D. Qu, J.G. Checkelsky, L.A. Wray, D. Hsieh, Y. Xia, S.Y. Xu, D. Qian, M.Z. Hasan, N.P. Ong, A. Yazdani, R. J. Cava.* Phys. Rev. B. 2010, v.81, p. 195203.
- [20] *D. Harker.* Zeitschrift für Crystallography - Crystalline Materials. 1934. v. 89. № 1-6. p.175.
- [21] *D.S. Lee, T.H. Kim, C.H. Park, C.Y. Chung, S. Lim, W.S. Seo, H.H. Park* CrystEngComm. 2013, v. 15, № 7, p. 5532.
- [22] *A. Zeugner et al.* Chem. Mater. 2019. v. 318, p.2795.
- [23] *R.C. Vidal et al.* archive:1906.08394 v.1.
- [24] *A. Zeugner, F. Nietschke, U. Anja, B. Wolter, etc.* Chemical Aspects of the Candidate Antiferromagnetic Topological Insulator MnBi_2Te_4 . Chem. Mater. 2019, v. 318, p. 2795.
- [25] *R. Diehl, C.D. Carpentier, R. Nitsche.* The crystal structure of gamma-In₂S₃ stabilized by As or Sb. Acta Crystallographic (24, 1968-38, 1982), 1976, 32, p.1257-1260.

Received: 21.09.2020

INFLUENCE OF SURFACE DISTURBANCES OF $\text{Bi}_{0.5}\text{Sb}_{1.5}\text{Te}_3$ CRYSTAL ON THE TRANSPORT OF ELECTRONS IN ITS VOLUME, SURFACE AND IN THE INTERFACE WITH Bi-Sn ALLOY

N.M. AKHUNDOVA¹, T.D. ALIYEVA², G.J. ABDINOVA³

¹Azerbaijan State University of Economics (UNEC)

AZ-1001, Azerbaijan Republic, Baku, Istiglaliyyat street, 6

²Institute of Physics NAS of Azerbaijan

AZ-1143, Azerbaijan Republic, Baku, H. Cavid avenue, 131

e-mail: tunzalaaliyeva@mail.ru

³Azerbaijan State Pedagogic College

AZ-1143, Azerbaijan Republic, Baku, İnshaacılar avenue, 14

Polarization investigations have shown that the influence of inhibitors containing inorganic oxidants and monoethanolamide reduce the corrosion rate of steel, which clearly testify about the slowdown of the cathodic process, the restoration of molecular oxygen and the anodic metal ionization reaction. Confirmation of this is the fact, that the developed mixtures are functioning as inhibitors of mixed type.

Keywords: polarization, inhibitor, cathodic and anodic processes, ionization, synergetic effect.

PACS: 61.50.-f, 61.82.Fk, 68.47.Fg, 72.20.-i

1. INTRODUCTION

In the manufacture of samples from ingots of crystals of $\text{Bi}_{0.5}\text{Sb}_{1.5}\text{Te}_3$ solid solution, widely used in various thermocouples, by the methods of mechanical or electroerosive cutting on their cut surface a disturbed layer appears, which differs from the crystal in composition and structure [1]. Such disturbed layers will differ in electrical properties from the sample. Therefore, the electrical parameters of the samples, their interfaces with metal alloys and electronic converters based on them will be determined by the parameters of the surface layer. In order to identify the regularities and mechanism of the effect of the disturbed surface layer on the electrical properties of samples of $\text{Bi}_{0.5}\text{Sb}_{1.5}\text{Te}_3$ solid solution and the interfaces between them, we studied the effect of surface treatment of samples cut from $\text{Bi}_{0.5}\text{Sb}_{1.5}\text{Te}_3$ crystal ingots on their surface conductivity, bulk electrical conductivity σ , thermo-e.m.f. α and Hall R_H coefficients, as well as on the electrical and adhesive properties of the contacts of structures (Bi-Sn) - $\text{Bi}_{0.5}\text{Sb}_{1.5}\text{Te}_3$ in the temperature range of 77-300 K.

2. EXPERIMENTAL METHODS

The compositions were synthesized by direct fusion of the initial components of the Bi-000 brand bismuth, the Sb-000 brand antimony, the T-hP grade tellurium (99,999) (additionally purified from impurities by the zone melting method). Crystal ingots were grown from the synthesized composition by directional crystallization.

Samples for research in the form of rectangular parallelepipeds with dimensions of $12 \times 6 \times 3 \text{ mm}^3$ were cut out of crystalline ingots on an electroerosive cutting installation. The measurements of these parameters were carried out on samples immediately after they were cut from ingots and on the same samples after processing their side and end surfaces by electrochemical etching in a special installation in a solution of $\text{KOH} + \text{C}_4\text{H}_4\text{O}_6 + \text{H}_2\text{O}$ (taken in a certain ratio) at $\sim 25\text{-}30^\circ\text{C}$ for 40 seconds. The interfaces (mutual diffusion of components, thickness and composition of the

formed intermediate phases) of the solid solution crystals with the indicated contact alloys were studied by local X-ray spectral microanalysis using a Cameca-Ms-46 microanalyzer. Metam-RIM microscope was also used with a magnification of 500 times. The depth of the disturbed layer on the cut surface of the crystal samples was estimated from the dependence of the etching rate on time, and the nature of the structure of the damaged layer was studied by X-ray diffraction. The adhesive strength was determined by the avulsion method [2], the adhesion work of A_a calculated from the measured surface tension σ_s (according to the method [3]) and the limiting wetting angle (according to the "lying drop" method [4]) according to the formula $A_a = \sigma_s (1 + \cos \theta)$.

The electrical parameters of the crystals and contacts of the samples were measured by the probe method [5], and the surface conductivity σ_s was measured by the wedge method [6].

The current-voltage characteristics of the structures indicated that contacts were ohmic in all cases.

3. EXPERIMENTAL RESULTS AND DISCUSSIONS

The data obtained are presented in figures 1-3 and in the table.

It can be seen that the temperature dependence of the surface conductivity σ_s of untreated samples of $\text{Bi}_{0.5}\text{Sb}_{1.5}\text{Te}_3$ crystals is quite complex and very different from those for the processed samples (Fig. 1). After surface treatment by electrochemical etching σ_s decreases several times over the entire temperature range and becomes almost independent of temperature. These data suggest that the specific temperature dependence of σ_s in untreated samples is due to the surface layer that occurs when cutting samples from ingots. It should be noted that the temperature dependence σ_s of the samples in all cases is reversible, i.e. the observed features of σ_s are due to electronic processes in the surface layer of the cut of the $\text{Bi}_{0.5}\text{Sb}_{1.5}\text{Te}_3$ sample.

Table

Dependence of surface tension σ_s (mJ/mm²), limiting contact angle θ (deg), adhesion work A_a (mJ/m²), contact resistance r_k ($10^{-5} \Omega \cdot \text{cm}^2$) of an alloy mass.%: 57 Bi + 43 Sn with a crystal ($\text{Bi}_{0.5}\text{Sb}_{1.5}\text{Te}_3$) as a result of changes in surface conductivity σ/σ_0 , bulk conductivity σ/σ_0 , Hall R_H / R_{H0} and thermo-e.m.f. coefficients α/α_0 during electrochemical processing of the crystal surface.

T, K	σ_s	θ	A_a	r_k , 300K	σ/σ_0		σ/σ_0		R_H/R_{H0}		α/α_0	
					77K	300K	77K	300K	77K	300K	77K	300K
413	409	60	463									
433	409	12	809									
453	413	11	816	0,70	7,10	0,80	1,12	1,33	1,01	1,06	0,94	0,95
473	413	11	817									
493	414	11	820									
513	415	11	823									

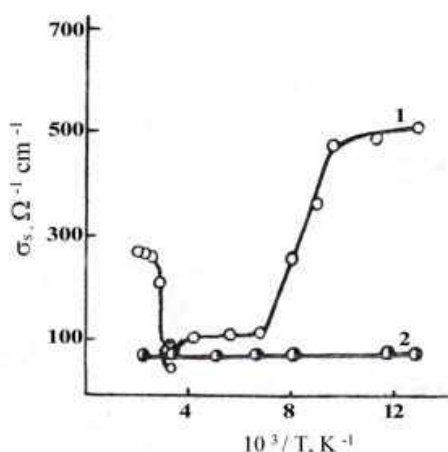


Fig. 1. Temperature dependence of the surface conductivity of $\text{Bi}_{0.5}\text{Sb}_{1.5}\text{Te}_3$ samples before (1) and after (2) treatment.

It follows from Fig. 2 that the surface treatment of the samples does not change the character of the temperature dependences of σ , α , R_H for $\text{Bi}_{0.5}\text{Sb}_{1.5}\text{Te}_3$ crystals. However, the numerical values of these parameters after processing undergo certain changes. Due to the fact that the disturbed surface of the crystal has a higher surface conductivity than

σ_s than the treated surface, it can lead to shunting (shorting) of the ends of the sample, i.e. an increase in σ measured before treatment and a decrease in α and R_H .

The structure and depth of the disturbed layer arising on the surface of the $\text{Bi}_{0.5}\text{Sb}_{1.5}\text{Te}_3$ sample in the process of electroerosion cutting are investigated. The depth of the disturbed layer was estimated from the time dependence of the rate of electrochemical etching in a $\text{KOH} + \text{C}_4\text{H}_4\text{O}_6 + \text{H}_2\text{O}$ solution. The nature of the structure of the disturbed layer was studied by X-ray diffraction when shooting a fixed sample for reflection to the RKSO camera, in the radiation of a tube with a copper anticathode; the depth of the semi-absorbing layer is $\sim 15 \mu\text{m}$.

The experiments showed that during electroerosive cutting of crystals of the $\text{Bi}_{0.5}\text{Sb}_{1.5}\text{Te}_3$ solid solution into samples a disturbed layer $\sim 40 \mu\text{m}$ thick appears on the surface of the cut. This disturbed layer consists mainly of two sublayers with different compositions: a sublayer formed by melting and partial combustion of a semiconductor material during cutting and quenching of the liquid phase, which is heavily contaminated with the products of the electrode and the dielectric medium, and the sublayer which is formed due to deformation of the surface of the sample at cutting, leading to fragmentation of crystallites, bending of atomic planes and the formation of polycrystalline areas on the surface of the single crystal.

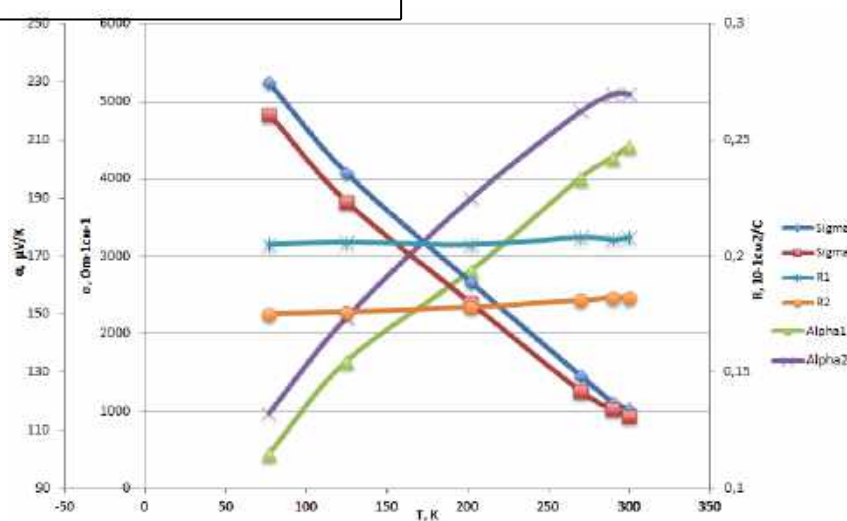


Fig. 2. Temperature dependence of the electrical conductivity σ , thermo-e.m.f. α and Hall R_H coefficients of $\text{Bi}_{0.5}\text{Sb}_{1.5}\text{Te}_3$ samples before (1; 2; 3) and after (10; 20; 30) treatment of their surface.

The table presents data on the dependences of the surface tension coefficient σ_s , limiting contact angle θ , adhesion work A_a , and contact resistance r_k at the contact alloy-Bi_{0.5}Sb_{1.5}Te₃ interface on preliminary processing of the crystal surface and temperature.

It can be seen that the contact angle θ decreases rapidly with increasing temperature and at temperatures 20–40 degrees higher than the melting temperature of the contact material is almost independent of temperature. With increasing temperature the work of adhesion also increases.

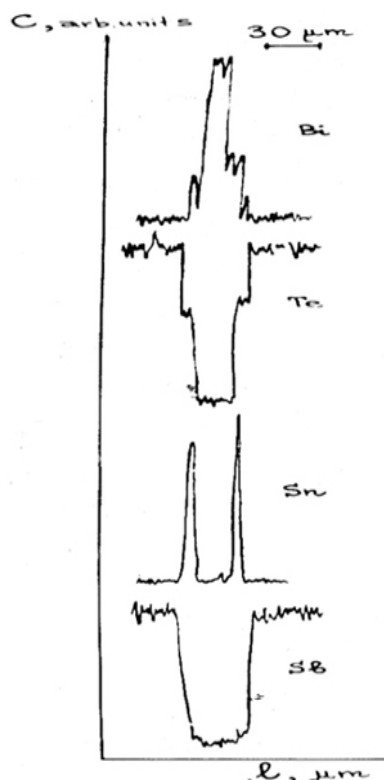


Fig. 3. Distribution curves of Bi_{0.5}Sb_{1.5}Te₃ crystal components and the contact material in the crystal-contact material-crystal structure.

The measured adhesive strength of Bi_{0.5}Sb_{1.5}Te₃ contacts with the alloy at ~ 300 K was ~ 73 kg/cm².

When creating contacts to Bi_{0.5}Sb_{1.5}Te₃ crystal by the tinning method, contact alloy simultaneously dissolves the crystal in the contact material melt, diffusion the ingredients of the contact material melt into the near-contact region of the crystal, and reactions leading to the formation of new intermediate phases at the interface.

Figure 3 shows a characteristic diagram illustrating changes in the distribution of the constituent elements of the crystal matrix (Bi_{0.5}Sb_{1.5}Te₃) - Bi-Sb-Te and contact material (Bi-Sn) at the interface Bi_{0.5}Sb_{1.5}Te₃ - contact material - Bi_{0.5}Sb_{1.5}Te₃.

It is seen that the concentration of the elements that make up the crystal and the contact alloy at the interface changes quite sharply. At the interface SnTe interlayers of 5–7 μm thick are formed. In this case the tin atoms that make up the contact material are mainly localized in the end parts of the initial contact layer, i.e. at the crystal-contact material interface, and the bismuth atoms are localized closer to the central part of the contact layer.

Microscopic studies have shown that at the crystal-contact material junction boundary a band is observed that clearly stands out in color against the background of the bulk of the contact material. The intermediate phases formed have different electrical and adhesive parameters which determine the electrical and adhesive properties of the interface of Bi_{0.5}Sb_{1.5}Te₃ crystals with the considered contact alloy.

4. CONCLUSION

It was found that during electroerosive cutting of single crystals of Bi_{0.5}Sb_{1.5}Te₃ solid solution single crystals into samples, a layer with disturbed composition and structure up to 40 μm thick appears on the surface of the cut. Disturbance of the surface substantially changes the electrical properties of the surface, volume, and interface between the crystal and the contact alloy. When the contact alloy crystals are applied to the ends of the samples, mutual diffusion and chemical interaction of the ingredients of the contact material and the crystal occurs, as a result of which an intermediate phase of the SnTe type is formed, which affects the electrical and adhesive properties of the interface. A correlation is observed between the parameters r_k and θ , A_a of the contacts.

- [1] M.G. Dick, L.N. Rybina, A.A. Dubrovina, D.Sh. Abdinov Structure and adhesive properties of the surface of samples of solid solutions based on bismuth tellurides after cutting. Izv. USSR Academy of Sciences, Neogan.materials, 1988 24 (4) p. 688-690 (in Russian).
- [2] T.I. Aliyeva, Ya.S. Feyiziev, Z.F. Agaev, D.Sh. Abdinov. Method for determining the temperature dependence of the adhesive strength of thermoelectric materials with commutation alloys. Zavodskaya laboratoriya, 1992. V. 52. P. 46-47 (in Russian).
- [3] T.D. Aliyeva, G.J. Abdinova, N.M. Akhundova, D.Sh. Abdinov. Physical Chemistry Journal, 2008, 82, pp.2185-2186 (in Russian).
- [4] A.I. Belyaev, Ye.A. Zhemchuzhina. Surface phenomena in metallurgical processes. M.: Metallurgizdat, 1952.143 p. (in Russian).
- [5] T.D. Aliyeva, G.D. Abdinova, N.M.A khundova, S.Z. Dzhaforova. Current flow mechanism in contact (In-Ag-Au) -Pb_{1-x}Mn_xTe Transactions of National Academy of Science of Azerbaijan, series of physics-mathematical and technical sciences, Physics and Astronomy, 2011. XXX. 2, p.126-130 (in Russian).
- [6] N.R. Rubinstein, V.I. Fistul. Dokl. USSR Academy of Sciences, 1959. 125. p.542-545 (in Russian).

MAGNETIC INTERACTION OF "EXCESS" CATIONS Cu^{+2} AND Fe^{+2} IN THE 2D-PLANE IN A SINGLE CRYSTAL $\text{Cu}_{1.04}\text{Fe}_{1.12}\text{Te}_{1.84}$

A.I. JABBAROV

*Institute of Physics of NAS,
131, H. Javid ave. Baku, AZ 1143
E-mail: ayd.jabb @ list.ru*

This paper presents the results of measurements of the temperature dependence of the magnetic susceptibility and magnetization (in a magnetic field up to $H=50\text{kOe}$) of single crystals of the non-stoichiometric chalcopyrite type $\text{Cu}_{1.04}\text{Fe}_{1.12}\text{Te}_{1.84}$ ($\sim\text{Cu}_{1.13}\text{Fe}_{1.22}\text{Te}_2$) in the temperature range $2 \leq T \leq 400\text{K}$. The measurement results indicate the presence of "clusters" ($\text{Cu} - \text{Te} - \text{Fe} = \text{Te}$) of an antiferromagnetic nature of the interaction, as well as "excess" of Cu^{+2} and Fe^{+2} cations in the 2D plane behaving like nanoparticles. The effective magnetic moment of iron atoms $M_{\text{eff}} > 1.3\mu_B$ at $H \leq 1000\text{Oe}$ and at $1.0 \leq H \leq 50\text{kOe}$ $M_{\text{eff}} > 2.0\mu_B$.

In the isotherms of magnetization (hysteresis) $M(H)$ at temperatures of 2, 4, 100 and 300K, residual magnetizations are observed, which are associated with frustration of magnetic interactions during the formation of a disordered magnetic structure of iron and copper. Antiferromagnetically located "clusters" at $T_N=65\text{K}$ transform into a paramagnetic state, which coincides with the spin-glass state at $T_g=65\text{K}$ (T_g is the freezing temperature). These results are in good agreement with the Mossbauer spectra of CuFeTe_2 .

Keywords: magnetic susceptibility, frustration, spin-glass state, magnetization isotherm.

PACS: 75.30.-m, 76.80.+y, 76.60Jx, 75.50.-y

1. INTRODUCTION

The strong temperature dependence of the isomeric shift of excess iron [1, 2], which appears as an intermediate hyperfine field, is an indicator that the electron density between Fe-Te (*CFT*, Fe_{1+x}Te) layers evolves significantly with increasing temperature of the two-dimensional nature of the material at low temperatures.

The embedded iron has a relatively large localized magnetic moment, at least for the region with the highest hyperfine field. These moments are almost randomly distributed over the interstitial sites of the sub lattice. Therefore, they strongly interact with electrons capable of forming Cooper pairs and preventing the onset of superconductivity. To obtain a superconducting material, it is necessary to remove this iron from the interstitial regions [1, 2].

Like the *HTSC* families of cuprites and ferropnictides, the terminal compound *CFT* and Fe_{1+y}Te is magnetically ordered and undergoes structural distortion, which lowers the high-temperature tetragonal symmetry of the lattice. The physics of these low-temperature phases and their relationship with superconductivity is of great interest and has been the subject of intense research [1, 2-7]. Two general trends in phase diagrams were established:

(1) if there is no first-order magneto structural transition, then the lattice distortion usually occurs at higher temperatures (T_S -structural transition) than magnetic ordering (T_N), T_S , or T_N and

(2) both T_S and T_N decrease with chemical substitution, so that both kinds tend to disappear as the superconducting state develops.

While this observation suggests an inextricable relationship between magnetic ordering, lattice distortion and superconductivity [1, 2]. Further studies of Fe-containing chalcogenide compounds are of interest. In this work, we present the results of magnetic

studies carried out to determine the magnetic state of a compound of nonstoichiometric chalcopyrite of the $\text{Cu}_{1.04}\text{Fe}_{1.12}\text{Te}_{1.84}$ (*CFT*) type and "excess" of Cu^{+2} and Fe^{+2} cations in the 2D plane.

Note that a lot of works [2-14, 16, 18] are devoted to growing single crystals, studying the crystal structure, and measuring magnetic, electrical and other physical characteristics of nonstoichiometric chalcopyrite type CuFeTe_2 .

The above compounds are characterized by the presence of different positions of magnetic ions, which introduces disorder into their magnetic subsystem and, as a consequence, leads to frustration of magnetic interactions during the formation of a disordered magnetic structure. And the excess of Cu^{+2} and Fe^{+2} atoms are located in the $2c$ 'position with coordinates (0, 0, 0.715) and (0, 0.5, 0.715), respectively [4]. The valence of cations at this position significantly affects the type of phase transitions (magnetic, spin-glass, and structural).

Polycrystals $\text{Cu}_{1.04}\text{Fe}_{1.12}\text{Te}_{1.84}$ were synthesized by alloying initial high-purity elements (Cu, Fe, Te) in quartz ampoules evacuated to 10^{-3}Pa , and their single crystals were grown by the Bridgman-Stockbarger method [4, 5, 14, 16]. The studied *CFT* single crystals crystallize in a tetragonal system with cell periods: $a=3.97$; $c=6.11\text{\AA}$, $v=96.2991\text{\AA}^3$, $\rho_{\text{prent}}=6.63\text{g/cm}^3$, etc. $P4/nmm$, $z=1$, which is in full agreement with the data [7].

2. EXPERIMENT

We have studied the crystal structure and magnetic properties of $\text{Cu}_{1.04}\text{Fe}_{1.12}\text{Te}_{1.84}$ (*CFT*) single crystals grown by the modified Bridgman method. Single crystals grown from a melt are structural with Rikkardit - $\text{Cu}_{4-x}\text{Te}_2$ [15], with the only difference that in the sub tetragonal structure $\text{Cu}_{1.04}\text{Fe}_{1.12}\text{Te}_{1.84}$ (*CFT*) both Cu and Fe metal atoms are

statically distributed in double crystallographic positions. Copper atoms are coordinated with $4\text{Fe}+4\text{Te}$, forming a tetragonal prism. $4\text{Cu}+\text{Fe}+\text{Te}$ form a polyhedron in the form of empty octahedral (fig. 1).

Taking into account that the minerals Cuprotybit - $\text{Cu}_2(\text{Sb}, \text{Te})$ and Rikkardit - Cu_{2-x}Te [15] have similar unit cell parameters and such symmetries, it can be assumed that the crystallization of CuFeTe_2 changes the valence of metals due to the lack of a part tellurium atoms (Te) and a composition with an excess of metal atoms is formed. This compound is converted to a tetragonal structure by CFT compounds. It was found that the Cu and Fe ions occupy a double position $2a$: $(0, 0, 0)$, and two Te atoms are located in the $2c$ position with coordinates $(0, 0.5, 0.28)$. And the excess of Cu and Fe atoms are located in the $2c$ position with coordinates $(0, 0, 0.715)$ and $(0, 0.5, 0.715)$, respectively [2, 6]. It was shown in [4, 18] that copper atoms are surrounded by eight $(4\text{Te}+4\text{Fe})$ atoms in the form of a tetragonal prism. Each such prismatic layer is located at a distance of $\sim 3.0\text{\AA}$ from the next analogous layers, which gives the structure a layered character and perfect cleavage. In other words, prismatic copper layers alternate parallel to the (001) plane of the crystal with empty prismatic layers. The chemical bond is found according to the scheme $\text{Cu}^+-\text{Te}^{2-}-\text{Fe}^{3+}=\text{Te}^{2-}$ as a "cluster", and the excess of 15% of Cu and Fe ions are randomly located in the voids of the lattice (Fig.1). It is known that a magnetic cluster exhibits fractal properties with increasing temperature. The presence of nonmagnetic tellurium atoms in the system leads to loosening of the structure of the magnetic cluster (see fig.1).

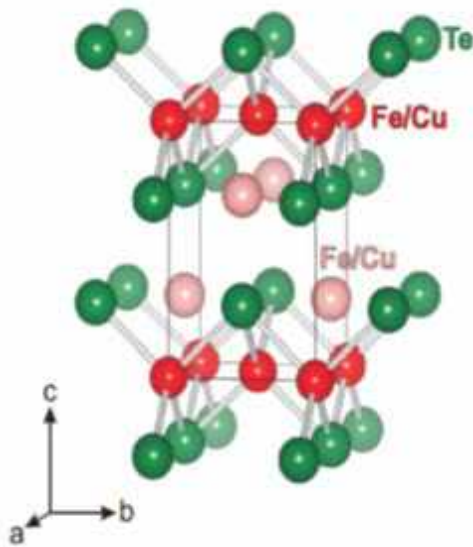


Fig. 1. Crystal structure CuFeTe_2

3. MAGNETIC SENSITIVITY. METHODS FOR MEASURING MAGNETIC PROPERTIES

The magnetic properties of the samples were studied using an MPMS-XL-5 SQUID magnetometer

(MPMS-Magnetic Property Measurement System) from Quantum Design, the absolute sensitivity of which is $\pm 1 \cdot 10^{-11} \text{ G} \cdot \text{cm}^3$ at $0 \text{ Ge} \leq H \leq 10 \text{ kOe}$ and $\pm 5 \cdot 10^{-11} \text{ G} \cdot \text{cm}^3$ at $10 \text{ kOe} < H \leq 50 \text{ kOe}$.

When studying magnets in a metastable state, methods of measuring the susceptibility are usually used when cooling without an external magnetic field (ZFC-zero field cooling) and during cooling in an external magnetic field (FC - field cooling) [16].

The magnetic susceptibility was measured in the temperature range $2-400\text{K}$ and the range of magnetic fields H up to 50 kOe . To study the temperature dependence of the magnetic susceptibility, the samples were cooled in zero magnetic field (ZFC) to 2K . Then a magnetic field (FC) with a strength of 1000 Oe was turned on; this magnetic field was kept constant. Magnetic susceptibility was measured during temperature rise (ZFC). At the next stage, the samples were cooled again, but already at the value of the magnetic field set at the previous stage, while taking readings (FC). These measurements were repeated at magnetic field strengths of 10 and 20 kOe . The field dependences of magnetization (hysteresis) were measured at temperatures of $2, 4, 100$ and 400K in magnetic fields up to 50 kOe .

4. EXPERIMENTAL RESULTS

The temperature dependences of the magnetic susceptibility χ (1) and its inverse value $(1/\chi)$ (2) in a magnetic field $H=1.0 \text{ kOe}$ for single crystals parallel to the plane (001) $\text{Cu}_{1.04}\text{Fe}_{1.12}\text{Te}_{1.84}$ in the temperature range $2-400\text{K}$ are shown in fig.2.

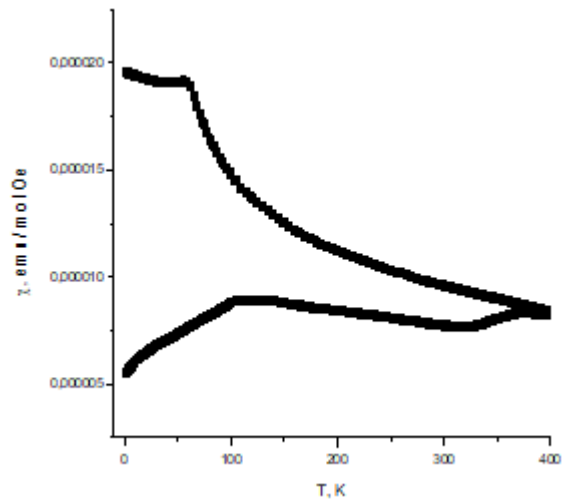


Fig. 2. Magnetic susceptibility of a CFT single crystal in χ ZFC and χ FC modes. The magnetic field $H=1000 \text{ Oe}$ is applied parallel to the plane (001) .

Antiferromagnetically located "clusters" at $T_N=65\text{K}$ are transformed into a paramagnetic state. In the temperature dependence of the magnetic susceptibility $\chi(T)$ below $T_g=65\text{K}$, splitting is observed for the ZFC and FC regimes as in the spin-glass state. In spin glasses below a certain temperature T_g , the spin-glass state (freezing point), a thermodynamic nonequilibrium metastable magnetic state arises,

characterized by a "frozen" spatial random distribution of the orientation of the spin magnetic moments. As can be seen from fig. 2, the course of the temperature dependences of the susceptibility in a weak magnetic field ($H=1.0\text{kOe}$) reveals a divergence of the ZFC-FC curves in the temperature range of 65-350K. These discrepancies in the temperature dependences $\chi(T)$ and $1/\chi(T)$ for ZFC and FC($H=1.0\text{kOe}$) and determination of the irreversibility temperature T_B for CFT single crystals $T_B=360\text{K}$ into the blocked state are characteristic of super paramagnets. The different behavior of the $\chi(T)$ ZFC and $\chi(T)$ FC dependences upon cooling below the blocking temperature ($T \leq T_B$) is one of the main signs that testify in favor of such a transition. To determine the magnetic characteristics of CFT single crystals in the temperature range above T_B , the temperature dependences of the inverse paramagnetic susceptibility $1/\chi(T)$ were plotted in strong fields (up to $H=20\text{kOe}$). As seen from fig. 3, the $\chi(T)$ curves have a maximum at $T_N=T_g=65\text{K}$. Spin-glass state, which is very sensitive to the magnitude of the magnetic field (the highest magnitude of the susceptibility is observed in the smallest magnetic field of the used fields, $H=1.0\text{kOe}$, and it decreases at $H=20\text{kOe}$).

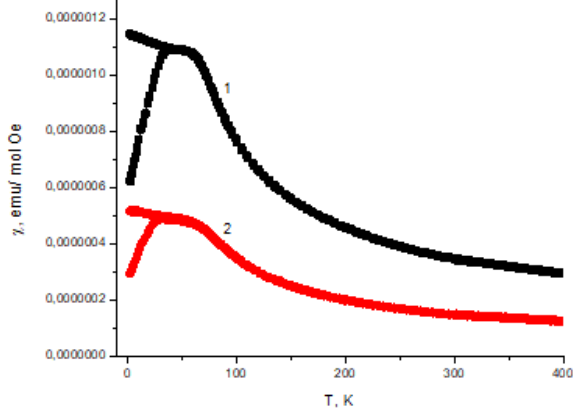


Fig. 3. The magnetic susceptibility of the CFT single crystal in the χ ZFC and χ FC modes, the magnetic field is applied parallel to the (001) plane: 1-10 and 2-20 kOe.

This behavior of the susceptibility χ is typical for spin glasses and was observed by neutron diffraction in $\text{Fe}_{1+\delta-x}\text{Cu}_x\text{Te}$ compounds [3]. The spin-glassy state is also supported by the fact that the low-temperature magnetization of the sample splits in the field or without it. In the intermediate region ($T \approx 65\text{-}360\text{K}$), the contribution of the paramagnetic susceptibility decreases under the influence of superparamagnetic clusters of the ferrimagnetic type and charge carriers. In the temperature range above $T_B > 360\text{K}$, the behavior of the susceptibility is mainly determined by free carriers and paramagnetic centers. The effective magnetic moments of paramagnetic clusters were calculated by linear approximation of the inverse susceptibility dependence for the paramagnetic temperature range. The estimation of the effective magnetic moment of iron ions in CFT from the results of studying the temperature dependences of the magnetic susceptibility $10^{-2}/\chi = f(T)$ was carried out using the expression [15]:

$$M_{\text{eff}} = 2.83 (CM)^{1/2} \mu_B,$$

where, M_{eff} is the effective magnetic moment, C is the Curie constant, M is the molar mass, μ_B is the value in the Bohr magneton.

As can be seen from table 1, the paramagnetic susceptibility obeys the Curie-Weiss law, while the asymptotic Curie temperatures θ_p have a negative sign due to the predominance of antiferromagnetic interaction in clusters, which is consistent with $\text{Cu}_{1.13}\text{Fe}_{1.22}\text{Te}_2$ [16]. This is also evidenced by the form of the temperature dependence of the inverse susceptibility, with the convexity facing upward. 1-1.0, 2-10, and 3-20kOe for the CFT single crystal (fig. 3) in the temperature range 2-400K.

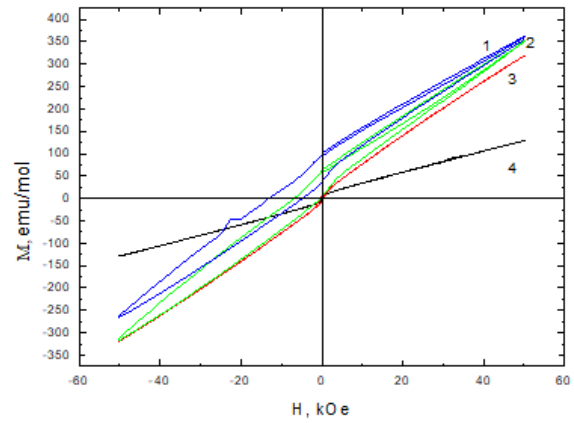


Fig. 4 a. Magnetic hysteresis of a CFT single crystal in the (001) plane at temperatures: 1 - 2, 2 - 4, 3 - 100 and 4 - 300K.

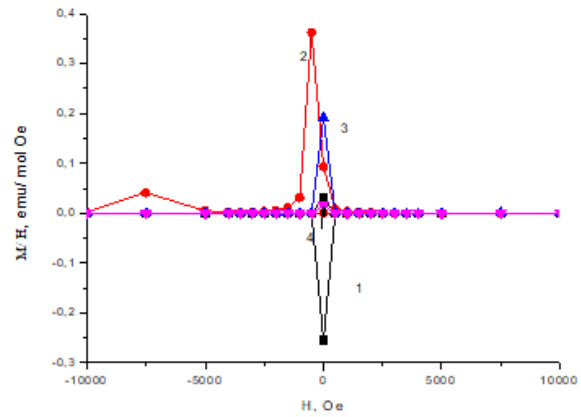


Fig. 4b. Residual magnetization (M/H) in a CFT single crystal in the (001) plane at temperatures: 1-2, 2-4, 3-100 and 4-300K.

Figures 4a and 4b show the isotherms (hysteresis) of magnetization (M) and the ratio of the isotherm of magnetization to the magnetic field M/H (remnant magnetization) of the CFT single crystal in the (001) plane at temperatures of 2, 4, 100, and 300K.

In [18], the temperature dependence $C_p(T)$ of $\text{Cu}_{1.04}\text{Fe}_{1.12}\text{Te}_{1.84}$ was investigated in the temperature range 2-306K. As shown, the total heat capacity CFT is the sum of various contributions, which are complexly dependent on temperature. In the lower part of the

investigated temperature range, the heat capacity can be represented as: $C_p(T) = \Delta C_p + C_D$. Here, the first term is the contribution of various components $\Delta C_p(T)$ to the heat capacity, the second is the lattice (Debye) component of the heat capacity.

5. CONCLUSION

In the *CFT* crystal structure ($P4/nmm$), the chemical bond along the "c" axis as a "cluster" $\text{Cu}^+ - \text{Te}^{2-} - \text{Fe}^{3+} = \text{Te}^{2-}$ and eight such molecules create an antiferromagnetik interaction (see fig.5) [17].

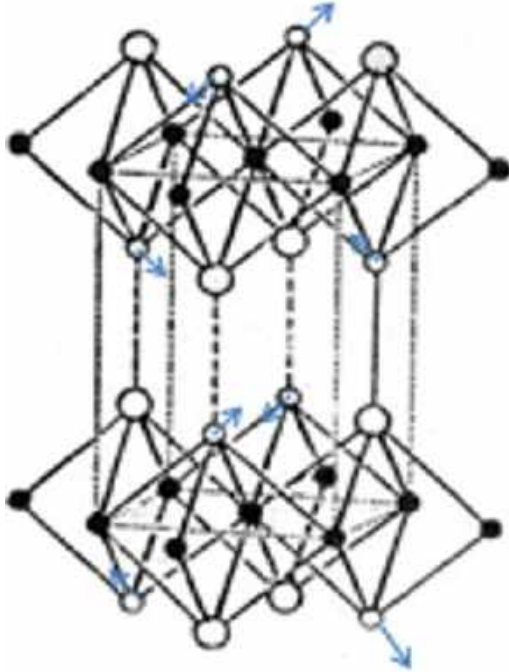


Fig. 5. The direction of the magnetic moments in the CFT structure.

According to the author [17], if the elementary crystallographic cell contains one magnetic ion, then the antiferromagnetik structure in the crystal will have an elementary magnetic cell that is larger than the crystallographic one. If there is more than one magnetic ion in an elementary crystallographic cell, then an alternative is possible for a magnetic cell: preserving the cell or increasing it.

In this *AFM* magnetic structure, the direction of the magnetic moments is shown in fig. 5. In $\text{Cu}_{1.04}\text{Fe}_{1.12}\text{Te}_{1.84}$, the magnetic and spin-glass phase transitions at the temperature $T_N = T_g = 65\text{K}$ coincide. In the (001) plane, the excess (15%) of Cu^{+2} and Fe^{+2} ions are statistically located randomly in the voids of the lattice (fig. 1).

As shown in fig. 4b, these excess copper and iron interact ferrimagnetically and exhibit magnetism (ferron [3], antiferromagnetik [5, 9, 16], spin density waves (*SDW*) [1, 12, 14]) in copper-iron-telluride up to 300K ... The excess component of the heat capacity

$\Delta C_p(T)$, as it were, shows the magnetic contribution of excess cations to the heat capacity [20], repeating the temperature dependence $M/H(T)$.

It was determined that the paramagnetic state of the samples exists in the temperature range exceeding 65K . When approximating the temperature dependences of the magnetic susceptibility in the high-temperature region in accordance with the Curie-Weiss law, it was determined that the paramagnetic Curie temperatures of all studied compounds had a negative sign, which characterizes the possibility of antiferromagnetik interactions between "clusters" and ferrimagnetik orders between magneto active Cu^{+2} and Fe^{+2} (between layers). An analysis of the temperature dependences of the effective magnetic moments (M/H in fig. 4b) in the $65\text{--}350\text{K}$ range for the samples provided additional evidence of the manifestation of such an interaction in the form of an exchange enhancement of paramagnetic with decreasing temperature. The values of M_{eff} , decreasing with increasing temperature, asymptotically approach constant values at temperatures exceeding 65K .

As seen in fig. 2, (1 and 2), the behavior of the temperature dependences of the susceptibility in a weak magnetic field ($H = 1.0\text{ kOe}$) reveals a divergence of the *ZFC* - *FC* curves in the temperature range $65\text{--}360\text{K}$, and at 10 (3 and 4) and 20 *kOe* (5 and 6) match.

Table 1.

H, kOe	1.0	10	20
M_{eff}, μ_B	1.3	2.12	2.22
Θ_P, K	-176	-204	-244

Despite the existence of a single crystallographic structure, sp.gr. $P4/nmm$, $z=1$ for an excess of iron and copper in CuFeTe_2 (*CFT*), at least three different types of these atoms are observed. This situation can arise due to the partial filling of the available intermediates in the structures of copper and iron and the possibility of some ordering of these atoms at the positions ($P4/nmm$). As shown in [1], with the highest magnetic hyperfine field, it probably contains almost isolated ions (Cu , Fe), that is, surrounded by vacancies at intermediate positions, which can be seen in fig. 4b. These results are in good agreement with the Mossbauer spectra of CuFeTe_2 . Any kind of arrangement on interstitial areas has a short-range order, since it is invisible by diffraction methods.

The magnetism of excess iron, copper and spin density waves (*SPW*) are related. The excess of iron and copper indicates some contributions to the hyperfine field causing the *SSW*. While the irregularity of the *VSP* shape is due to the random distribution of interstitial iron. Both types of magnetism disappear at the same transition temperature ($T_N = T_g = 65\text{K}$). However, the available data cannot exclude some other exotic mechanisms of superconductivity.

- [1] A. Rivas, F. Gonzalez, F. Jimenez, L.D'Onofrio, et al. SDW in the 2D Compound CuFeTe_2 - Hyperfine Interactions, 2001, v. 134, p.115-122.
- [2] A. Blachowski, K. Ruebenbaueri, P. Zajdel, E.E. Rodriguez and M.A. Green. Mössbauer study of the '11' iron-based superconductors parent compound Fe_{1+x}Te . J. of Physics: Con. Matt. 24 (38), 386006 (9) (20112). DOI: <http://dx.doi.org/10.1088/0953-8984/24/38/386006>.
- [3] P.N. Valdivia, Kim M.G., Forrest T.R., et al. Copper-substituted iron telluride: A phase diagram //Amer. Phys. Rev. B 91, 2015, 224424.
- [4] A.A. Voipolin, V.D. Prochukhan, Yu.V.Rud, V.E. Skoryukin. Semiconductor properties of CuFeTe_2 . Inorganic materials, 1984, v. 20, № 4, p. 578-581.
- [5] A.I. Dzhabbarov, S.K. Orudzhov, G.G.Guseinov, N.F. Gakhramanov. Growth of single crystals, structural and magnetic properties of CuFeTe_2 . - Crystallography, 2004, v.49, № 6, p. 1136-139.
- [6] F.Yu. Aliev, G.G. Guseinov, A.I. Jabbarov and S.K. Orudzhov. Crystal structure and electrical properties of CuFeTe_2 - Physics. NAS of Azerbaijan. 2000, v.4, № 2, p.58.
- [7] A.I. Nadzhafov, O.Z. Alekperov, G.G.Guseinov and S.K. Orudzhov. Preparation and X-ray diffraction studies of single crystals of tetragonal varieties of CuFeTe_2 - Izv. National Academy of Sciences of Azerbaijan, 2002, № 5, p. 81.
- [8] S.K. Orudzhov, G.G. Guseinov, A.I.Jabbarov, A.I. Najafov and M.M.Akhmedov. Magnetic properties of $\text{Cu}_{1.22}\text{Fe}_{1.1}\text{Te}_2$ single crystals. - Izv. National Academy of Sciences of Azerbaijan, 2004, №2, p. 104-107.
- [9] A.M. Lamarche, J.C. Woolley, G.Lamarche, I.P. Swainson, T.M. Holden. Structure and magnetic properties of the ternary compound copper iron telluride. J. Magn. Mater. 186 (1998) p. 121-128.
- [10] F.N. Abdullaev, T.G. Kerimova, G.D.Sultanov and N.A. Abdullaev. Conduction anisotropy and electron localization in layered CuFeTe single crystals - FTT, 2006, 48 (10), p. 744-1747.
- [11] A.A. Vaipolin, S.A. Kijaev, L.V.Kradinova, A.M. Polubotko, V.V. Popov, V.D.Prochukhan, Yu.V. Rud and V.E.Skoriukin. Investigation of the gapless state in CuFeTe_2 .-J.Phys: Condense. Matter 4 (1992) 8035-8038. Printed in the UK.
- [12] F. Gonzalez-Jimenez, E. Jaimes, A.D. Rivas, L. Onofrio, J. Gonzales, M. Quintero. New spin-density waves systems: Cu and Fe selenides and tellurides. - Physica B 259-261 (1999) 987-989.
- [13] D.F. Zocco, D.Y. Tutun, J.J. Yfmlin, J.R.Jeffries, S.T. Weir, Y.K. Vohra and M.B.Maple. High pressure transport studies of the LiFeAs analogues CuFeTe_2 and Fe_2As . archive: 120/62/2v1 [Cond.-mat.supr -con] 26 Jul 2012.
- [14] A.I. Dzhabbarov, S.K. Orudzhov, G.G.Guseinov, et al. Growth, structure, and magnetic properties of CuFeTe_2 single crystals - Crystallography Reports, 2004, v.49, № 6, p. 1038-1041.
- [15] D. Vaughan and J. Craig. Chemistry of sulfide minerals.- Ed. Mir, Moscow, 1981, p.576.
- [16] A.I. Jabbarov. Magnetic properties of single crystals $\text{Cu}_{1.13}\text{Fe}_{1.22}\text{Te}_2$ and $\text{Cu}_{1.15}\text{Fe}_{1.23}\text{Te}_2$ - News of Azerbaijan National Academy of Sciences Series of physical-technical and mathematical sciences, physics and astronomy, volume XXXVII 31-39.
- [17] F.A. Babushkin. Dynamic theory of magnetic scattering of X-rays in antiferromagnets - Leningrad: Leningrad Publishing House. University, 1979. p.104.
- [18] A.M. Abdullaev, A.M. Aldzhanov, M.J.Najafzadeh, et al. Low-temperature heat capacity, Debye temperature and entropy in $\text{Cu}_{1.04}\text{Fe}_{1.12}\text{Te}_{1.84}$ crystals - Chemical Problems, 2019, № 3 (17), p. 470-479.

Received: 22.09.2020

HIGGS BOSON DECAYS INTO A PAIR OF SUPERSYMMETRIC PARTICLES

S.K. ABDULLAEV, E.SH. OMAROVA

Baku State University

sabdullayev@bsu.edu.az, emiliya.abdullayeva@inbox.ru

Within the framework of the Minimal Supersymmetric Standard Model, the H, h, A and H^\pm Higgs bosons decay channels into a pair of supersymmetric particles were studied: into a pair of chargino $H(h; A) \Rightarrow \chi_i^- \chi_j^+$; a pair of neutralino $H(h; A) \Rightarrow \chi_i^0 \chi_j^0$; in a pair of chargino - neutralino $H^\pm \Rightarrow \chi_i^\pm \chi_j^0$; into a pair of scalar fermions $H(h; A) \Rightarrow \tilde{f}_i \tilde{f}_j$, $H^\pm \Rightarrow \tilde{f}_i \tilde{f}_j'$. Analytical expressions for these decays widths are obtained, the degree of longitudinal polarizations of the chargino and neutralino and the dependence of the decay width on the Higgs boson mass are studied in detail.

Keywords: Standard Model, Minimal Supersymmetric Standard Model, Higgs boson, chargino, neutralino, decay width, sfermion.

PACS: 14.80 Da, 14.80 Ly, 14.80 Nb.

1. INTRODUCTION

The discovery of the Higgs boson H_{SM} with characteristics corresponding to the predictions of the Standard Model (SM) was carried out by the *ATLAS* and *CMS* collaborations in the Large Hadron Collider (*LHC*) in 2012 [1,2] (see also reviews [3-5]). With the discovery of the Higgs boson, a missing brick was found in the SM building and the mechanism for generating masses of fundamental particles, the mechanism of spontaneous breaking of the Braut - Englert-Higgs symmetry, was experimentally confirmed [6,7]. It should be noted that the path to the discovery of the Higgs boson was a long one; at the same time, much work began on its determination of the physical characteristics of this particle.

According to the SM , there are six leptons and six quarks, each comprising three families. The carriers of strong, electromagnetic, and weak interactions are gluons, a photon, charged W^\pm and neutral Z - bosons. Now they are supplemented by the fourth Yukawa interaction carried by Higgs boson H_{SM} .

SM allows you to accurately calculate the Feynman diagrams of various processes and compare with the corresponding experimental data. The agreement between the SM and the experience is strikingly good. Nevertheless, SM has its own difficulties. Many of them are connected with the fact that this model describes a lot, but is not able to explain where it came from, does not allow it to be deduced from deeper principles.

One of the difficulties of SM is related to the problem of hierarchy. According to quantum field theory, vacuum is not an absolute void, but a sea of virtual particles. All real particles of our world are particles dressed in a virtual fur coat. Masses, charges and other characteristics of the observed particles are the characteristics of particles dressed in a fur coat. Theorists take this phenomenon into account using a mathematical procedure called renormalization. The fact is that renormalization works well for all particles, but in the case of the Higgs boson, a problem arises: the influence of virtual particles on the Higgs boson mass is too strong, as a result, the boson mass increases trillions of times, and such a particle can no longer play

the role of the Higgs boson. This difficulty is called the hierarchy problem. This way out of this situation is possible. If in nature there are some other particles that do not exist in the SM , then in a virtual form they can compensate for the influence of the boson on the Higgs mass. The most important thing here is that in supersymmetric theories such compensation itself arises from the construction of the theory. It is such a supersymmetric theory that most attracts theorists.

Another important difficulty of SM is the lack of dark matter particles in it. In astrophysics, it is believed that in the Universe, in addition to ordinary matter in the form of stars, black holes, planets, gas and dust clouds, and. etc., there are particles of a completely different nature. These are particles of dark matter, we do not see them, they practically do not interact with ordinary matter and radiation. Possible candidates for dark matter particles may be neutralino, sneutrino, gluino, gravitino, the existence of which is assumed in the Minimum Supersymmetric Standard Model ($MSSM$) [8-11].

Unlike the SM , the $MSSM$ introduces two doublets of the scalar field with hypercharges -1 and $+1$:

$$\varphi_1 = \begin{pmatrix} H_1^0 \\ H_1^- \end{pmatrix}, \quad \varphi_2 = \begin{pmatrix} H_2^+ \\ H_2^0 \end{pmatrix}.$$

To obtain the physical fields of Higgs bosons, φ_1 and φ_2 we represent in the form

$$\varphi_1 = \frac{1}{\sqrt{2}} \begin{pmatrix} v_1 + H_1^0 + iP_1^0 \\ H_1^- \end{pmatrix},$$

$$\varphi_2 = \frac{1}{\sqrt{2}} \begin{pmatrix} H_2^+ \\ v_2 + H_2^0 + iP_2^0 \end{pmatrix}.$$

where H_1^0, P_1^0, H_2^0 and P_2^0 are the fields describing the excitations of the system relative to vacuum states $\langle \varphi_1 \rangle = \frac{1}{\sqrt{2}} v_1$ and $\langle \varphi_2 \rangle = \frac{1}{\sqrt{2}} v_2$.

The CP -even Higgs bosons H and h are obtained by mixing the fields H_1^0 and H_2^0 (mixing angle α):

$$\begin{pmatrix} H \\ h \end{pmatrix} = \begin{pmatrix} \cos\alpha & \sin\alpha \\ -\sin\alpha & \cos\alpha \end{pmatrix} \begin{pmatrix} H_1^0 \\ H_2^0 \end{pmatrix}.$$

Similarly, mixing P_1^0 and P_2^0 , as well as H_1^\pm and H_2^\pm , one obtains Goldstone bosons G^0 and G^\pm , CP -an odd Higgs boson A and charged Higgs bosons H^\pm (mixing angle β):

$$\begin{pmatrix} G^0 \\ A \end{pmatrix} = \begin{pmatrix} \cos\beta & \sin\beta \\ -\sin\beta & \cos\beta \end{pmatrix} \begin{pmatrix} P_1^0 \\ P_2^0 \end{pmatrix},$$

$$\begin{pmatrix} G^\pm \\ H^\pm \end{pmatrix} = \begin{pmatrix} \cos\beta & \sin\beta \\ -\sin\beta & \cos\beta \end{pmatrix} \begin{pmatrix} H_1^\pm \\ H_2^\pm \end{pmatrix}.$$

Thus, there are five Higgs bosons in the $MSSM$: CP -even H and h -bosons, CP -odd A -boson, charged H^\pm -bosons.

The Higgs sector of the $MSSM$ is characterized by six parameters $M_H, M_h, M_A, M_{H^\pm}, \alpha$ and β . Of these, the parameters M_A and $\tan\beta = \frac{v_1}{v_2}$ are free. The parameter $\tan\beta$ varies within

$$1 \leq \tan\beta \leq \frac{m_t}{m_b} = 35.5.$$

here $m_t = 173.2\text{GeV}$ and $m_b = 4.88\text{GeV}$ of masses of t - and b -quarks.

The Higgs masses of the H - and h - (H^\pm -) bosons are expressed by the masses M_A and M_Z (M_A and M_W):

$$M_{H(h)}^2 = \frac{1}{2} \left[M_A^2 + M_Z^2 \pm \sqrt{(M_A^2 + M_Z^2)^2 - 4M_A^2 M_Z^2 \cos^2 2\beta} \right],$$

$$M_{H^\pm}^2 = M_A^2 + M_W^2.$$

Higgs bosons H, h, A and H^\pm can decay through different channels (see [8, 11–18] and references in them to primary sources. Along with decays of these bosons into ordinary particles, their decay into supersymmetric ones is also possible ($SUSY$) particles:

Chargino, neutralino, and scalar fermions (sfermions) are such particles. The present work is devoted to the study of the decay channels of the Higgs bosons H, h and A into a pair of chargino

$$H(h; A) \Rightarrow \tilde{\chi}_i^- + \tilde{\chi}_j^+, \quad (i, j = 1, 2), \quad (1)$$

$$H(h; A) \Rightarrow \tilde{\chi}_i^0 + \tilde{\chi}_j^0, \quad (i, j = 1 \div 4), \quad (2)$$

$$H^\pm \Rightarrow \tilde{\chi}_i^\pm + \tilde{\chi}_j^0, \quad (i = 1, 2, j = 1 \div 4), \quad (3)$$

$$H(h; A) \Rightarrow \tilde{f}_i + \tilde{f}_j, \quad (i, j = 1, 2), \quad (4)$$

$$H^\pm \Rightarrow \tilde{f}_i + \tilde{f}_j', \quad (i, j = 1, 2). \quad (5)$$

Within the framework of the $MSSM$ and taking into account the polarization states of the chargino, analytical expressions for the width of the indicated decays are obtained, the degrees of the longitudinal and transverse polarizations of the chargino are determined, the dependence of these characteristics and the width of the decays on the mass of Higgs bosons is studied.

2. HIGGS BOSON DECAYS IN A PAIR OF CHARGINO

The supersymmetric partnyors of the gauge W^\pm and Higgs H^\pm -bosons are calibrino (vino) \tilde{W}^\pm and Higgsino \tilde{H}^\pm . The mass matrix of these spinor fields is off-diagonal, which leads to their mixing. Chargino $\tilde{\chi}^\pm$ is a four-component. Dirac fermion that occurs when vino \tilde{W}^\pm and Higgsino \tilde{H}^\pm are mixed. The masses and coupling constants of the chargino with the Higgs bosons H, h, A, H^\pm are determined by the mass matrix.

$$M_{\tilde{\chi}^\pm} = \begin{pmatrix} M_2 & \sqrt{2}M_W \sin\beta \\ \sqrt{2}M_W \cos\beta & \mu \end{pmatrix},$$

where M_2 and μ - mass parameters of vino and Higgsino. This matrix is diagonalized by two real two-

row U and V matrices.

$$UM_{\tilde{\chi}^\pm}V^{-1} \Rightarrow U = R_- \text{ and } V = \begin{cases} R_+, & \text{if } \det M_{\tilde{\chi}^\pm} > 0 \\ \sigma_3 R_+, & \text{if } \det M_{\tilde{\chi}^\pm} < 0, \end{cases}$$

where σ_3 is the Pauli matrix, which makes the chargino mass positive, R_\pm are the rotation matrices with angles θ_\pm :

$$R_\pm = \begin{pmatrix} \cos\theta_\pm & \sin\theta_\pm \\ -\sin\theta_\pm & \cos\theta_\pm \end{pmatrix},$$

and the angles θ_+ and θ_- are defined as

$$\tan 2\theta_+ = \frac{2\sqrt{2}M_W(M_2 \sin\beta + \mu \cos\beta)}{M_2^2 - \mu^2 + 2M_W^2 \cos\beta},$$

$$\tan 2\theta_- = \frac{2\sqrt{2}M_W(M_2 \cos\beta + \mu \sin\beta)}{M_2^2 - \mu^2 - 2M_W^2 \cos\beta}.$$

After diagonalizing the matrix $M_{\tilde{\chi}^\pm}$, new states of chargeino with masses are obtained:

$$m_{\tilde{\chi}_{1,2}^\pm}^2 = \frac{1}{2} \{ M_2^2 + \mu^2 + 2M_W^2 \mp [(M_2^2 + \mu^2)^2 + 4M_W^2(M_W^2 \cos^2 2\beta + M_2^2 + \mu^2 + 2M_2\mu \sin 2\beta)]^{1/2} \}. \quad (6)$$

If one of the two parameters μ or M_2 has a very large value, then one state of the chargino corresponds to the calibrino state and the other to the Higgsino state. In this case, the masses of the chargino are equal: at

$$|\mu| \gg M_Z, \quad M_2 \sim M_Z : m_{\tilde{\chi}_1^\pm} \sim M_2, \quad m_{\tilde{\chi}_2^\pm} \sim |\mu|;$$

at

$$|\mu| \sim M_Z, \quad M_2 \gg M_Z : m_{\tilde{\chi}_1^\pm} \sim |\mu|, \quad m_{\tilde{\chi}_2^\pm} \sim M_2.$$

Figure 1 shows the dependence of the chargino mass $\tilde{\chi}_1^\pm$ and $\tilde{\chi}_2^\pm$ on the parameter μ at $\tan\beta = 30$ and the fixed mass $M_2 = 150\text{GeV}$. As can be seen, with an increase in the moduls of the parameter $|\mu|$ the mass of light (heavy) chargino $m_{\tilde{\chi}_1^\pm}$ ($m_{\tilde{\chi}_2^\pm}$) monotonously increases and approaches the value of 147GeV

(512GeV) at $\mu = -500\text{GeV}$ and 145GeV (514GeV) at $\mu = 500\text{GeV}$. The minimum value of the chargino mass $m_{\tilde{\chi}_1^\pm}$ and $m_{\tilde{\chi}_2^\pm}$ is observed at a zero value of the parameter μ : $m_{\tilde{\chi}_1^\pm}(\mu = 0) = 2,696\text{GeV}$, $m_{\tilde{\chi}_2^\pm}(\mu = 0) = 188.192\text{GeV}$.

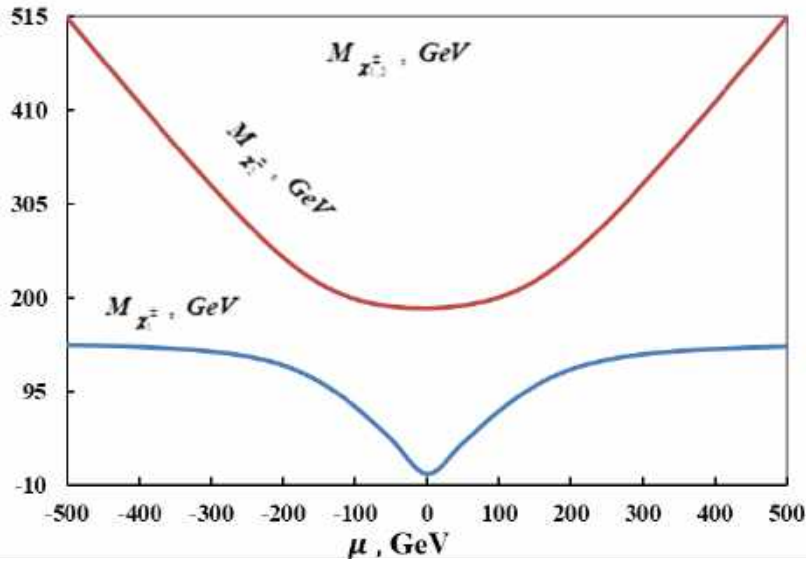


Fig. 1. Chargino masses $m_{\tilde{\chi}_1^\pm}$ and $m_{\tilde{\chi}_2^\pm}$ as a function of the parameter μ

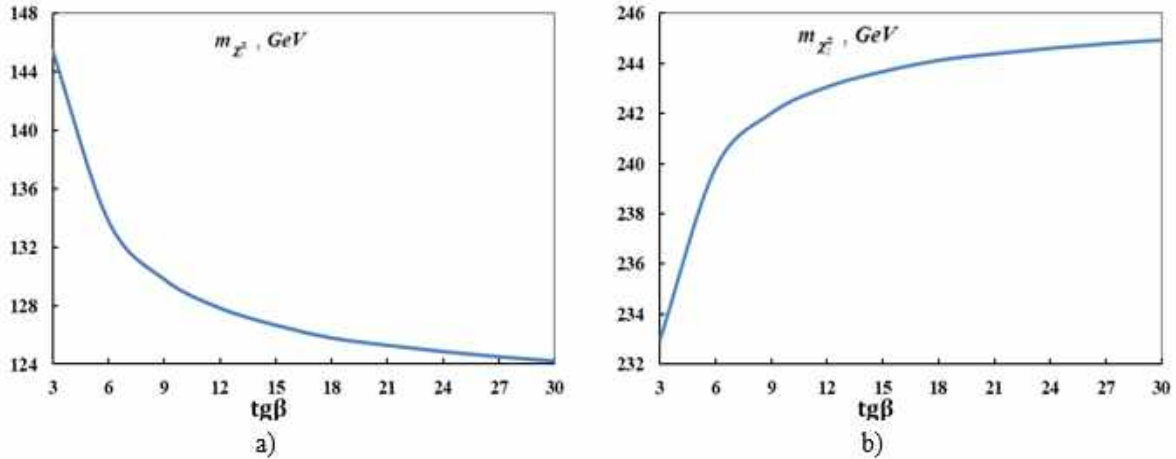


Fig. 2. Dependence of the mass $m_{\tilde{\chi}_1^\pm}$ (a) and $m_{\tilde{\chi}_2^\pm}$ (b) on the parameter $\tan\beta$

Note that, for a given parameter μ , the chargino masses $m_{\tilde{\chi}_1^\pm}$ and $m_{\tilde{\chi}_2^\pm}$ are very sensitive to the $\tan\beta$ parameter (see fig. 2, where the dependence of the mass $m_{\tilde{\chi}_1^\pm}$ and $m_{\tilde{\chi}_2^\pm}$ of the $\tan\beta$ parameter for $M_2 = 150\text{GeV}$, $\mu = -200\text{GeV}$). As can be seen from the figure, with an increase in the parameter $\tan\beta$, the chargino mass $m_{\tilde{\chi}_1^\pm}$ monotonously decreases, and the charge chargino $m_{\tilde{\chi}_2^\pm}$ on the contrary, increases monotonously. With a positive value of the parameter $\mu = 200\text{GeV}$, an inverse relationship is observed: with an increase in the $\tan\beta$ parameter, the chargino mass $m_{\tilde{\chi}_1^\pm}$ increases and the mass $m_{\tilde{\chi}_2^\pm}$ on the contrary, decreases.

The Feynman diagram of the Higgs boson decay $H_k \Rightarrow \tilde{\chi}_i^- + \tilde{\chi}_j^+$ is shown in fig. 3 (the $k = 1, 2, 3$ index corresponds to the neutral Higgs bosons H, h, A and the $i, j = 1, 2$ indexes correspond to the chargino).

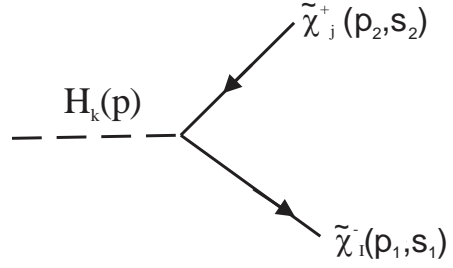


Fig. 3. Feynman diagram for $H_k \Rightarrow \tilde{\chi}_i^- \tilde{\chi}_j^+$ decay. In the figure p , p_1 and p_2 denote 4 - momenta of Higgs boson H_k , $\tilde{\chi}_i^-$ and $\tilde{\chi}_j^+$ chargino, s_1 and s_2 4 - polarization vectors of chargino.

According to the *MSSM*, the amplitude corresponding to the diagram in fig. 3 can be written in the following form:

$$M(H_k \Rightarrow \tilde{\chi}_i^- \tilde{\chi}_j^+) = ig [g_{ijk}^L \bar{u}(p_1, s_1) P_L v(p_2, s_2) + g_{ijk}^R \bar{u}(p_1, s_1) P_R v(p_2, s_2)], \quad (7)$$

where g is a constant determining the mass of the gauge W - boson

$$M_W^2 = \frac{1}{2} g^2 (v_1^2 + v_2^2);$$

$P_{L,R} = \frac{(1 \pm \gamma_5)}{2}$ is chirality matrices, g_{ijk}^L and g_{ijk}^R is interaction constants of the Higgs boson H_k with chargino $\tilde{\chi}_i^- \tilde{\chi}_j^+$ [8,11]

$$\begin{aligned} g_{ijk}^L &= \frac{1}{\sqrt{2}} [V_{j1} U_{i2} e_k - V_{j2} U_{i1} d_k], \\ g_{ijk}^R &= \frac{1}{\sqrt{2}} [V_{i1} U_{j2} e_k - V_{i2} U_{j1} d_k] \epsilon_k, \end{aligned} \quad (8)$$

$\epsilon_1 = \epsilon_2 = -\epsilon_3 = 1$; the coefficients e_k and d_k are equal to:

$$\begin{aligned} e_1 &= \cos\alpha, e_2 = -\sin\alpha, e_3 = -\sin\beta, \\ d_1 &= -\sin\alpha, d_2 = -\cos\alpha, d_3 = \cos\beta. \end{aligned} \quad (9)$$

To find the probabilities (width) of the Higgs boson decay into a pair of chargino, we must squared the amplitude moduls $|M(H_k \Rightarrow \tilde{\chi}_i^- \tilde{\chi}_j^+)|^2$. In the standard way for the squared amplitude module, we find:

$$\begin{aligned} |M(H_k \Rightarrow \tilde{\chi}_i^- \tilde{\chi}_j^+)|^2 &= \frac{g^2}{2} \{ [(g_{ijk}^L)^2 + (g_{ijk}^R)^2] [(p_1 \cdot p_2) + m_{\tilde{\chi}_i} m_{\tilde{\chi}_j} (s_1 \cdot s_2)] + [(g_{ijk}^L)^2 - (g_{ijk}^R)^2] \times \\ &\times [m_{\tilde{\chi}_i} (p_2 \cdot s_1) + m_{\tilde{\chi}_j} (p_1 \cdot s_2)] + 2g_{ijk}^L g_{ijk}^R [-m_{\tilde{\chi}_i} m_{\tilde{\chi}_j} - (p_1 \cdot p_2)(s_1 \cdot s_2) + (p_1 \cdot s_2)(p_2 \cdot s_1)] \}. \end{aligned} \quad (10)$$

In the Higgs boson rest system H_k the energy and the modules of the three-dimensional chargino momentum are determined by the expressions:

$$E_1 = \frac{1}{2} M_H (1 + r_i - r_j), \quad E_2 = \frac{1}{2} M_H (1 - r_i + r_j),$$

$$|\vec{p}_1| = |\vec{p}_2| = |\vec{p}| = \frac{1}{2} M_H \sqrt{(1 - r_i - r_j)^2 - 4r_i r_j},$$

here the notation

$$r_i = \left(\frac{m_{\tilde{\chi}_i^\pm}}{M_{H_k}} \right)^2, \quad r_j = \left(\frac{m_{\tilde{\chi}_j^\pm}}{M_{H_k}} \right)^2.$$

Given the polarization states of the chargino $\tilde{\chi}_i^-$ and $\tilde{\chi}_j^+$, the decay width $H_k \Rightarrow \tilde{\chi}_i^- + \tilde{\chi}_j^+$ has the form:

$$\begin{aligned} \frac{d\Gamma(\vec{\xi}_1, \vec{\xi}_2)}{d\Omega} = & \frac{G_F M_W^2}{32\sqrt{2}\pi^2} M_{H_k} \sqrt{(1-r_i-r_j)^2 - 4r_i r_j} \left\{ \left[(g_{ijk}^L)^2 + (g_{ijk}^R)^2 \right] [(1-r_i-r_j)(1-(\vec{n}\vec{\xi}_1)(\vec{n}\vec{\xi}_2)) + \right. \\ & + 2\sqrt{r_i r_j} \times (-\vec{\xi}_1 \vec{\xi}_2) + (\vec{n}\vec{\xi}_1)(\vec{n}\vec{\xi}_2)] + \left. \left[(g_{ijk}^L)^2 - (g_{ijk}^R)^2 \right] \sqrt{(1-r_i-r_j)^2 - 4r_i r_j} [(\vec{n}\vec{\xi}_1) - \right. \\ & \left. - (\vec{n}\vec{\xi}_2)] - 4g_{ijk}^L g_{ijk}^R \times \left[\sqrt{r_i r_j} (1 - (\vec{n}\vec{\xi}_1)(\vec{n}\vec{\xi}_2)) - \frac{1}{2}(1-r_i-r_j)(\vec{\xi}_1 \vec{\xi}_2) - (\vec{n}\vec{\xi}_1)(\vec{n}\vec{\xi}_2) \right] \right\} \end{aligned} \quad (11)$$

where \vec{n} is the unit vector, in the direction of the charge of the chargino $\tilde{\chi}_i^-$, $\vec{\xi}_1$ and $\vec{\xi}_2$ are the unit vectors characterizing the polarization of the chargino $\tilde{\chi}_i^-$ and $\tilde{\chi}_j^+$ in the rest systems of each of these particles, respectively; $\lambda(r_i, r_j) = (1-r_i-r_j)^2 - 4r_i r_j$ is the kinematic function of a two-particle phase volume.

We consider particular cases of the decay width formula (9). First, suppose that the chargino is polarized longitudinally, while

$$\vec{\xi}_1 = \vec{n}\lambda_1, \quad \vec{\xi}_2 = -\vec{n}\lambda_2,$$

where λ_1 and λ_2 are the spiralities of the chargino $\tilde{\chi}_i^-$ and $\tilde{\chi}_j^+$

In this case, the decay width $H_k \Rightarrow \tilde{\chi}_i^- + \tilde{\chi}_j^+$ is determined by the expression:

$$\Gamma(\lambda_1, \lambda_2) = \frac{1}{4} \Gamma_0(H_k \Rightarrow \tilde{\chi}_i^- \tilde{\chi}_j^+) [1 + \lambda_1 \lambda_2 + (\lambda_1 + \lambda_2)P], \quad (12)$$

here

$$\Gamma_0(H_k \Rightarrow \tilde{\chi}_i^- \tilde{\chi}_j^+) = \frac{G_F M_W^2}{2\sqrt{2}\pi} M_{H_k} \sqrt{(1-r_i-r_j)^2 - 4r_i r_j} \left\{ \left[(g_{ijk}^L)^2 + (g_{ijk}^R)^2 \right] (1-r_i-r_j) - 4g_{ijk}^L g_{ijk}^R \sqrt{r_i r_j} \right\} \quad (13)$$

is the decay width in the case of unpolarized chargino, and P is the degree of longitudinal polarization of chargino, defined by the formula

$$P = \frac{\left[(g_{ijk}^L)^2 - (g_{ijk}^R)^2 \right] \sqrt{(1-r_i-r_j)^2 - 4r_i r_j}}{\left[(g_{ijk}^L)^2 + (g_{ijk}^R)^2 \right] (1-r_i-r_j) - 4g_{ijk}^L g_{ijk}^R \sqrt{r_i r_j}}. \quad (14)$$

It follows from the decay width (12) that, in the Higgs boson decay $H_k \Rightarrow \tilde{\chi}_i^- + \tilde{\chi}_j^+$ the chargino $\tilde{\chi}_i^-$ and $\tilde{\chi}_j^+$ must have the same $\lambda_1 = \lambda_2 = \pm 1$ helicities ($\tilde{\chi}_{iR}^- \tilde{\chi}_{jR}^+$ or $\tilde{\chi}_{iL}^- \tilde{\chi}_{jL}^+$). This is a consequence of maintaining the full moment in $H_k \Rightarrow \tilde{\chi}_i^- + \tilde{\chi}_j^+$ decays. Consider this decay in the resting system of the Higgs boson H_k . In this system, the momenta of the chargino $\tilde{\chi}_i^-$ and $\tilde{\chi}_j^+$ are equal in magnitude and opposite in

direction (see fig. 4, which shows the directions of the charge and spin of the chargino). Since the Higgs boson H_k is zero, the process $H_k \Rightarrow \tilde{\chi}_i^- + \tilde{\chi}_j^+$ is allowed only if the chargino $\tilde{\chi}_i^-$ and $\tilde{\chi}_j^+$ are in the same helicity state. It is in this case that the projection of the total moment of two chargino in the direction of movement of chargino $\tilde{\chi}_i^-$ (or $\tilde{\chi}_j^+$) is zero.

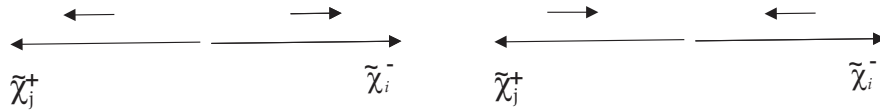


Fig. 4. Direction of momenta and spins in $H_k \Rightarrow \tilde{\chi}_i^- \tilde{\chi}_j^+$ decay

We estimate the degree of longitudinal polarization of chargino (12) at $\tan\beta = 1$. Calculations show that, at this value of the parameter $\tan\beta$, the interaction constants g_{ijk}^L and g_{ijk}^R are equal to each other in the decays $H(h; A) \Rightarrow \tilde{\chi}_i^- + \tilde{\chi}_j^+$, as a result of which the degree of longitudinal polarization of the chargino vanishes.

Now consider the case when the charginos are transversely polarized. Where in

$$(\vec{n}\vec{\xi}_1) = (\vec{n}\vec{\eta}_1) = 0, \quad (\vec{n}\vec{\xi}_2) = (\vec{n}\vec{\eta}_2) = 0$$

$$(\vec{\xi}_1 \vec{\xi}_2) = (\vec{\eta}_1 \vec{\eta}_2) = \eta_1 \eta_2 \cos\varphi$$

where $\vec{\eta}_1$ and $\vec{\eta}_2$ are the transverse components of the chargino vectors $\tilde{\chi}_i^-$ and $\tilde{\chi}_j^+$, φ is the angle between these vectors. In this case, the decay width $H_k \Rightarrow \tilde{\chi}_i^- + \tilde{\chi}_j^+$ is

$$\frac{d\Gamma(\eta_1, \eta_2)}{d\Omega} = \frac{1}{4} \frac{d\Gamma_0(H_k \Rightarrow \tilde{\chi}_i^- \tilde{\chi}_j^+)}{d\Omega} [1 + \eta_1 \eta_2 P_\perp], \quad (15)$$

where

$$\frac{d\Gamma_0(H_k \Rightarrow \tilde{\chi}_i^- \tilde{\chi}_j^+)}{d\Omega} = \frac{G_F M_W^2}{8\sqrt{2}\pi^2} M_{H_k} \sqrt{\lambda(r_i, r_j)} \left\{ \left[(g_{ijk}^L)^2 + (g_{ijk}^R)^2 \right] (1 - r_i - r_j) - 4g_{ijk}^L g_{ijk}^R \sqrt{r_i r_j} \right\} \quad (16)$$

is the decay width for unpolarized chargino, and P_\perp is the degree of transverse polarization of chargino :

$$P_\perp = \frac{2g_{ijk}^L g_{ijk}^R (1 - r_i - r_j) - 2[(g_{ijk}^L)^2 + (g_{ijk}^R)^2] \sqrt{r_i r_j}}{[(g_{ijk}^L)^2 + (g_{ijk}^R)^2] (1 - r_i - r_j) - 4g_{ijk}^L g_{ijk}^R \sqrt{r_i r_j}} \cdot \cos\varphi. \quad (17)$$

At $\tan\beta = 1$ due to the equality of the interaction constants $g_{ijk}^L = g_{ijk}^R$ the degree of transverse polarization depends only on the cosinus of the angle between the spin vectors \vec{n}_1 and \vec{n}_2 :

$$P_\perp = \cos\varphi. \quad (18)$$

At $\varphi = 0^\circ$ the degree of transverse polarization of the chargino is +1, with increasing angle φ , the degree of transverse polarization decreases and vanishes at an angle $\varphi = 90^\circ$. Then, the degree of transverse polarization changes sign and decreases to -1 at $\varphi = 180^\circ$. A further increase in the angle φ from 180° to 360°

leads to an increase in the degree of transverse polarization from -1 to +1. It should be noted that in the approximation $|\mu| \gg M_2$ or $M_2 \gg |\mu|$ the decays of the Higgs bosons into a pair of identical chargino $H_k \Rightarrow \tilde{\chi}_1^- + \tilde{\chi}_1^+ (\tilde{\chi}_2^- + \tilde{\chi}_2^+)$ are suppressed.

In this case, the decays of the heavy H and A bosons into a pair of different $H(A) \Rightarrow \tilde{\chi}_1^- + \tilde{\chi}_2^+$ chargino dominate. In fig.5 shows the dependence of decay $H \Rightarrow \tilde{\chi}_1^- + \tilde{\chi}_2^+$ width on the Higgs boson mass M_H at $\tan\beta = 1$, $\mu = 160\text{GeV}$, $M_2 = 150\text{GeV}$, $M_W = 80.385\text{GeV}$, $M_Z = 91.1875\text{GeV}$.

With an increase in the Higgs boson mass M_H the decay width increases.

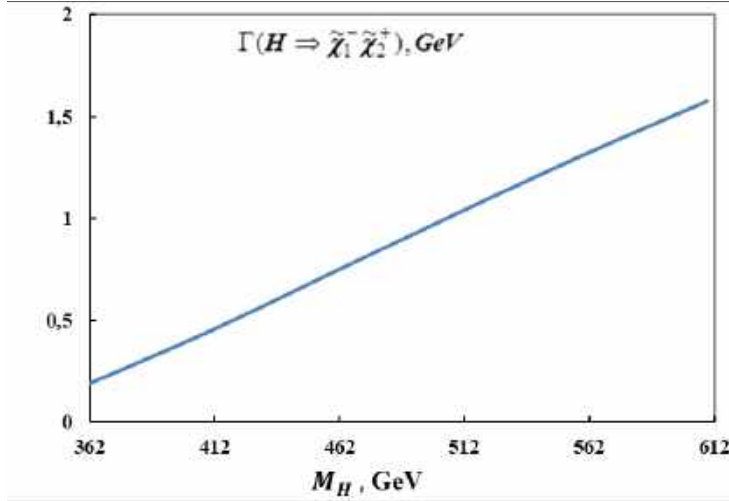


Fig. 5. Dependence of the decay width $H \Rightarrow \tilde{\chi}_1^- \tilde{\chi}_2^+$ on the mass M_H

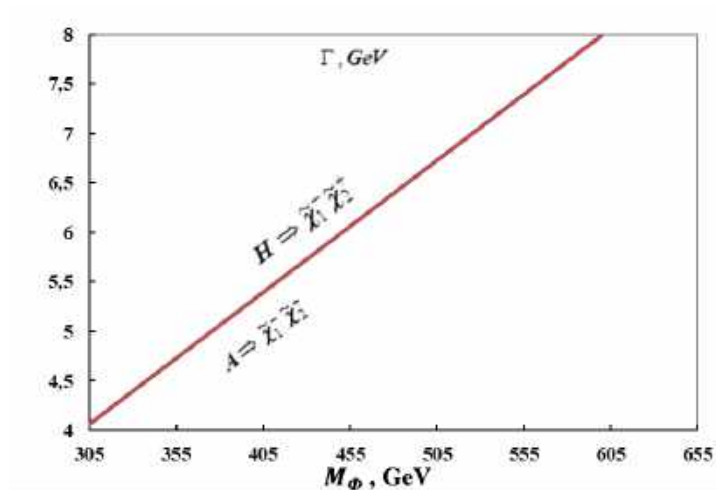


Fig. 6. Dependence of the decay width $\Gamma(H(A) \Rightarrow \tilde{\chi}_1^- \tilde{\chi}_2^+)$ on the mass M_Φ

In the $M_A \gg |\mu| \gg M_2$ limit, the partial decay widths of $H \Rightarrow \tilde{\chi}_1^\pm + \tilde{\chi}_2^\mp$ and $A \Rightarrow \tilde{\chi}_1^\pm + \tilde{\chi}_2^\mp$ are equal

$$\Gamma(H \Rightarrow \tilde{\chi}_1^- \tilde{\chi}_2^+) = \frac{G_F M_W^2}{4\sqrt{2}\pi} M_H, \quad (18)$$

$$\Gamma(A \Rightarrow \tilde{\chi}_1^- \tilde{\chi}_2^+) = \frac{G_F M_W^2}{4\sqrt{2}\pi} M_A.$$

The dependence of the width of these decays on the Higgs mass M_H and M_A boson is shown in fig. 6. At $M_\Phi = 305\text{GeV}$, the decay width is 4GeV , with an increase in the Higgs boson mass, the decay width increases, and with a mass $M_\Phi = 602\text{GeV}$, the decay width reaches 8GeV .

3. HIGGS BOSON DECAYS INTO A PAIR OF NEUTRALINO

Neutral vino \tilde{W}^0 and bino \tilde{B}^0 , as well as Higgsino \tilde{H}_1^0 and \tilde{H}_2^0 interact weakly, they are not proper mass states. The four mass states of the neutralino $\tilde{\chi}_i^0$ ($i = 1, 2, 3, 4$) are alternating combinations of the particles mentioned above. Neutralino - Majorana fermions, their antiparticles coincide with their particles. The neutralino mass matrix, as in the case of the chargino, depends on the parameters, M_2 , $\tan\beta$ and also on the new mass parameter M_1 of the bino \tilde{B}^0 [8, 11]. As in the case of the chargino, with a large value of one of the parameters μ or M_2 , two neutralino correspond to a pure gaugino-like state, and the other neutralino ones correspond to a pure Higgsino-like state. In these limiting states, the neutralino masses are equal to:

$$\begin{aligned} \text{at } |\mu| \gg M_Z, \quad M_2 \sim M_Z : m_{\tilde{\chi}_1^0} \sim M_1, \quad m_{\tilde{\chi}_2^0} \sim M_2, \quad m_{\tilde{\chi}_3^0} \cong m_{\tilde{\chi}_4^0} \cong |\mu|, \\ \text{at } |\mu| \sim M_Z, \quad M_2 \gg M_Z : m_{\tilde{\chi}_1^0} \cong m_{\tilde{\chi}_2^0} \cong |\mu|, \quad m_{\tilde{\chi}_3^0} \cong M_1, \quad m_{\tilde{\chi}_4^0} \cong M_2. \end{aligned}$$

The decay width of the Higgs bosons H_k into a neutralino pair for arbitrarily polarized particles is determined by a formula similar to formula (11). In a particular case, the decay width $H_k \Rightarrow \tilde{\chi}_i^0 + \tilde{\chi}_j^0$ in the case of the production of a longitudinally polarized neutralino pair is determined by the expression:

$$\Gamma(\lambda_1, \lambda_2) = \frac{1}{4} \Gamma_0(H_k \Rightarrow \tilde{\chi}_i^0 \tilde{\chi}_j^0) [1 + \lambda_1 \lambda_2 + (\lambda_1 + \lambda_2)P], \quad (19)$$

here

$$\Gamma_0(H_k \Rightarrow \tilde{\chi}_i^0 \tilde{\chi}_j^0) = \frac{G_F M_W^2}{2\sqrt{2}\pi} M_{H_k} \delta \sqrt{\lambda(r_i, r_j)} \left\{ \left[(g_{ijk}^L)^2 + (g_{ijk}^R)^2 \right] (1 - r_i - r_j) - 4\varepsilon_i \varepsilon_j g_{ijk}^L g_{ijk}^R \sqrt{r_i r_j} \right\} \quad (20)$$

is the width of this decay in the case of unpolarized neutralino, and P is the degree of longitudinal polarization of neutralino, defined by the expression

$$P = - \frac{[(g_{ijk}^L)^2 - (g_{ijk}^R)^2] \sqrt{\lambda(r_i, r_j)}}{[(g_{ijk}^L)^2 + (g_{ijk}^R)^2] (1 - r_i - r_j) - 4\varepsilon_i \varepsilon_j g_{ijk}^L g_{ijk}^R \sqrt{r_i r_j}}; \quad (21)$$

the factor δ in formula (20) is equal to $1\left(\frac{1}{2}\right)$, if a pair of different (identical) neutralinos are born, ε_i and ε_j

determine the sign of the parameter μ , g_{ijk}^L and g_{ijk}^R are the interaction constants of the Higgs boson H_k with a pair of neutralino [8, 11]:

$$\begin{aligned} g_{ijk}^L &= \frac{1}{2} (Z_{j2} - \tan\theta_W Z_{j1}) (Z_{i3} e_k + Z_{i4} d_k) + i \rightarrow j, \\ g_{ijk}^R &= \frac{1}{2} (Z_{j2} - \tan\theta_W Z_{j1}) (Z_{i3} e_k + Z_{j4} d_k) \varepsilon_k + i \rightarrow j; \end{aligned} \quad (22)$$

Z is 4×4 matrix diagonalizing the neutralino mass matrix; $\varepsilon_1 = \varepsilon_2 = -\varepsilon_3 = 1$; the coefficients e_k and d_k are given by expressions (9); θ_W is the Weinberg angle.

Denote the simplest neutralino by $\tilde{\chi}^0$; it can be the easiest *SUSY* particle. Then all other *SUSY* particles will decay into $\tilde{\chi}^0$ and ordinary *SM* particles. Table 1 shows the upper bounds on the masses of *SUSY* particles for various values of the parameter $\tan\beta$. In the table, $\tilde{\tau}$ and \tilde{t} are sfermions - stau lepton and stop quark.

Table 1.

Upper Boundaries for *SUSY* Particle Masses

$\tan\beta$	$\tilde{\chi}^0$	$\tilde{\chi}^-$	$\tilde{\tau}$	\tilde{t}
10	155	280	170	580
15	168	300	185	640
20	220	400	236	812
30	260	470	280	990

Calculations show that the decay widths of the heavy Higgs bosons H and A into a pair of different neutralinos $\tilde{\chi}_1^0\tilde{\chi}_3^0$, $\tilde{\chi}_1^0\tilde{\chi}_4^0$, $\tilde{\chi}_2^0\tilde{\chi}_3^0$ and $\tilde{\chi}_2^0\tilde{\chi}_4^0$ are prevailed. The widths of these decays are shown in Table 2 (in units of $\frac{G_F M_W^2}{8\sqrt{2}\pi} M_{H_k}$).

Table 2.

Decay widths of H and A into a neutralino pair

Neutralino pair	$\Gamma(H \Rightarrow \tilde{\chi}_i^0 \tilde{\chi}_j^0)$	$\Gamma(A \Rightarrow \tilde{\chi}_i^0 \tilde{\chi}_j^0)$
$\tilde{\chi}_1^0 \tilde{\chi}_3^0$	$\tan^2\theta_W(1 + \sin 2\beta)$	$\tan^2\theta_W(1 - \sin 2\beta)$
$\tilde{\chi}_1^0 \tilde{\chi}_4^0$	$\tan^2\theta_W(1 - \sin 2\beta)$	$\tan^2\theta_W(1 + \sin 2\beta)$
$\tilde{\chi}_2^0 \tilde{\chi}_3^0$	$(1 + \sin 2\beta)$	$(1 - \sin 2\beta)$
$\tilde{\chi}_2^0 \tilde{\chi}_4^0$	$(1 - \sin 2\beta)$	$(1 + \sin 2\beta)$

Fig. 7(a) and (b) illustrate the dependence of the decay width $H \Rightarrow \tilde{\chi}_2^0 + \tilde{\chi}_3^0$ and $A \Rightarrow \tilde{\chi}_2^0 + \tilde{\chi}_4^0$ on the Higgs boson mass M_H and M_A for $\tan\beta = 3$, $\sin^2\theta_W = 0.2315$. In these figures, the decay width $H \Rightarrow \tilde{\chi}_2^0 + \tilde{\chi}_3^0$ and $A \Rightarrow \tilde{\chi}_2^0 + \tilde{\chi}_4^0$ with an increase in the Higgs boson masses the H and A are observed.

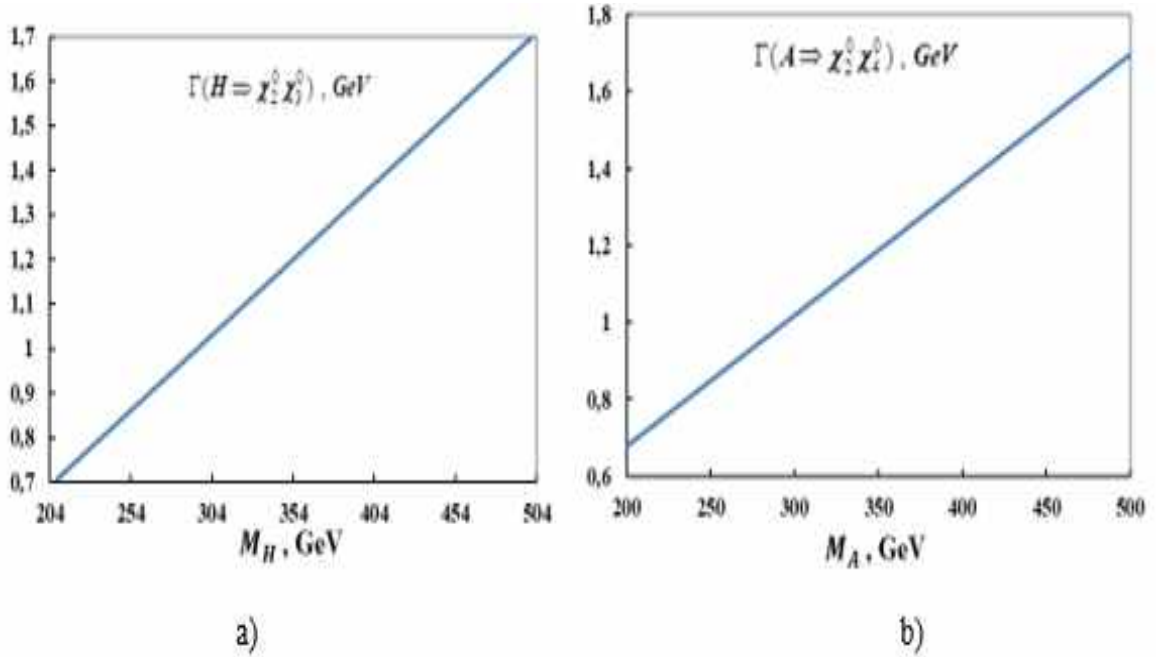


Fig. 7. Dependence of the decay width $H \Rightarrow \tilde{\chi}_2^0 + \tilde{\chi}_3^0$ (a) and $A \Rightarrow \tilde{\chi}_2^0 + \tilde{\chi}_4^0$ (b) on the masses M_H and M_A

4. DECAYS OF HIGGS BOSON H^\pm INTO THE CHARGINO - NEUTRALINO PAIR

The charged Higgs boson H^\pm can decay into a pair of chargino-neutralino along the channel $H^\pm \Rightarrow \tilde{\chi}_i^\pm + \tilde{\chi}_j^0$. Having performed standard calculations, we obtain for the decay width $H^- \Rightarrow \tilde{\chi}_i^- + \tilde{\chi}_j^0$ in the Higgs boson rest system :

$$\begin{aligned} \frac{d\Gamma(\vec{\xi}_1, \vec{\xi}_2)}{d\Omega} = \frac{G_F M_W^2}{32\sqrt{2}\pi^2} M_{H^-} \sqrt{\lambda(r_i, r_j)} \{ & [(g_{ijk}^L)^2 + (g_{ijk}^R)^2] [(1 - r_i - r_j)(1 - (\vec{n}\vec{\xi}_1)(\vec{n}\vec{\xi}_2)) - 2\sqrt{r_i r_j} \times \\ & \times ((\vec{\xi}_1\vec{\xi}_2) - (\vec{n}\vec{\xi}_1)(\vec{n}\vec{\xi}_2))] + [(g_{ijk}^L)^2 - (g_{ijk}^R)^2] \sqrt{\lambda(r_i, r_j)} [(\vec{n}\vec{\xi}_1) - (\vec{n}\vec{\xi}_2)] + 2g_{ijk}^L g_{ijk}^R \times \\ & \times [(1 - r_i - r_j)((\vec{\xi}_1\vec{\xi}_2) - (\vec{n}\vec{\xi}_1)(\vec{n}\vec{\xi}_2)) - 2\sqrt{r_i r_j}(1 - (\vec{n}\vec{\xi}_1)(\vec{n}\vec{\xi}_2))] \}. \end{aligned} \quad (23)$$

Here \vec{n} is a unit vector in the direction of the mometum of the chargino; $\vec{\xi}_1$ and $\vec{\xi}_2$ are unit vectors characterizing the polarization of chargino and neutralino; $d\Omega = \sin\theta d\theta d\varphi$ is the solid angle of departure of the chargino; $\lambda(r_i, r_j)$ is a kinematic function ;

$$r_i = \left(\frac{m_{\tilde{\chi}_i^-}}{M_{H^-}}\right)^2, \quad r_j = \left(\frac{m_{\tilde{\chi}_j^0}}{M_{H^-}}\right)^2;$$

g_{ijk}^L and g_{ijk}^R are the interaction constants of the Higgs boson $H_k = H_4 = H^\pm$ with the chargino - neutralino pair:

$$g_{ijk}^L = \frac{1}{2}(Z_{j2} - \tan\theta_W Z_{j1})(Z_{i3}e_k + Z_{i4}d_k) + i \rightarrow j, \quad (24)$$

$$g_{ijk}^R = \frac{1}{2}(Z_{j2} - \tan\theta_W Z_{j1})(Z_{i3}e_k + Z_{i4}d_k)\varepsilon_k + i \rightarrow j;$$

$Z - 4 \times 4$ matrix diagonalizing the neutralino mass matrix; $\varepsilon_1 = \varepsilon_2 = -\varepsilon_3 = 1$; the coefficients e_k and d_k are given by expressions (9).

In the case of a longitudinally polarized chargino-neutralino pair, the decay width $H^- \Rightarrow \tilde{\chi}_i^- + \tilde{\chi}_j^0$ takes the form:

$$\Gamma(\lambda_1, \lambda_2) = \frac{1}{4}\Gamma_0(H^- \Rightarrow \tilde{\chi}_i^- \tilde{\chi}_j^0)[1 + \lambda_1\lambda_2 + (\lambda_1 + \lambda_2)P], \quad (25)$$

here

$$\Gamma_0(H^- \Rightarrow \tilde{\chi}_i^- \tilde{\chi}_j^0) = \frac{G_F M_W^2}{2\sqrt{2}\pi} M_{H^-} \sqrt{\lambda(r_i, r_j)} \{ [(g_{ijk}^L)^2 + (g_{ijk}^R)^2] (1 - r_i - r_j) - 4g_{ijk}^L g_{ijk}^R \sqrt{r_i r_j} \} \quad (26)$$

is the decay width of the charged Higgs boson into a pair of unpolarized chargino - neutralino, λ_1 and λ_2 are chargino and neutralino helicities, and P is a degree of longitudinal polarization of chargino (neutralino)

$$P = \frac{[(g_{ijk}^L)^2 - (g_{ijk}^R)^2] \sqrt{\lambda(r_i, r_j)}}{[(g_{ijk}^L)^2 + (g_{ijk}^R)^2] (1 - r_i - r_j) - 4g_{ijk}^L g_{ijk}^R \sqrt{r_i r_j}}. \quad (27)$$

In the case when the chargino and neutralino are transversely polarized, for the decay width $H^- \Rightarrow \tilde{\chi}_i^- + \tilde{\chi}_j^0$ we obtain the following expression:

$$\frac{d\Gamma(\eta_1 \eta_2)}{d\varphi} = \frac{1}{4} \frac{d\Gamma_0(H^- \Rightarrow \tilde{\chi}_i^- \tilde{\chi}_j^0)}{d\varphi} [1 + \eta_1 \eta_2 P_\perp]. \quad (28)$$

Here

$$\frac{d\Gamma_0(H^- \Rightarrow \tilde{\chi}_i^- \tilde{\chi}_j^0)}{d\varphi} = \frac{G_F M_W^2}{4\sqrt{2}\pi^2} M_{H^-} \sqrt{\lambda(r_i, r_j)} \{ [(g_{ijk}^L)^2 + (g_{ijk}^R)^2] (1 - r_i - r_j) - 4g_{ijk}^L g_{ijk}^R \sqrt{r_i r_j} \} \quad (29)$$

is a differential decay width and

$$P_\perp = \cos\varphi \frac{2g_{ijk}^L g_{ijk}^R (1 - r_i - r_j) - 2[(g_{ijk}^L)^2 + (g_{ijk}^R)^2] \sqrt{r_i r_j}}{[(g_{ijk}^L)^2 + (g_{ijk}^R)^2] (1 - r_i - r_j) - 4g_{ijk}^L g_{ijk}^R \sqrt{r_i r_j}} \quad (30)$$

is a degree of transverse polarization of chargino - neutralino. It can be seen that the degree of transverse polarization P_\perp is very sensitive to the angle φ between the transverse spin vectors $\vec{\eta}_1$ and $\vec{\eta}_2$. With parallel ($\vec{\eta}_1 \uparrow \vec{\eta}_2$) and antiparallel ($\vec{\eta}_1 \uparrow \vec{\eta}_2$) spin vectors, the degree of transverse polarization modul reaches a maximum value. If the transverse spin vectors $\vec{\eta}_1$ and $\vec{\eta}_2$ are mutually perpendicular ($\vec{\eta}_1 \perp \vec{\eta}_2$), then the degree of transverse polarization P_\perp vanishes.

Note that in the $H^- \Rightarrow \tilde{\chi}_1^- \tilde{\chi}_3^0$ decay the coupling constants g_{ijk}^L and g_{ijk}^R are equal to each other, as a result, the degree of longitudinal polarization of the chargino (neutralino) vanishes, and the degree of transverse polarization of the chargino-neutralino will depend only on the angle φ between the transverse spin vectors $\vec{\eta}_1$ and $\vec{\eta}_2$:

$$P_\perp = \cos\varphi.$$

In the approximation $M_A \gg |\mu| \gg M_2$, the partial decay widths of the charged Higgs boson into a

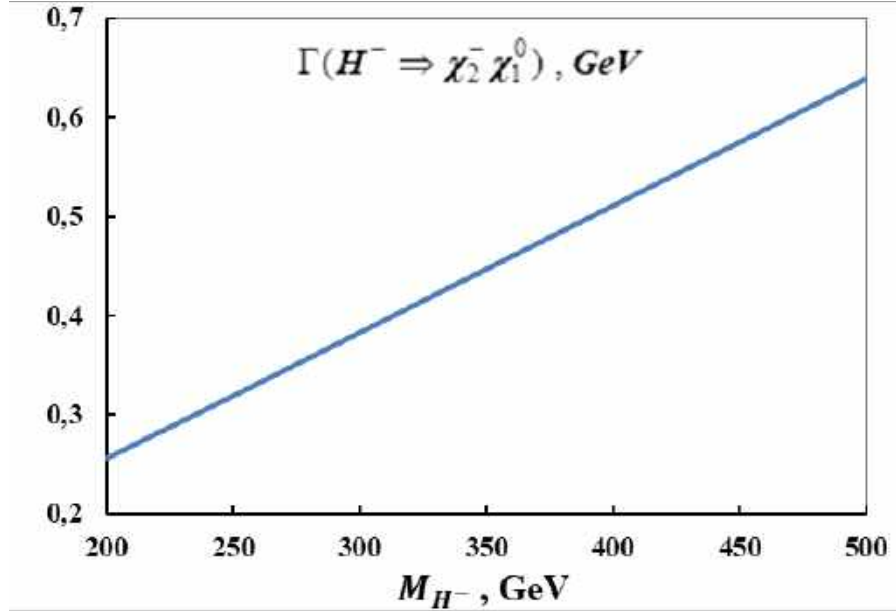
chargino-neutralino pair are given in Table 3 (in $\frac{G_F M_W^2}{4\sqrt{2}\pi} M_{H^\pm}$ units).

Table 3.

 Parsial decay widths $H^\pm \Rightarrow \tilde{\chi}_i^\pm \tilde{\chi}_j^0$

Chargino - neutralino	$\Gamma(H^\pm \Rightarrow \tilde{\chi}_i^\pm \tilde{\chi}_j^0)$
$\tilde{\chi}_1^\pm \tilde{\chi}_3^0$	1
$\tilde{\chi}_1^\pm \tilde{\chi}_4^0$	1
$\tilde{\chi}_2^\pm \tilde{\chi}_1^0$	$\tan^2\theta_W$
$\tilde{\chi}_2^\pm \tilde{\chi}_2^0$	1

In fig.8 shows the dependence of the decay width $H^- \Rightarrow \tilde{\chi}_2^- + \tilde{\chi}_1^0$ on the Higgs mass of the boson M_{H^-} at $\tan\beta = 3$ and $\sin^2\theta_W = 0.2315$. With an increase in the Higgs boson mass M_{H^-} , the decay width increases.


 Fig 8. Dependence of the decay width $H^- \Rightarrow \tilde{\chi}_2^- \tilde{\chi}_1^0$ on the mass M_{H^-}

Note that for large Higgs boson masses, the total decays widths H, A, H^\pm into a pair of chargino and neutralino does not depend on the parameters M_2 , μ , $\tan\beta$ and in the asymptotic limit $M_{H_k} \gg m_{\tilde{\chi}}$ we have

$$\Gamma_0(H_k \Rightarrow \sum_{i,j} \tilde{\chi}_i \tilde{\chi}_j) = \frac{3G_F M_W^2}{4\sqrt{2}\pi} M_{H_k} (1 + \tan^2\theta_W) \quad (31)$$

We also introduce the width of the Higgs boson decay channels $(A) \Rightarrow t + \bar{t}$, $H(A) \Rightarrow b + \bar{b}$, $H^+ \Rightarrow t + \bar{b}$, then we have the expression for branching

$$BR(H_k \Rightarrow \sum_{i,j} \tilde{\chi}_i \tilde{\chi}_j) = \frac{\Gamma(H_k \Rightarrow \sum_{i,j} \tilde{\chi}_i \tilde{\chi}_j)}{\Gamma(H_k \Rightarrow \sum_{i,j} \tilde{\chi}_i \tilde{\chi}_j) + \Gamma(H_k \Rightarrow t\bar{t} + b\bar{b} + t\bar{b})} = \frac{(1 + \frac{1}{3}\tan^2\theta_W)M_W^2}{(1 + \frac{1}{3}\tan^2\theta_W)M_W^2 + m_t^2 \cot^2\beta + m_b^2 \tan^2\beta} \quad (32)$$

In fig.9 illustrates the dependence of branching (32) on the parameter $\tan\beta$ in the asymptotic regime $M_A \sim M_H \sim M_{H^\pm} \approx 1 \text{ TeV} \gg m_\chi$ at $\sin^2\theta_W = 0.2315$.

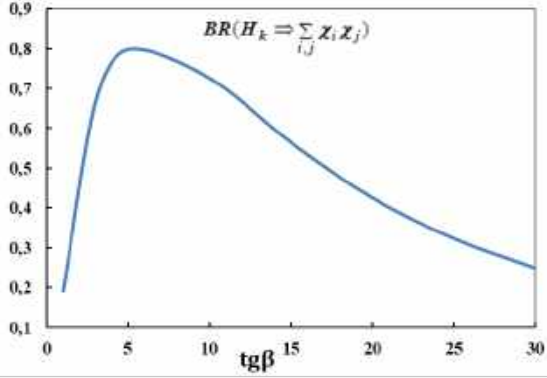


Fig 9. Branching $BR(H_k \Rightarrow \sum_{i,j} \tilde{\chi}_i \tilde{\chi}_j)$ as a function of $\tan\beta$

As can be seen from the figure, with the parameter $\tan\beta$ increasing, the branching also increases and reaches a maximum at $\tan\beta = 5$, and a further increase in the parameter $\tan\beta$ leads to a decrease in branching

5. HIGGS BOSON DECAYS INTO A PAIR OF SFERMIIONS

The scalar partners of fermions (sfermions) form a set of new particles: $\nu_{\tau L}, \tau_L, \tau_R, \tilde{t}_L, \tilde{t}_R, \tilde{b}_L, \tilde{b}_R$ are in the third family. All of them are complex scalar fields and the indices L, R are used to denote the SM fermions with which these fields partner. The sfermions \tilde{f}_L and \tilde{f}_R mix with each other and new states \tilde{f}_1 и \tilde{f}_2 with masses arise

$$m_{\tilde{f}_1, \tilde{f}_2}^2 = m_f^2 + \frac{1}{2} \left[m_{\tilde{f}_L}^2 + m_{\tilde{f}_R}^2 \mp \sqrt{(m_{\tilde{f}_L}^2 - m_{\tilde{f}_R}^2)^2 + 4m_f^2(A_f - \mu r_f)^2} \right], \quad (33)$$

where A_f and r_f is some parameters.

The interaction constants of neutral Higgs bosons with sfermions are determined by the expressions

$$\begin{aligned} g_{H_k \tilde{f}_L \tilde{f}_L} &= m_f^2 + M_Z^2 (I_3(f) - Q_f \sin^2 \theta_W) g_2, \\ g_{H_k \tilde{f}_R \tilde{f}_R} &= m_f^2 g_1 + M_Z^2 Q_f \sin^2 \theta_W g_2, \\ g_{H_k \tilde{f}_L \tilde{f}_R} &= -\frac{1}{2} m_f (\mu g_3 - A_f g_4), \end{aligned} \quad (34)$$

where the coefficients $g_i (i = 1, 2, 3, 4)$ are given in Table 4.

Table 4.

Coefficients $g_i (i = 1, 2, 3, 4)$

\tilde{f}	H_k	g_1	g_2	g_3	g_4
\tilde{t}	H	$\sin\alpha/\sin\beta$	$\cos(\alpha + \beta)$	$\cos\alpha/\sin\beta$	$\sin\alpha/\sin\beta$
	h	$\cos\alpha/\sin\beta$	$-\sin(\alpha + \beta)$	$-\sin\alpha/\sin\beta$	$\cos\alpha/\sin\beta$
	A	0	0	1	$-\tan\beta$
\tilde{b}	H	$\cos\alpha/\cos\beta$	$\cos(\alpha + \beta)$	$\sin\alpha/\cos\beta$	$\cos\alpha/\cos\beta$
	h	$-\sin\alpha/\cos\beta$	$-\sin(\alpha + \beta)$	$\cos\alpha/\cos\beta$	$-\sin\alpha/\cos\beta$
	A	0	0	1	$-\tan\beta$

The interaction constants of the charged Higgs boson H^\pm with a sfermion pair $\tilde{t}_\alpha \tilde{b}_\beta$ ($\alpha, \beta = L, R$) can be expressed as:

$$g_{H^\pm \tilde{t}_\alpha \tilde{b}_\beta} = \frac{1}{\sqrt{2}} (g_1^{\alpha\beta} + M_W^2 g_2^{\alpha\beta}), \quad (35)$$

The coefficients $g_1^{\alpha\beta}$ and $g_2^{\alpha\beta}$ are shown in Table 5.

Table 5.

Coefficients $g_i^{\alpha\beta} (i = 1, 2; \alpha, \beta = L, R)$

i	g_i^{LL}	g_i^{RR}	g_i^{LR}	g_i^{RL}
1	$m_t^2 \cot\alpha + m_b^2 \tan\beta$	$m_t m_b (\cot\alpha + \tan\beta)$	$m_b (\mu + A_b \tan\beta)$	$m_t (\mu + A_t \cot\alpha)$
2	$-\sin 2\beta$	0	0	0

The partial Higgs boson decay widths H_k ($k = 1, 2, 3$ and 4 correspond to the bosons, H, h, A and H^\pm) in the sfermion pair $\tilde{f}_i \tilde{f}_j$ ($i, j = 1, 2$) can be written as follows:

$$\Gamma(H_k \Rightarrow \tilde{f}_i \tilde{f}_j) = \frac{N_c G_F}{2\sqrt{2}\pi M_{H_k}} \sqrt{\lambda(r_i, r_j)} (g_{H_k \tilde{f}_i \tilde{f}_j})^2, \quad (36)$$

where N_c is the color factor ($N_c = 3(1)$) at the birth of a squark (slepton) pair $r_i = \left(\frac{m_{\tilde{f}_i}}{M_{H_k}}\right)^2$, $r_j = \left(\frac{m_{\tilde{f}_j}}{M_{H_k}}\right)^2$; interaction constants $g_{H_k \tilde{f}_i \tilde{f}_j}$ can be obtained from the interaction constants (34) and (35) using the mixing relations of sfermions. These constants are given in [8, 11].

To estimate the decay width (36), we consider H^\pm boson decay into a pair of $\tilde{u}_L \tilde{d}_L$ -squarks. In this decay, the interaction constant $g_{H^\pm \tilde{u}_L \tilde{d}_L}$ is equal to:

$$g_{H^\pm \tilde{u}_L \tilde{d}_L} = -\frac{1}{\sqrt{2}} [m_u^2 \cot \beta + m_d^2 \tan \beta - M_W^2 \sin 2\beta]. \quad (37)$$

Since the masses of u - and d -quarks are much smaller than the mass of the gauge W -boson ($M_W \gg m_u, m_d$), for the interaction constant $g_{H^\pm \tilde{u}_L \tilde{d}_L}$ we have:

$$g_{H^\pm \tilde{u}_L \tilde{d}_L} = -\frac{1}{\sqrt{2}} M_W^2 \sin 2\beta. \quad (38)$$

Thus, in the first and second families with massless fermions, the pseudoscalar A -boson does not decay into a pair of sfermions, and the decay widths of the heavier H^\pm and H -bosons into a sfermion pair are proportional to the expression

$$\Gamma(H^\pm(H) \Rightarrow \tilde{f} \tilde{f}) \sim \frac{G_F M_W^4}{2\sqrt{2}\pi M_{H^\pm(H)}} \sin^2 2\beta. \quad (39)$$

These decay widths are maximum for small values of the parameter $\tan \beta \approx 1$.

Figure 10 shows the dependence of the decay width $H^\pm \Rightarrow \tilde{t}_R + \tilde{b}_L$ on the Higgs boson mass M_{H^\pm} for $m_{\tilde{t}} = 160 \text{ GeV}$, $m_{\tilde{b}} = 140 \text{ GeV}$, $\tan \beta = 10$, $\mu = 160 \text{ GeV}$ and $A_t = 320 \text{ GeV}$. It can be seen from the figure that with an increase in the Higgs boson mass M_{H^\pm} the decay width increases and reaches a maximum at $M_{H^\pm} = 425 \text{ GeV}$, and then the decay width decreases and near $M_{H^\pm} = 650 \text{ GeV}$ secondary maximum and with a further increase in the Higgs boson mass, its decay width decreases again.

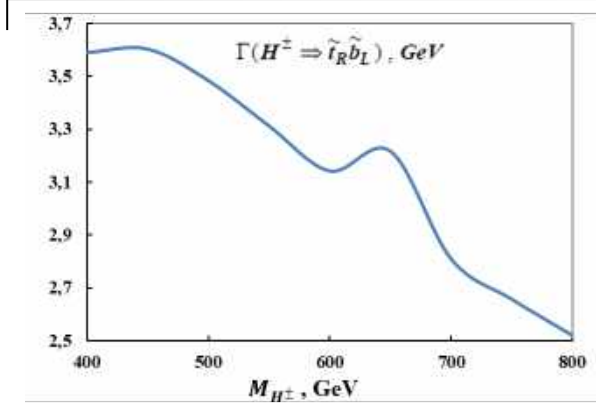


Fig 10. Dependence of the decay width $\Gamma(H^\pm \Rightarrow \tilde{t}_R \tilde{b}_L)$ on the mass M_{H^\pm}

CONCLUSION

We discussed the decay widths of the Higgs bosons H, h, A and H^\pm into supersymmetric particles, precisely decays into a pair of chargino $H_k \Rightarrow \tilde{\chi}_i^\pm + \tilde{\chi}_j^\pm$, decays into a pair of neutralino $H_k \Rightarrow \tilde{\chi}_i^0 + \tilde{\chi}_j^0$, decays into a pair of chargino-neutralino $H_k^\pm \Rightarrow \tilde{\chi}_i^\pm + \tilde{\chi}_j^0$, decays into a pair of sfermions $H_k \Rightarrow \tilde{f}_i + \tilde{f}_j$. In the framework of the $MSSM$, analytical expressions are obtained for the decay width of the Higgs boson mass. The research results are illustrated by graphs.

- [1] ATLAS Collaboration. Observation of a new particle in the search for the Standard Model Higgs boson at the ATLAS detector at the LHC. Phys. Letters, 2012. B716,] p.1-29.
- [2] CMS Collaboration. Observation of a new boson at mass of 125 GeV with the CMS experiment at the LHC. Phys. Letters, 2012, B716, p.30-61.
- [3] V.A. Rubakov. On Large Hadron Colliders discovery of a new particle with Higgs boson properties. UFN, 2012, v.182, №10, p.1017-1025 (in Russian).
- [4] A.V. Lanev. CMS Collaboration results: Higgs boson and search for new physics. UFN, 2014, v.184, №9, p.996-1004 (in Russian).
- [5] D.I. Kazakov. The Higgs boson is found: what is next?. UFN, 2014, v.184, №9, p.1004-1016 (in Russian).
- [6] F. Englert, R. Brout. Broken Symmetry and the mass of gauge vector bosons. Phys. Rev. Letters, 1964, v.13, №9, p.321.
- [7] P.W. Higgs. Broken symmetries and the masses of gauge bosons. // Phys. Rev. Letters, 1964, v.13, №16, p.508.
- [8] A. Djouadi. The Anatomy of Electro-Weak Symmetry Breaking. Tome II. The Higgs Boson in the MSSM. archive: hep-ph 0503173 v.2, 2003.
- [9] J.F. Gunion, H. E. Haber. Higgs bosons in supersymmetric models (I) Nucl. Phys., 1986, v. B 272, p.1-76.

- [10] J.F. Gunion, H. E. Haber. Higgs bosons in supersymmetric models (II) Nucl. Phys., 1986, v. B 278, p.449-492.
- [11] *M. Spira*. QCD effects in Higgs Physics. archive: hep – ph . 9705337 v.2, 1997.
- [12] *A. Djouadi, J. Kalinowski, P. M. Zerwas*. Two – and Three- Body Decay Modes of SUSY Higgs Particles. archive: hep – ph 9511342 v.1, 1995.
- [13] *S.K. Abdullayev, E.Sh. Omarova*. Decays of supersymmetric Higgs bosons into fermions. AJP Fizika, 2018, V. XXIV, №4, p.22-34.
- [14] *S. K. Abdullayev, E. Sh. Omarova*. Decays of Higgs Bosons into a fermion-antifermion pair. Russian Physics Journal, 2019, v.61. №9, p.1603-1612.
- [15] *S.K. Abdullayev, E.Sh. Omarova*. Decay channels of Higgs Bosons $H(h; A) \Rightarrow \gamma\gamma, H(h; A) \Rightarrow \gamma Z$, $H^\pm \Rightarrow \gamma W^\pm$. Journal of Baku Engineering University – Physics, 2019, v.3, №1, p.39-57.
- [16] *S. K. Abdullayev, E.Sh. Omarova*. Decays of Higgs Bosons into a gauge boson and a fermion-antifermion pair. Russian Physics Journal, 2019, v.62. №1, p.30-39.
- [17] *S.K. Abdullayev, E.Sh. Omarova*. Three-particle decays of the Higgs Bosons in the Minimal Supersymmetric Standard Model. Russian Physics Journal, 2019, v.62. №3, p.425-435.
- [18] *S.K. Abdullayev, E.Sh. Omarova*. Decays of $H(h; A)$ bosons into two photons (gluons). Russian Physics Journal, 2020, v.62. №9, p.1623-1634.

Received: 29.09.2020

THE PHOTOELECTRIC PECULIARITIES OF ELECTROGRAPHIC LAYERS OF TRIGONAL SELENIUM, CHEMICALLY PURIFIED AND DOPED BY SODIUM

V.G. AGAYEV

Institute of Physics of ANAS,

AZ 1143, H.Javid ave., 131

The electrographic layers on the base of trigonal selenium, chemically purified and doped by sodium, in binding material are prepared. The main parameters and characteristics of the layers with sodium impurity and without it are investigated. It is shown that sodium impurity especially improves the layer properties.

Keywords: photographic materials, electrophotographic layer.

PACS: 68.20; 72.20

INTRODUCTION

The electrography, the principles of which are connected with achievements of semiconductor physics, is the one of the most distributed and intensively developed reproduction methods. The wide application of electrography causes the necessity in improvement of present photoreceptors and formation of new ones. The photosensitivity in visual and especially red regions of spectrum is the important criterion. Nowadays, the schemes of xerographic image reproduction based on the use of amorphous selenium, A^2B^6 type compounds, organic semiconductors and etc, are realized. The investigations on formation of photoreceptors on the base of amorphous silicon enriched by oxygen are carried out.

The elementary semiconductor Se notices attention of investigators by its unique properties. It has the high photosensitivity, it can be obtained in amorphous, (glassy), and crystal (trigonal and monoclinic) states. All these properties make it irreplaceable one at formation of different transformers (first power rectifiers, photoreceptors, vidicons, photoisolators and etc). The high technological effectiveness of selenium (low melting point, possibility of marking on the surface of any form and etc) is the important. The wide use of Se in different technique fields constantly stimulates the investigations of its properties in whole world. The wide-ranging investigations of selenium and transformers on its base have begun in early 50th in Institute of Physics of ANAS. The dependence of physical properties of selenium on external action conditions and impurities has the complex character. The many experimental data of different authors essentially differ that makes difficult their interpretation with unique positions. The ambiguity is caused by specificity and complexity of selenium structure, structure diversity of its molecules. This peculiarity gives to Se and its transformers on its base such property gamma which makes this semiconductor irreplaceable one in some cases. The same peculiarity transforms Se in difficult investigation object [1-4 and etc].

Se belongs to the number of more sensitive photosemiconductors in visible region of spectrum and that's why both amorphous and trigonal Se are widely

used at formation of photoreceptors of different functional destinations.

EXPERIMENT AND RESULT DISCUSSION

The chemical methods of material obtaining and treatment have the big possibilities for directed change of photo-semiconductor properties. The fact that the final product is obtained more fine-dispersed one that at mechanical chopping and no necessity in separation by sizes is the one of important advantages of chemical method use. As only near-surface regions of photo-semiconductor particles take place in electrographic process (light quanta penetrate in intrinsic absorption region in depth 1μm), then the photo-semiconductor is used more effectively and the layers are more homogeneous ones at chemical method.

The photoreceptors on the base of amorphous selenium have the high electrographic parameters (good charging and sensitivity), but they have the essential disadvantages. They are weakly sensitive to red light, as a result of exploitation and even the storage the layers of amorphous Se crystallize under the influence of many factors and break down. Also, their production includes many steps, requires the difficult vacuum equipment, big power inputs and etc. Trigonal Se is known as photosemiconductor with spectral sensitivity covered whole visible region. Usually, layers of trigonal Se are prepared by dispersing of its particles in polymer binding material and deposition of suspension on conducting substrate. They have well photosensitivity, but they have the low initial charging potential and dark semi-decay that is the sequence of Se high conduction.

Firstly, the aim of the given work is the defect elimination belonging to layers from trigonal Se obtained by usual dispersing technology in binding material, and secondly, the search of improvement ways of their parameters and characteristics. With this purpose the search of appropriate chemical methods has been carried out.

The trigonal Se crystals are obtained from initial Se powder of high pureness 99,999%, by previous thermo-treatment in evaporated quartz ampoules at 700°C during 3 hours by rapid cooling of melt up to 250°C, quenching in running water and crystallization at 210°C during 40 hours (4). The specific resistance is

$5 \cdot 10^6$ Ohm-cm with forbidden band thickness 1,8 eV. The melting point is 200°C . The freshly prepared layers in binding material charge positively and have low charging potential. The monotonous annealing of layer main parameters is observed when the layers are treated to continuous annealing at 100°C - 180°C with further slow cooling. The general photosensitivity increases up to $0,5 (\text{lux} \cdot \text{C})^{-1}$ at annealing 160°C .

The chosen method of purification and doping of Se is caused by the following circumstances. It is known that impurities of alkali metals (for example, sodium) decreases Se conduction on several orders and that's why this should led to increase of layer charging potential on its base and decrease of its dark relaxation velocity. The advantage is in the fact that the photo-semiconductor material is obtained in the form of low-dispersed powder particles with the surface enriched by sodium in comparison with traditional high-temperature doping. The method is described in detail in work [5]: Se is endured during 5-16 hours in solution of caustic sodium with following neutralization by hydrochloric acid. The precipitated material is obtained in the form of low-dispersed powder particles of Se enriched by sodium. X-ray diffraction investigations show that Se obtained by the given method presents itself the low-dispersed powder of trigonal Se with average particle size $\leq 0,7 \mu\text{m}$. The electrographic layers of them are prepared by dispersing in binding material from butyral resin solution in ethyl alcohol and deposition of suspension on electroconducting substrates. The layers with thickness $20 \pm 2 \mu\text{m}$ further are treated at 160°C during 0,5 hours.

The main parameters and characteristics are investigated by noncontact method on electrometric installation with vibrating gauge under layer surface (in static regime). The electrization is carried out in corona charge by high voltage block $\pm 7\text{kV}$ and exposure is carried out by white or monochromatic light. The irradiance is forecasted by radiation thermo-element. The decay of charging potential is registered by pointer instrument or storage unit C8-13 switched on to output of electrometric amplifier.

The general photosensitivity of electrographic layer is defined by decay velocity of charging potential at illumination. The photo-sensitivity criterion can be value of surface potential change at definite exposure conditions or exposition value necessary for providing of definite potential drop can serve the photo-sensitivity criterion. The layer photo-sensitivity can be characterized by time of exposure t (in seconds) duration which the surface potential decreases in two times in the case of L (in lux) constant illumination. At definition of spectral sensitivity, the illumination is measured in energy units by number of incident quanta on unit of area of layer surface per time unit. In case of L constant illumination the layer photosensitivity S_λ can be characterized by the time of exposure t (in seconds) duration which surface potential V decreases in two times:

$$S_\lambda = \left(\frac{1}{L \lambda \cdot t} \right) \frac{\Delta N}{v} = \frac{1}{2}, \quad \text{SM}^2 \cdot \text{J}^{-1} \quad (1)$$

The quantum efficiency of charge carrier photogeneration η is defined as ratio of generated charge number in the layer Δn to number of absorbed light quanta ΔN . At illumination by monochromatic light potential decay ΔV is expressed by formula:

$$\Delta V = \frac{\Delta n \cdot l}{C}$$

From here it is followed:

$$\eta = \frac{\Delta n}{\Delta N} = \frac{\Delta V \cdot C}{L \cdot \Delta N} \quad (2)$$

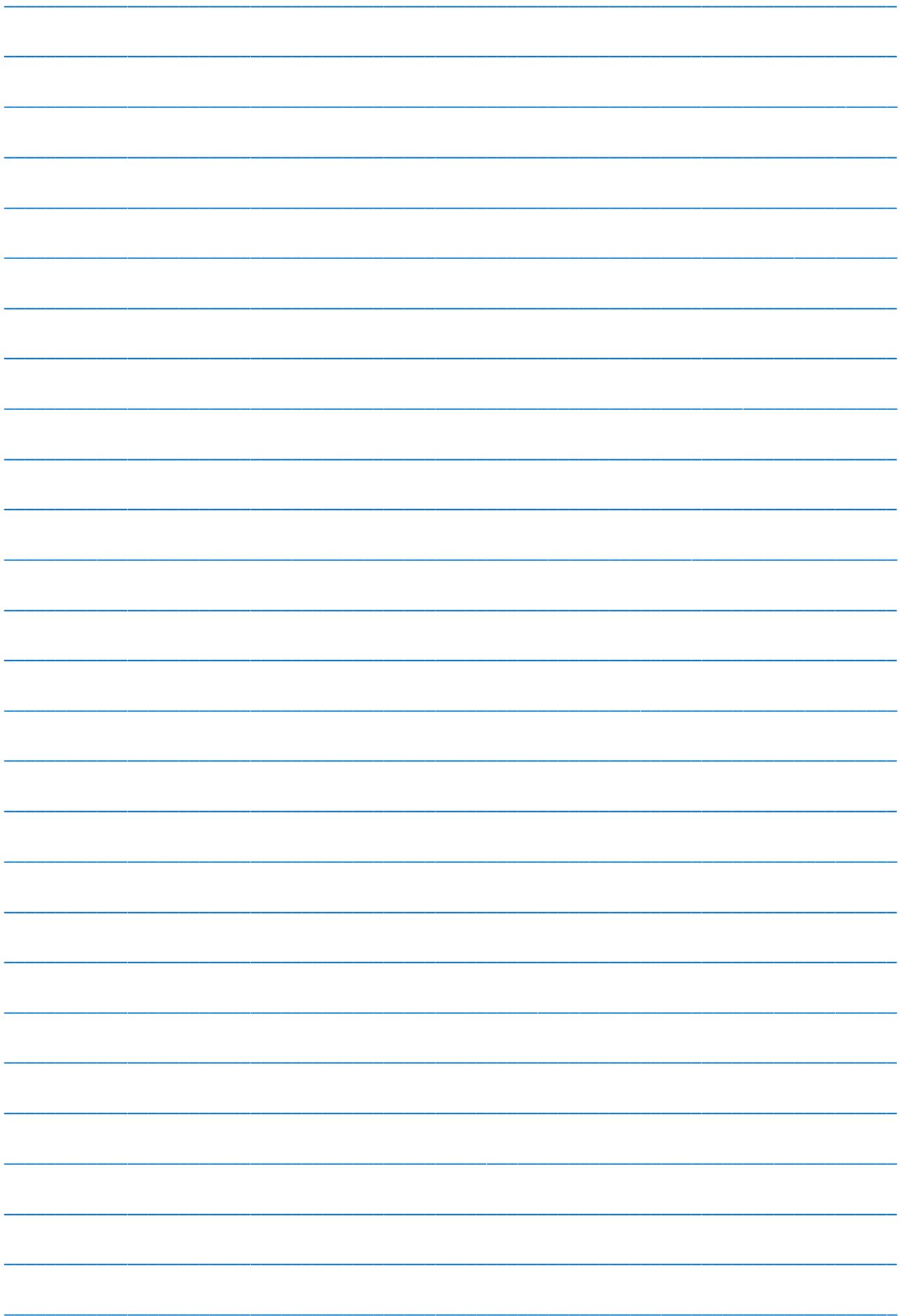
where C is layer electrocapacity, e is elementary charge. Using V , C , e and Δn we can calculate the spectral distribution of quantum output of internal photoelectric effect. After optimization of technological process of electrographic layer preparation the comparison of layer parameters of trigonal Se doped by sodium and initial one (without sodium) shows that the layers doped by sodium are the best on all parameters. This fact proves that chemical purification and doping by sodium essentially improves the layer properties on the base of trigonal Se in binding material. The method is in the fact that sodium impurities penetrate in near-surface region of trigonal Se micro-particles as a result of diffusion at annealing, i.e. especially in that region where light quanta penetrate at illumination of electrographic layer. Indeed, this is proved by the fact that general photosensitivity is bigger ($\geq 0,8 \text{ lux}^{-1} \cdot \text{C}^{-1}$ at charging potential $\geq 300\text{V}$) in layers of Se doped by sodium than in layers of initial Se. The essential outgrowing both photosensitivity and quantum output and also their expansion into long-wavelength spectrum region takes place in spectral distribution of photosensitivity and quantum output of the layers with doping. As quantum energy becomes enough for formation of electron-hole couples, then quantum output rapidly grows up to 0,7 and further the photo-sensitivity increasing up to 700 nm appears in absorption band. The illumination of intrinsic light (case of strong absorption) leads to photogeneration of charge carriers in thin near-surface region of electrographic layer whereas at impurity photo electric effect the carriers generate in whole volume. The photoreceptor has maximum photosensitivity in intrinsic absorption band. The general sensitivity decreases in the result of increase of forbidden band and intrinsic absorption edge shifts to the short-wave spectrum region. That's why for supply of its growth one should prepare the layer from photo-semiconductor with narrow band. So, the formation of electrographic layers on the base of trigonal Se is actual.

[1] G.B. Abdullayev, D.Sh. Abidinov. Se physics, Elm, Baku, 1975.

[2] G.B. Abdullayev, N.I. Ibragomov, V.G. Agayev. Author's certificate. USSR: 467315 (1974),

- 560200(1977), 627707(1978), 704395(1979), 1170413(1985), 1176299(1985), 1301169(1986), 0281072(1987), 1403010(1988), 1466504(1988), 1568016(1990), 1603335(1990), 1675837(1991), 1730608(1992), 1807442(1992).
- [3] *N.İ. İbragimov, V.G. Agaev, Z.M. Abutalibova.* Thin solid films, 2000, V. 359, P 125.
- [4] *N.İ. İbragimov.* Doctor Thesis, Baky, 1980.
- [5] *N.İ. İbragimov, V.G. Agaev, Z.M. Abutalibova.* Author's certificate, USSR. №1675833, 1991.

Received: 17.09.2020



CONTENTS

1.	Rashba spin-orbit interaction in semiconductor nanostructures B.G. Ibragimov	3
2.	Dielectric, conductivity, and electro-optic properties of liquid crystal 5cb doped by single-walled carbon nanotubes T.D. Ibragimov, A.R. Imamaliyev, G.F. Ganizade	10
3.	The investigation of equilibrium and dynamic characteristics of dielectric polarization of chlorobenzene – <i>n</i> – butyl alcohol solution S.T. Azizov, G.M. Askerov	15
4.	Dielectric relaxations of chlorobenzene-benzene and chlorobenzene- <i>n</i> -hexane solutions S.T. Azizov	18
5.	Characterization of optical parameters and evaluation of the quantum yield of the led phosphor layer T.Y. Orujov	21
6.	Refinement of the crystal structure of MnBi_2Te_4 I.R. Amiraslanov, P.A. Askerova, Z.S. Aliyev, Y.R. Aliyeva, A.B. Rahimli	25
7.	Influence of surface disturbances of $\text{Bi}_{0.5}\text{Sb}_{1.5}\text{Te}_3$ crystal on the transport of electrons in its volume, surface and in the interface with Bi-Sn alloy N.M. Akhundova, T.D. Aliyeva, G.J. Abdinova	30
8.	Magnetic interaction of "excess" cations Cu^{+2} and Fe^{+2} in the 2D-plane in a single crystal $\text{Cu}_{1.04}\text{Fe}_{1.12}\text{Te}_{1.84}$ A.I. Jabbarov	33
9.	Higgs boson decays into a pair of supersymmetric particles S.K. Abdullaev, E.SH. Omarova	38
10.	The photoelectric peculiarities of electrographic layers of trigonal selenium, chemically pured and doped by sodium V.G. Agayev	51



www.physics.gov.az